Preparation of Calcium Atoms at High Phase Space Density in a Continuously Loaded Dipole Trap

Dissertation

zur Erlangung des Doktorgrades
des Department Physik
der Universität Hamburg

vorgelegt von
Chih-Yun Yang
aus Luodong (Taiwan)

Hamburg
2011

Gutachter der Dissertation:	Prof. Dr. Andreas Hemmerich
	Prof. Dr. Henning Moritz
Gutachter der Disputation:	Prof. Dr. Andreas Hemmerich
	Prof. Dr. Klaus Sengstock
Datum der Disputation:	03.05.2011
Vorsitzender des Prüfungsausschusses:	Prof. Dr. Peter Schmelcher
Vorsitzender des Promotionsausschusses:	Prof. Dr. Günter Huber
Dekan der Fakultät für Mathematik, Informatik und Naturwissenschaften:	Prof. Dr. Heinrich Graener

Abstract

In this thesis, a novel approach for the production of ^{40}Ca ensembles at high phase space density (PSD) in the $^1S_0$ state is investigated. Firstly, a continuous loading scheme is studied to efficiently transfer $^3P_2$ atoms from a density limited $^3P_2$ triplet magneto-optical trap (MOT) into an optical dipole trap (ODT) in the $^1S_0$ ground state. As a consequence, the density of the atoms in the ODT is one order of magnitude larger and the PSD of the atoms in the ODT is three orders of magnitude larger compared to the parameters of the $^3P_2$ triplet-MOT. The results indicate that the loading process is neither limited by the volume difference between the MOT and the ODT nor by the density limited atomic reservoir. Numerical models are presented which identify the relevant physical mechanisms of the loading and decay dynamics. Moreover, they reveal that the novel loading scheme is based upon a spatial energy selective optical pumping transfer. Secondly, a crossed optical dipole trap (CODT) setup is applied to further increase the PSD of the ensemble. Utilizing the developed loading scheme, the peak density of the atoms in the dimple formed by the $^1S_0$ CODT reaches the order of $10^{14}\,\mathrm{cm}^{-3}$. Finally, in order to realize a ^{40}Ca Bose-Einstein Condensate (BEC), forced evaporative cooling is applied. Two evaporation schemes previously applied for ^{174}Yb and ^{40}Ca are studied which are successfully applied to atomic samples with densities and temperatures comparable to our initial sample. The experimental observations are used to optimize the evaporation strategy for our specific case. Utilizing the newly designed strategy, the highest obtained PSD of the atom ensemble is 0.146, limited by a fast loss of particles arising at the end of the evaporation process - independent of the specific protocol used. Numerical calculations suggest that residual stray light heating might be the underlying mechanism.

Kurzfassung

Diese Arbeit beschäftigt sich mit einem neuartigen Verfahren, um ^{40}Ca-Atomensembles mit hoher Phasenraumdichte (PSD) im Grundzustand $^1S_0$ zu erzeugen. Dazu wurde ein Verfahren entwickelt, mit dem die ^{40}Ca-Atome kontinuierlich und effizient von einer magneto-optischen Falle (MOT) für den $^3P_2$-Triplett-Zustand mit begrenzter Dichte in eine optische Dipolfalle (ODT) transferiert werden. Nach der Übertragung ist die Atomdichte der ODT eine Größenordnung und die PSD der ODT drei Größenordnungen höher. Die Ergebnisse deuten darauf hin, dass der Transferprozess durch optisches Pumpen nicht durch den Volumenunterschied zwischen MOT und ODT begrenzt und dass er räumlich und energetisch hochgradig selektiv ist. Mittels numerischer Simulationsrechnungen wurden die relevanten physikalischen Mechanismen identifiziert, welche für den Einfangprozess und den Verlusten in der Falle eine Rolle spielen. Als nächstes wurde eine gekreuzte Dipolfalle (CODT) verwendet, um die PSD des Ensembles weiter zu erhöhen. Unter Verwendung eines selbstentwickelten Befüllungsschemas konnte die Atomdichte in der $^1S_0$ CODT den Bereich von $10^{14}\,\mathrm{cm}^{-3}$ erreichen. Rechnungen ergaben, dass die Atome noch mehrere hundert Millisekunden nach Beenden des Ladevorgangs im Überlappungsbereich eingefangen werden. Als letztes wurde mit einem optimierten Evaporationskühlungsprozess versucht, den Zustand eines Bose-Einstein-Kondensats (BEC) zu erreichen. Anhand zweier erfolgreich erprobter Evaporationskühlungsverfahren für ^{174}Yb- und ^{40}Ca-Atomensembles mit vergleichbaren Teilchendichten und Temperaturen konnte die Evaporationsstrategie für den verwendeten experimentellen Aufbau optimiert werden. Die dadurch erzielte PSD von 0,146 stellt die bis dato höchste erreichte PSD für diesen Aufbau dar. Während der Evaporation wurde ein kontinuierlicher, schneller Teilchenverlust beobachtet, der unabhängig von der angewandten Evaporationsstrategie auftritt und vermutlich auf Erwärmung durch Streulicht zurückzuführen ist.

Contents

Chapter 1

Introduction

Recent developments of laser cooling and trapping techniques have opened new possibilities for studies in the ultracold temperature regime. One of the major breakthroughs in this field is the realization of an atomic Bose-Einstein Condensate (BEC) which provides the chance to study fundamental quantum mechanics experimentally in a macroscopic system. Before 2003, all observed BECs were achieved in atoms with one valence electron, especially alkaline-metal atoms (AMAs), which are the most extensively studied elements. There are many reasons for the popularity of AMAs in laser cooling experiments. One of the reasons is that the lasers required for AMA experiments are easy to build and low cost. The other reason is that alkaline-metal atomic beams are relatively simple to generate because of their low vapour pressure.

Despite AMAs being good candidates for ultracold atom experiments, extending fundamental research beyond AMAs is important. Many groups are involved in the search for BECs of atoms in quantum states with zero total angular momentum, for example those realized by the ground states of effective two-electron systems such as alkaline-earth atoms (AEAs). Different from AMAs, the major isotopes of AEAs have no hyperfine structure, except for Be. Detailed atomic properties of the major isotopes of group-II elements can found in [Mac01]. Therefore two-electron atoms allow good comparisons between experiments and theoretical work because they greatly simplify theoretical calculations. However, experiments for AEAs studies are much more complicated. Firstly, the lasers required for AEA experiments are more technical to construct as the principal fluorescence lines are located in the blue and UV parts of the spectrum. Secondly, an exceedingly stable laser system is required for the application of the intercombination transition. The spin zero ground state excludes the application of the polarization gradient cooling technique. Instead, the narrow intercombination transition $^1S_0$ to $^3P_1$ of

AEAs is used to reduce the temperature of the atomic ensemble. The two valence electrons of the atoms result in singlet and triplet states which are connected by extremely narrow intercombination transitions for example the transition from the $^1S_0$ state to the $^3P_1$ state. Theoretically a dipole transition between the singlet and triplet states is forbidden. But, the $^3P_1$ state is not a pure triplet state and has small singlet component. Therefore, due to mixing with a nearby $^1P_1$ state, a weak dipole transition arises between the $^1S_0$ and $^3P_1$ states of AEAs. For such a narrow transition, the resulting Doppler temperature limit calculated is approximately the same order as the recoil temperature.

In 2003, a ^{174}Yb BEC in the $^1S_0$ singlet state was successfully achieved by the research group in Kyoto University [Tak03]. This achievement is encouraging for all physicists pursuing AEA BECs. Rare earth Yb atoms have distinct features related to the two valence electrons and its ground state electronic structure is similar to AEAs. The ^{174}Yb BEC system combines the magneto-optical trap (MOT) with the intercombination transition $^1S_0$ to $^3P_1$ and the newly designed crossed optical dipole trap (CODT). The temperature of the atoms in the MOT is reduced to the microkelvin range before atoms are loaded into the CODT. To realize the CODT, two optical dipole traps (ODTs) are crossed in the horizontal and vertical planes. The crossed region acts as a dimple in the reservoir formed by the non-crossed region. The ODT in the horizontal plane (HODT) provides a large trap volume to capture large amounts of cold atoms. The ODT in the vertical plane (VODT), with a shallow trap depth, offers ideal conditions for evaporative cooling, such as providing an additional confining force during the evaporative cooling process, offering a path for hot atoms to escape from the trap and eliminating undesired collisions with cold atoms in the dimple [Tak09]. Additionally, ^{174}Yb atoms have a small positive scattering length in the $^1S_0$ ground state ($\approx 104\,a_0$, $a_0 = 0.0529\,\text{nm}$ is the Bohr radius), providing good conditions for evaporation. Once forced evaporative cooling is performed by ramping down the HODT trap depth, the BEC is realized.

In 2009 the first AEA BEC, a ^{40}Ca BEC in the $^1S_0$ ground state, was successfully obtained by the ^{40}Ca research group at the Physikalisch-Technische Bundesanstalt (PTB), Braunschweig [Kra09]. Difficulties in reaching BEC in ^{40}Ca arise due to ^{40}Ca atoms possessing a particularly large ground state scattering length ($\approx 440\,a_0$) which results in losses and heating of the atoms due to three-body collisions. The ^{40}Ca research group at the PTB has developed the evaporative cooling strategy to remove this drawback, making a ^{40}Ca BEC possible. The system uses two-MOTs and a CODT system. The atomic reservoir of the CODT is sourced from a two-MOTs system with application of the intercombination transition $^1S_0$ to $^3P_1$. The intercombination

transition of ^{40}Ca atoms (of linewidth $\Gamma \approx 2\pi \times 400\,\mathrm{Hz}$) is much narrower than that of ^{174}Yb atoms ($\Gamma \approx 2\pi \times 182\,\mathrm{kHz}$). Narrow transition linewidths result in a weak scattering force, hampering the cooling process. For effective cooling, the upper state of the intercombination transition, the $^3P_1$ state, is coupled to the higher lying $^1D_2$ [4s4d] state with an additional laser such that the atoms can decay to the $^1S_0$ ground state via the $^1D_2$ [4s4d] state. This increases the scattering rate and thus the maximum radiation pressure force. The CODT is configured in largely the same way as for the ^{174}Yb experiment [Tak09]. To eliminate large three-body losses, the individual CODT beam waists are comparatively broad. The evaporative cooling process is obtained by generally ramping down the depths of the two ODTs.

BECs with two-electron atoms provide many interesting research topics. So far, ^{40}Ca and ^{84}Sr BECs in the $^1S_0$ ground state have been obtained [Kra09, Ste09, Eco09]. The intercombination transitions of AEAs, especially for ^{40}Ca atoms, have been considered for frequency and time standards [Hal89, Ste04] and a spinless BEC allows the use of novel interferometry which is not affected by any external magnetic field. Various interesting applications of ^{40}Ca BECs are described below.

Optical Feshbach Resonance

One exciting application of ^{40}Ca BECs is optical tuning of the ground state scattering length of ^{40}Ca atoms, the so-called optical Feshbach resonance. The ability to modify interactions between colliding ultracold atoms opens possibilities for exciting experiments with ultracold atomic gases. In recent years, the magnetic Feshbach resonance has been a key technique. For instance, the first BEC of ^{133}Cs atoms [Web03b] to be observed would have been impossible without magnetically tuning interactions from being attractive to being repulsive. However, the magnetic Feshbach resonance is not applicable for atoms in quantum states with zero total angular momentum. Recently, the theoretical optical Feshbach resonance was analyzed by Bohn and Julienne [Boh97, Boh99] and has been experimentally presented, initially in ^{87}Rb atoms. A significant tuning of scattering length was observed, but it was accompanied with a substantial loss of atoms. Afterward, the theoretical work of Ciurylo et al. in 2005 [Ciu05] discovered that it is possible to tune the scattering length for collisions of the ultracold $^1S_0$ ground state AEAs by using an optical Feshbach resonance and without serious decrease in atom number. This can be achieved using a laser which is far detuned from an excited molecular level near the frequency of the atomic intercombination transition from the $^1S_0$ state to the $^3P_1$ state. The narrow linewidth of the intercombination transition allows the use of an excited molecular level close

to the dissociation limit that provides a strong optical coupling because of a large Frank-Condon overlap for the photoassociation (PA) transition, while atom losses due to photon scattering are kept small.

A Feshbach resonance occurs when the energy of a colliding pair of atoms in an open channel is close to the energy of a molecular bound state in the closed channel. The energy of the internal atomic states depends on the external parameters, thus the magnitude and the sign of the scattering length can be tuned by varying the external parameters such as the strength of a magnetic or an electric field. The interatomic structure of ultracold atoms can be investigated by the PA spectroscopy method. So far, the PA spectra of two valence electron atoms, obtained using the intercombination transition, have been reported only for Yb [Toj06, Eno08b] and ^{88}Sr [Zel06]. The PA spectra near the intercombination line of the AEAs have been theoretically investigated [Ciu04]. The author calculated PA spectra for ^{40}Ca atoms colliding at ultracold temperatures in different temperature ranges. The results indicate that for ^{40}Ca atoms with a temperature of the order of 1 μK and below the PA spectrum should be observable. Importantly, the atomic gas should be Bose-Einstein condensed, otherwise, the line shapes in a PA spectrum would be dominated by natural broadenings such as Doppler broadening due to the narrow linewidth of the intercombination line. Furthermore, Ref. [Ciu04] also discusses the possibility to produce cold ^{40}Ca molecules in the electronic ground state via the PA process.

In 2008, the Yb research group in Kyoto university [Eno08a] successfully controlled the scattering wave function by an optical Feshbach resonance effect using the intercombination transition of ^{172}Yb and ^{176}Yb atoms. They found that the optical Feshbach resonance is especially efficient for an isotope with a large negative scattering length. In the zero energy limit, the scattering length of $^1S_0$ ground state ^{172}Yb atoms is changed by about 30 nm. On the other hand, they also point out that it is also interesting to generate optical Feshbach resonances using the $^1S_0$ to $^3P_{0,2}$ PA transitions, which have narrower lindewidths than the $^1S_0$ to $^3P_1$ transition, and could give much more efficient optical Feshbach resonance effects. Although there is no existing information of these ultranarrow transitions for ^{40}Ca atoms, the information could be observed by the procedure described in Ref. [Yam07] where the author introduces a method to observe the ultranarrow magnetic quadrupole transition $^1S_0$ to $^3P_2$ in the bosonic and fermionic isotopes of Yb atoms.

Collisional properties of two-electron atoms in the ^3P_J metastable states:

Collisional properties of ultracold two-electron atoms in the ^3P_J metastable state is another interesting application for ^{40}Ca atoms. The extremely long-lived $^3P_0$ state especially may play an important role in developing optical clocks such that their relative precision exceeds 10^{-17}. Our previous work [Han06b] has successfully demonstrated the collisional properties of $^3P_2$ metastable ^{40}Ca atoms in a magnetic field. Comparing the results given by the theoretical work [Kok03], we have indicated that besides spin-exchanging collisions, short range interactions of metastable two-electron atoms may have to be taken into account, such as fine-structure changing collisions.

Recently the collisions of two valence electron atoms in the ^3P_J metastable states have been reported in Yb atoms [Yam08] and Sr atoms [Tra09]. Ref. [Yam08] has demonstrated large atomic losses of ultracold dense Yb [$^3P_2$] atoms in an ODT. An ODT is able to trap atoms in all magnetic Zeeman sublevels, therefore it removes m-changing collisional losses in the trap. Accordingly, fine-structure changing collisions between $^3P_2$ atoms are suspected. Ref. [Tra09] studies the collisional properties of ^{88}Sr atoms trapped in a CODT in the $^3P_0$ metastable state. By trapping atoms in the lowest energy level in the metastable state, the possibility of spin-exchanging collisions and fine-structure changing collision can be removed. However, the resulting comparable loss rates for atoms in both the $^3P_2$ and $^3P_0$ metastable states indicate important principle-quantum-number-changing collisions (orbital angular momentum changes) between metastable atoms. This result also excludes the possibility to achieve BECs in metastable states of two-electron atoms.

Thesis Content

In this work I investigate a novel approach for producing cold dense ^{40}Ca samples in the $^1S_0$ ground state and study the evaporative dynamics of ^{40}Ca atoms in the dimple formed by a $^1S_0$ CODT with the aim of reaching a BEC. In contrast to most AEA research groups, in our experiment cold atoms for loading the ODTs are prepared by bi-chromatic MOTs without an application of the narrow intercombination transition.

Our group has explored a particularly efficient method for the production of large samples of ultracold ^{40}Ca atoms exploiting the existence of the extremely long-lived $^3P_2$ metastable state where the sub-Doppler cooling technique is applicable [Gru01, Gru02b]. Despite being the usual drawback of ^{40}Ca atoms, the fact that the principle fluorescence transition is not closed

is an advantage for loading atoms into the $^3P_2$ metastable state. Firstly, the atoms pre-cooled by the Zeeman slower are trapped in the $^1S_0$ singlet-MOT where the strong principle transition from $^1S_0$ to $^1P_1$ at 423 nm is used. 22 % of the atoms are transferred to the $^3P_2$ metastable state via the $^1D_2$ state and are subsequently trapped by the $^3P_2$ triplet-MOT. The $^3P_2$ triplet-MOT uses the infrared transition from $^3P_2$ to $^3D_3$ at 1978 nm. The rest of the atoms directly decay to the $^1S_0$ ground state or return to the $^1S_0$ state via the $^3P_1$ state in 3 ms and are then trapped by the $^1S_0$ singlet-MOT. In order to operate two MOTs simultaneously and to capture most of the atoms in the $^3P_2$ triplet-MOT, the gradient of the magnetic field is optimized and the sizes of MOT beams have been carefully designed. Typically after 3 s of atom loading, there are 2×10^8 atoms with a temperature around 200 μK in the $^3P_2$ triplet-MOT. The corresponding atomic density is of the order of 10^{10} cm^{-3}. The detailed experimental system is described in Chapter 3. The energy levels of the transitions are shown in Figure (1.1).

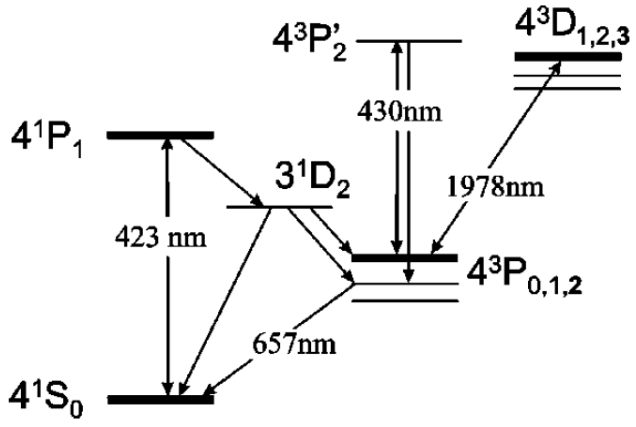

Figure 1.1: Relevant energy levels of ^{40}Ca atoms [Gru02b]. Here ^{3}P'$_2$ is the $^3P_2$ [4p4p] state.

Our previous experimental goal was to achieve a ^{40}Ca metastable BEC. Investigation of the dipolar magnetic interaction is possible using a $^3P_2$ metastable ^{40}Ca BEC due to the large g-factor of the $^3P_2$ states [Doy04, Stu05]. Recent theoretical work [Kok03] indicates that collisions between two metastable AEAs in the presence of external magnetic fields should be largely determinate by partial waves with large angular momenta, even at very low temperature ranges, such as spin-exchanging collisions. The inelastic collision rate is predicted to be comparable to the elastic collision rate at relatively high collisional energies, $T > 100\,\mu$K; however, at lower collisional

energies, $T \sim 1\,\mu$K, the inelastic collision rate is predicted to become substantially larger than the elastic collision rate [Kok03]. Our previous work [Han06b] has confirmed this prediction by studying the collisional properties of metastable $^3P_2$ ^{40}Ca atoms in a minimized Ioffe trap. By analyses of the loss of trapped atoms and a re-equilibration measurement, the inelastic collision and the elastic collision rate are measured, respectively. The results show that inelastic collision rates are comparable to, or even one order of magnitude larger, than the theoretical value. Our results are obtained in magnetic fields varying between 2 and 10 Gauss which are smaller than the applied magnetic fields (of the order of 100 Gauss) used in the theoretical work. Therefore our findings indicate that particularly at low magnetic field, besides values due to the long-range mechanism described in the theoretical work [Kok03], other contributions need to be accounted for such as the potential role of fine-structure changing collisions due to short-range interactions between colliding atoms. Accordingly, inelastic collisions exclude the possibility of implementing evaporation of metastable ^{40}Ca atoms in a magnetic trap.

In order to eliminate these inelastic collisions in a magnetic trap, an ODT is applied. An ODT is able to trap all Zeeman substates of atoms which can remove spin-exchanging collisions and makes evaporation of ^{40}Ca atoms in ^3P_J metastable states possible. Linearly polarized radiation at 532 nm is applied for the ODT, a trap depth of approximately $300\,\mu$K for the $^3P_2$ ($m = \pm 2$) states. The reservoir for the $^3P_2$ ODTs is the atoms in the $^3P_2$ triplet-MOT. Experimentally, unusually short trap lifetimes and low densities of atoms are observed, even for vanishing magnetic field strength. The small number of atoms in the $^3P_2$ ODT comes from the density limited $^3P_2$ triplet-MOT due to the radiation trapping effect, density dependent losses and light assisted collisions in the MOT. Furthermore the short lifetime of the atoms (≈ 20 ms) indicates that other inelastic collisions may need to be taken into account between metastable ^{40}Ca atoms. Recent experimental works have pointed out principle-quantum-number changing collisions [Tra09] and fine-structure changing collisions [Yam08] between metastable AEAs reduce chances of achieving metastable AEA BECs.

In order to achieve a BEC of ^{40}Ca atoms, ^{40}Ca atoms are loaded into the $^1S_0$ ODT. Since the $^1S_0$ state is the absolute ground state, two-body inelastic collisions cannot arise. Since the polarization gradient cooling technique is not applicable in the $^1S_0$ ground state and the intercombination transition is not applicable to our system, the resulting temperature of the atoms in the $^1S_0$ singlet-MOT is in the range of a few mK. This temperature is much higher than the depth of the $^1S_0$ ODT ($350\,\mu$K). Thus, the atoms trapped in the $^3P_2$ triplet-MOT are chosen as the reservoir for the $^1S_0$ ODT. In order to

effectively load atoms trapped in the density limited $^3P_2$ triplet-MOT into the $^1S_0$ ODT, a novel loading scheme has been developed. The study of the novel loading scheme is the topic of Chapter 4.

The novel loading scheme is based upon a spatial energy selective optical pumping transfer. The intensity of the optical pumping beam is kept so small that the transfer is only efficient for slow atoms spending sufficient time in the pumping volume. Thus, the transfer provides significant energy selectivity. The starting point is a moderately cold ($\approx 300\,\mu$K) and dense ($\approx 9 \times 10^9\,\mathrm{cm}^{-3}$) reservoir of $^3P_2$ atoms in the $^3P_2$ triplet-MOT. A linearly polarized laser beam at 532 nm is used as the ODT, which provides negative light shifts in the ^3P_J metastable substates and the $^1S_0$ ground state, except for the $^3P_2$ (m=0) state. The pumping process is done by the linearly polarized laser beam at 430 nm, the so-called pump beam. The pump beam works on the $^3P_2$ [4s4p] to $^3P_2$ [4p4p] transition. In order to only pump $^3P_2$ atoms located within the volume of the ODT, the pump laser, which has a intensity lower than the saturation intensity, is shaped to match the profile of the ODT beam. The atoms are pumped to the $^3P_1$ [4p4p] ODT and further spontaneous decay to the $^1S_0$ ODT within 0.42 ms. The volume of the ODT perpetually refills the $^3P_2$ atoms from the $^3P_2$ triplet-MOT, thus providing a continuous stream of cold atoms in to the ODT before the $^3P_2$ population of the $^3P_2$ triplet-MOT is exhausted.

Typically 5×10^5 atoms with a peak atomic density of $3.5 \times 10^{10}\,\mathrm{cm}^{-3}$ are loaded in the $^1S_0$ ODT. The initial axial and radial temperatures of the atoms are $300\,\mu$K and $85\,\mu$K, respectively. After 50 ms of plain evaporation, there are 10^5 atoms with nearly equal radial and axial temperatures close to $40\,\mu$K and a peak density of $5 \times 10^{11}\,\mathrm{cm}^{-3}$. In order to understand the dynamics of the atoms, numerical models have been developed. Despite the dramatic difference between the trap volumes of the $^3P_2$ triplet-MOT and the ODT, a dense and cold atomic ensemble in the $^1S_0$ ODT is obtained. An image of the ODT is illustrated in Figure (1.2(A)).

The new continuous loading scheme produces a dense and cold atomic ensemble in an ODT and provides an opportunity to pursue a BEC in the $^1S_0$ ground state. One of the observations in Chapter 4 is that the resulting phase space density (PSD) of the atoms in the $^1S_0$ ODT does not increase after 2 s of trap holding time. Therefore, forced evaporation is applied afterwards. The purpose of application of forced evaporation is to maintain a constant or increasing elastic collision rate. It is carried out by continuously ramping down the threshold for evaporation. However, a single beam ODT is not a good candidate for forced evaporation because the weak axial confinement results in a decreased density of the atomic ensemble, causing a reduction of the evaporative rate. Consequently, the elastic collision rate decreases

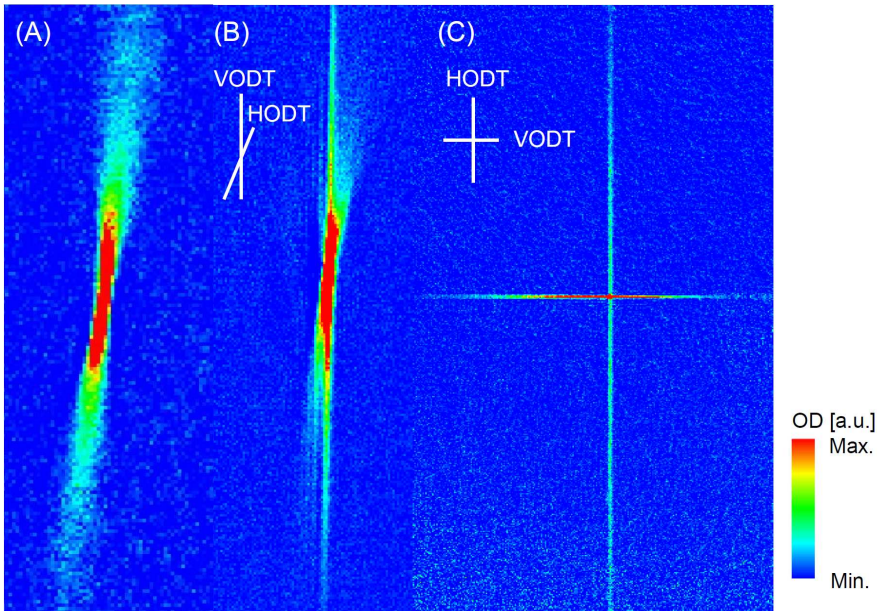

Figure 1.2: Images of the $^1S_0$ ODTs. (A) is the image of the ODT at 532 nm taken by the CCD chip at position 1, see Figure (3.2(A)). The ODT is used for studies of the loading scheme. (B) and (C) are images of the CODT taken by the CCD camera at positions 1 and 2, individually, see Figure (3.2). The HODT and VODT are the ODTs at 1064 nm and 532 nm. The experimental setup is described in Chapter 3.

yielding a stagnation of evaporation. To avoid this drawback, a CODT is utilized.

The CODT system follows the setup for ^{174}Yb atoms [Tak03]. A circularly polarized laser beam at 1064 nm is used as the HODT. A linear polarized laser beam at 532 nm is used as the VODT. The CODT provides approximately 1 mK of the well depth of the dimple. Two narrow pump beams are applied for loading atoms. Typically there are 2×10^5 atoms trapped in the dimple at the temperature of 120 μK when the novel loading scheme is applied. The peak density of the atoms has been successfully increased to the order of $10^{14}\,\mathrm{cm}^{-3}$. The results of experiments with the CODT are presented in Chapter 5 and 6. The characteristics of the CODT are presented in the first part of Chapter 5. Images of the CODT are illustrated in Figures (1.2(B)) and (1.2(C)). Experimentally, after the loading phase is terminated, some atoms remain in the non-crossed region of the CODT, the so-called wings of the CODT. These atoms hamper studies of the dynamics of the atoms trapped in the dimple because the system is not in the equilibrium state.

The atoms in the wings may still load into the dimple via elastic collisions. To study the effect of the atoms in the wings upon the atoms trapped in the dimple, a numerical model is applied. The results of modeling are shown in the second part of Chapter 5.

In Chapter 6, the results of evaporation are demonstrated. Firstly two evaporation schemes previously applied for Yb [Tak03] and Ca [Kra09] are studied, which were successfully applied to atomic samples with densities and temperatures comparable with our initial sample. The observations are then used to find the evaporation strategy optimal for our specific case. Utilizing the newly designed strategy, the highest obtained PSD of the trapped atoms is 0.146. Experimentally, a further increase could not be realized due to a fast loss of particles arising at the end of evaporation independent of the specific protocol used. In order to investigate the experimental limits, the theoretical model is developed which is based on the famous work by O. J. Luiten [Lui96]. This model suggests that the observed fast particle loss is independent of the density, which excludes collisions as its cause. A strong dependence of the trap depth is found which suggests that residual stray light heating might be the underlying mechanism.

The outline of this thesis is as follows:

Chapter 2: the theoretical concepts used in this work are introduced in this chapter. In addition, an analysis of our absorption imaging system indicates the limitations for observing a condensate.

Chapter 3: the experimental setup is illustrated in this chapter which mainly focuses on the modifications to the system.

Chapter 4: the study of the new loading scheme is demonstrated in this chapter. Besides experimental observations, two numerical models are applied for quantitative studies of loading and decay dynamics.

Chapter 5: the characteristics of the CODT are presented in this chapter. Experimentally, some atoms remain in the wings of the CODT after the loading process is terminated. The atoms impede studies of the dynamics of atoms in the dimple due to the fact that the system is not in equilibrium. In order to investigate the effect of the atoms in the wings upon the atoms in the dimple, a theoretical model is applied.

Chapter 6: the results of evaporation of the atoms are presented. In addition, a theoretical model is applied to understand the evaporative dynamics of the atoms.

Chapter 7: This chapter describes the next experimental goal of our research.

Chapter 2

Theoretical Background

This chapter gives a brief overview of the theoretical concepts used in this thesis. The first section introduces the principle of operation of MOTs and the radiation trapping effect. Since the radiation trapping effect plays an important role for the density limited $^3P_2$ triplet-MOT in our system, understanding these concepts are necessary. The second section describes ODTs which includes calculations of optical potentials and the effects by gravity. The following two sections describe the principle of evaporative cooling and discuss collisions in the system. The necessary condition for evaporative cooling is that the time of re-thermalization has to be shorter than the lifetime of the atoms. The lifetime of the atoms is typically limited by inelastic collisions. Therefore, a discussion of inelastic collisions is needed. The final section introduces how the absorption imaging method is used to detect the characteristics of atoms. In addition, the limitations of the imaging system are discussed in order to explain the difficulties in detecting a small atomic ensemble in the CODT.

2.1 Magneto-Optical Trap

2.1.1 Principle of Operation

A MOT, first demonstrated in 1987 [Raa87], is the most widely utility used for trapping neutral atoms. It combines three pairs of counter-propagating laser beams with opposite circular polarization and an inhomogeneous magnetic field. Two coils arranged in the anti-Helmholtz configuration generate a magnetic field which increase from the center of the trap outwards. The beams propagate along three orthogonal axes and intersect at the minimum of the magnetic quadrupole field.

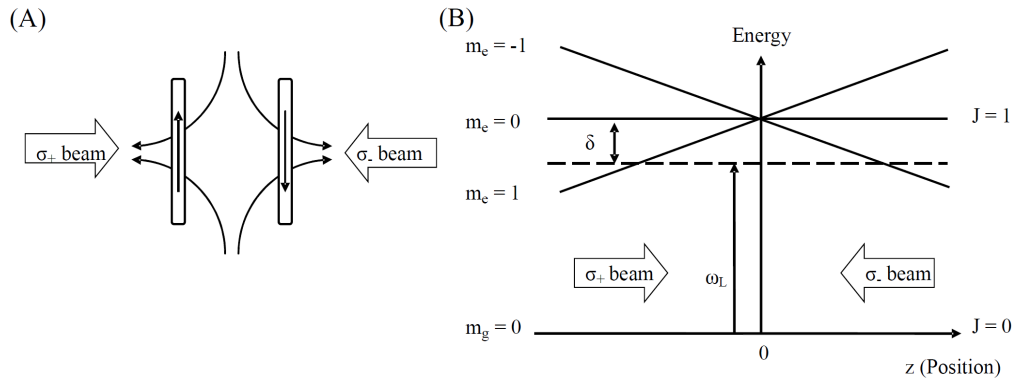

Figure 2.1: Plot (A): One-dimensional MOT configuration. It shows the configuration of a one-dimensional MOT with a pair of counter-propagating circularly polarized beams, and two coils arranged in the anti-Helmholtz configuration. Plot (B): Energy levels in a spatially varying field. The figure shows that two counter-propagating beams of opposite polarization drive a J = 0 to J = 1 transition in a magnetic quadrupole field where the excited state energy levels shift in frequency due to the Zeeman effect. The beams are red detuned by δ MHz with respect to the zero field resonance. The frequency detuning is plotted with a horizontal dashed line. An explanation is provided in the text.

The operational principle of a MOT can be understood by using a one-dimensional illustration shown in Figure (2.1). When an atom is approaching from a positive z-direction through the trap, the Zeeman effect shifts the atoms's frequency onto resonance with a σ_- laser from the right. The atom is driven toward to the center of the magnetic field. Moreover, a moving atom experiences a Doppler shift resulting in a velocity dependent force that opposes its motion, see Equation (2.3). Therefore, an atom experiences a force leading to efficient cooling and trapping.

The scattering force of a single laser beam interacting with neutral atoms in a two-level system is given by

$$F_{scat} \;=\; \hbar k \frac{\rho_{ee}}{2}\,\Gamma \tag{2.1}$$

where

$$\begin{aligned} \rho_{ee} &= s_0/(1+s_0+(2\delta/\Gamma)^2) \\ s_0 &\equiv 2\Omega^2/\Gamma^2 \;=\; I/I_s \\ I_s &\equiv \pi hc/(3\lambda^3\tau)\,. \end{aligned} \tag{2.2}$$

Equation (2.1) shows that the scattering force is given by the momentum kick of a single photon multiplied by the scattering rate. ρ_{ee} is the population of the excited state, $\hbar k$ is the momentum of a photon, Γ is the spontaneous decay rate, δ is the detuning, s_0 is the on resonance saturation parameter, Ω is the Rabi frequency, I_s is the saturation intensity and $k = 2\pi/\lambda$ is the wavenumber, where λ is the wavelength of the beam.

In the low intensity limit, the net force on an atom is simply the sum of the force from each individual beam. Notice, we use the one-dimensional case here. In the limit of small velocities and small Zeeman shifts, the net force experienced by an atom depends on the atomic velocity v and the position z, and is given by

$$F(v,z) = \frac{4\hbar k s_0(2\delta/\Gamma)(kv+\beta z)}{(1+(2\delta/\Gamma)^2)^2} \tag{2.3}$$

where m is the mass of an atom, kv is the Doppler shift and βz is the Zeeman frequency shift. $\beta = dB/dz$ is the gradient of the magnetic field where B is the magnetic field.

An equation of motion can be expressed as an ordinary differential equation,

$$\ddot{z} + \gamma_{damp}\dot{z} + {\omega_{trap}}^2 z = 0 \tag{2.4}$$

where

$$\begin{aligned} \gamma_{damp} &= \frac{4\hbar k^2 s_0(2\delta/\Gamma)}{m(1+(2\delta/\Gamma)^2)^2} \\ {\omega_{trap}}^2 &= \frac{4\hbar k s_0(2\delta/\Gamma)\beta}{m(1+(2\delta/\Gamma)^2)^2} \end{aligned} \tag{2.5}$$

where ω_{trap} is the MOT oscillation frequency. The atomic motion in a MOT is strongly damped since $\gamma_{damp}^2/(4\,{\omega_{trap}}^2) \gg 1$. ω_{trap} and γ_{damp} have a relative maximum at $\delta = \text{-}\Gamma/2$, the laser detuning is optimized, and at $\Omega = \Gamma$, the laser intensity is optimized.

2.1.2 Capture Range

The capture range of a MOT is defined as the spherical region around the trap center (with radius R_c) outside of which no atoms can interact with the light field. The maximum velocity of the atoms that can be captured by the trap is determined by the red detuning δ of the laser beams with respect to the zero field resonance and the gradient of the trap's magnetic field.

The decelerated atoms entering the trap are shifted onto the resonance with the laser beam by the magnetic field which increases from the trap

center outwards. At a distance from the center, the Zeeman effect shifts the resting atoms onto resonance. Therefore, R_c can be calculated by

$$kv_{max} = 2 \times \beta R_c = \widetilde{\delta}\,\widetilde{\Gamma} \tag{2.6}$$

where $\widetilde{\Gamma} \equiv \Gamma(1 + 2(\Omega/\Gamma)^2)^{1/2}$ is the power broadening linewidth and $\widetilde{\delta} = \delta\,(\widetilde{\Gamma}/2)^{-1}$ is the power weighted detuning.

2.1.3 Cooling Limits

In Doppler cooling theory [Ste86], the temperature limit of Doppler laser cooling arises from the competition between the damping force and heating. This heating is caused by the randomness of spontaneous emission and absorption shot noises. The temperature limit is given by the condition of zero detuning and low laser intensity below the onset of the saturation since the excited state population cannot exceed half of the trapped atoms.

The Doppler temperature T_D is written as

$$T_D = \frac{\hbar\Gamma}{2k_B} \tag{2.7}$$

where k_B is the Boltzmann constant.

Another temperature limit is the recoil temperature T_R. For atoms moving in a spatially varying light field, optical pumping acts to adjust the atomic orientation to the changing conditions of the light field. For example, consider two counter-propagating laser beams with orthogonal polarization. The resulting light field has a polarization that varies on the wavelength scale along the direction of the laser beam. i.e., Sub-Doppler cooling.

If the momentum transfer due to absorption of a photon brings an atom to a complete halt, the inevitable spontaneous emission causes a momentum kick of $\hbar k$. The atom has a final velocity which is a minimum of $\hbar k/m$ and its temperature is

$$T_R = \frac{(\hbar k)^2}{m k_B}\,. \tag{2.8}$$

2.1.4 Radiation Trapping Effect

Although a MOT is the most versatile kind of atom trap with wide applicability, a limited atomic density is a challenge which must be overcome. The density is limited to approximately $10^{11}\,\mathrm{cm}^{-3}$ due to the fluorescent light emitted by some trapped atoms being absorbed by others [Wal90, Ses91] and due to collisions between the atoms.

After passing through an on resonant atomic ensemble with a density n, the change in laser intensity I along the z-direction is given by

$$\frac{dI}{dz} = -\sigma_{sc} n I \tag{2.9}$$

where the on resonance scattering cross-section σ_{sc} is

$$\sigma_{sc} = \frac{3\lambda^2}{2\pi} \tag{2.10}$$

$I(z) = I_0 \exp(-\sigma_{sc} n z)$ is the intensity loss in the z-direction. It has to be noted that the scattering cross section is of the order of λ^2. The re-absorption of spontaneously emitted light causes a repulsion force between atoms, see Equation (2.1).

Comparing the $^3P_2$ triplet-MOT in our system with a MOT in a ^{87}Rb system, the scattering cross section of a laser beam at 2 μm is 6.5 times bigger than that of a beam at 780 nm. As a result, the radiation trapping effect is a significant issue for the $^3P_2$ triplet-MOT of ^{40}Ca atoms.

2.2 Optical Dipole Traps

2.2.1 Optical Potential

The optical dipole force arises from the dispersive interaction of an induced atomic dipole moment with an intensity gradient of a light field. Due to its conservative character, the force can be derived from a potential where its minimum can be used for atom trapping. The absorptive part of the dipole interaction in far-detuned light leads to residual photon scattering of the trapping light which causes loss and heating of trapped atoms.

Using the oscillation model described in [Gri00] **for two-level atoms**, the dipole potential U_{dip} and the photon scattering rate Γ_{sc} for large detuning and negligible saturation are given by

$$U_{dip}(\vec{r}) = -\frac{3\pi c^2}{2{\omega_{ot}}^3}(\frac{\Gamma}{\omega_{ot}-\omega_l}+\frac{\Gamma}{\omega_{ot}+\omega_l})I(\vec{r}) \tag{2.11}$$

$$\Gamma_{sc}(\vec{r}) = \frac{3\pi c^2}{2\hbar{\omega_{ot}}^3}(\frac{\omega_l}{\omega_{ot}})^3(\frac{\Gamma}{\omega_{ot}-\omega_l}+\frac{\Gamma}{\omega_{ot}+\omega_l})^2 I(\vec{r}) \tag{2.12}$$

where ω_l denotes the laser frequency, ω_{ot} denotes the frequency of the optical transition, $I(\vec{r})$ denotes the intensity of the dipole trap laser beam, Γ is the spontaneous decay rate and c denotes the speed of light.

For multi-level atoms, the state dependent ground state dipole potential is calculated by the AC Stark shift of the ground state given by

$$U_{dip}(\vec{r}) = \frac{-3\pi c^2}{2{\omega_{ij}}^3} I(\vec{r}) \times \sum_j {c_{ij}}^2 \Gamma(\frac{1}{\omega_{ij}-\omega_l}+\frac{1}{\omega_{ij}+\omega_l}) \tag{2.13}$$

here ω_{ij} are the frequencies of optical transitions where i and j represent the ground state and the excited state, respectively. The transition coefficient c_{ij} is equal to $\langle e_j | \mu | g_i \rangle / \|\mu\|$ with the reduced matrix element $\|\mu\|$, where μ is the operator of the dipole moment. The transition coefficient c_{ij} takes into account the coupling strength between the electronic ground state $|g_i\rangle$ and the excited state $|e_j\rangle$ which depends on laser polarization as well as the electronic and nuclear contributions to angular momentum. The state dependent ground state potential is given by contributions from all excited states coupling to it.

In this thesis, the rotating-wave approximation is not applied. The difference in detuning between ω_l and ω_{ij} is not small enough. The condition for the rotating-wave approximation is $\omega_{ij} \gg |\omega_l - \omega_{ij}|$.

For a Gaussian beam with total power P, the intensity as a function of axial position z and radial position r is given by

$$I(r,z) \;=\; \frac{2P}{\pi w(z)^2}\exp(-\frac{2\,r^2}{w(z)^2}) \tag{2.14}$$

where $\omega(z) = \omega_0\sqrt{1+(z/z_R)^2}$ represents the $1/e^2$ radius of the beam which depends on z. The minimum ω_0 is located in the focal plane of the beam at $z = 0$. It is commonly referred to as the beam waist. $z_R = \pi{\omega_0}^2/\lambda$ is the Rayleigh length and λ is the wavelength of the laser beam.

At the position of the beam focus ($z = r = 0$), the trap depth is given by U_0 which does not consider the gravitational potential. Assuming the thermal energy k_BT of atoms is much smaller than U_0, the atoms will be confined in the trap. This condition holds for positions $z_R \gg z$ and $\omega_0 \gg r$. The optical potential can be well approximated by a simple cylindrically symmetric harmonic oscillator

$$U_{dip}(r,z) \cong -U_0[1-2(\frac{r}{\omega_0})^2-(\frac{z}{z_R})^2] \tag{2.15}$$

where the minus sign is a result of the red detuning assumed here.

The potential depth U_0 is a positive quantity, and if the approximation for Equation (2.15) holds, the trap frequencies of the harmonic potential calculated by Equation (2.13) can be derived

$$\begin{aligned} \omega_{rad} &= \sqrt{4U_0/(m{\omega_0}^2)} \\ \omega_{ax} &= \sqrt{2U_0/(m{z_R}^2)} \end{aligned} \tag{2.16}$$

where m is the mass of the atom, ω_{rad} and ω_{ax} are the trap frequencies in the radial and in the axial direction, respectively.

2.2.2 Gravitational Sag

For an ODT beam propagating in the direction of gravity, the total potential is modified by the gravitational potential due to the small restoring force along the axis. Usually, the potential at the the center can still be approximated as harmonic, but the center will be shifted away and the whole potential is tilted along the axis of gravity. In the case of a shallow optical potential, the potential may even vanish due to gravity.

Taking into account the gravitational potential, the total potential for the case of a beam propagating along the axis of gravity z is given by

$$U_{total}(r,z) \;=\; -U_0\exp(-2\frac{r^2}{{\omega_0}^2})\exp(-\frac{z^2}{{z_R}^2}) \;+\; mgz \tag{2.17}$$

here $g = $-9.81 m/s^2 is the gravitational acceleration.

Figure (2.2) shows total potentials calculated using Equation (2.17). The calculations are computed using π-polarized radiation at 532 nm with a Gaussian radius of 15.8 μm. The black solid line shows the $^1S_0$ optical potential for a beam power of 3.2 W where the gravitational potential is excluded. The red solid line and the blue solid line give the total potential in the $^1S_0$ state for powers of 3.2 W and 0.32 W, respectively.

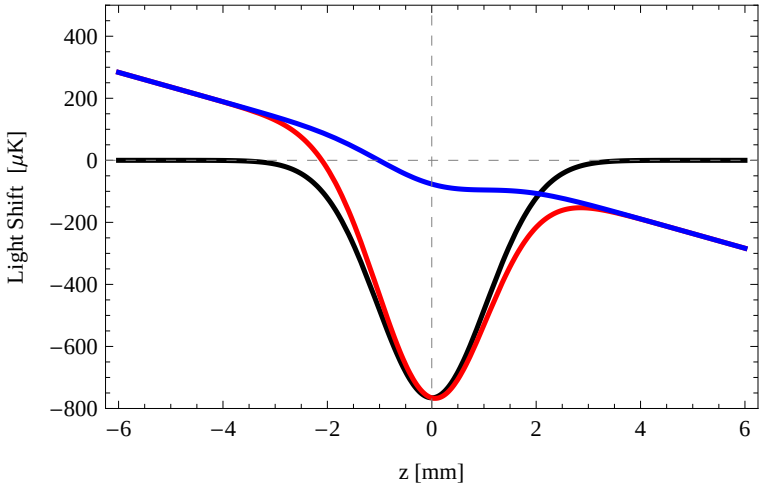

Figure 2.2: Optical potentials at the $^1S_0$ state. The calculations are computed using 532 nm radiation which is π-polarized and a 15.8 μm Gaussian radius. The black solid line shows the $^1S_0$ optical potential for a power of 3.2 W where the gravitational potential is excluded. The red solid line and the blue solid line give total potentials in the $^1S_0$ state for powers of 3.2 W and 0.32 W, respectively.

Comparing the red and black solid lines, one can see that gravity shifts the center of the optical potential away from the center and tilts the potential along the direction of gravity. Moreover, comparing the red and the blue solid lines, for the weaker optical potential the center of the optical potential is shifted further from the center and the confinement minimum vanishes, due to gravity.

2.3 Theory of Evaporative Cooling

2.3.1 Introduction to Evaporation

A PSD of the order of unity is a necessity for observing a BEC. The exact value depends on the geometry of the trap. For atoms trapped in a three-dimensional harmonic trap, the PSD can be expressed by

$$PSD \equiv n{\lambda_{th}}^3 \approx 1.202 \tag{2.18}$$

here $n = N\overline{\omega}^3 m^{3/2}/(2\pi k_B T)^{3/2}$ is the peak density of the atoms and $\lambda_{th} = \sqrt{2\pi\hbar^2/(mk_B T)}$ is the de Broglie wavelength of the atoms where $\overline{\omega}$ is the mean geometric trap frequency. Equation (2.18) indicates that the atomic ensemble has to have a sufficiently low temperature and a sufficiently high density to obtain a condensed state.

MOTs and ODTs can generate an atom ensemble with a high density and a low temperature, but the atomic ensemble is still far away from the BEC state. This is because the temperature of atoms is not low enough. In order to further reduce the temperature of the atoms, the method of evaporative cooling is essential. The evaporative cooling process is based on the removal of the atoms with a thermal energy which is higher than the average energy. The remaining atoms in the trap re-thermalize due to elastic collisions and then reach a lower temperature.

The main condition for evaporative cooling is that the time for re-thermalization to occur is significantly shorter than the lifetime of the trapped atoms. The time for re-thermalization is affected by elastic collisions between the atoms. The lifetime of the trapped atoms is typically dominated by inelastic collisions. The continuous thermalization process replenishes the high energy tail of a Boltzmann distribution. When the temperature of the atoms decreases, the probability of evaporation reduces approximately as $\exp(-U/(k_B T))$, where U is the finite trap depth. Eventually, the evaporation process stagnates due to competition between cooling processes and heating processes. In order to maintain a constant or increasing elastic collision rate, forced evaporation is needed. It is implemented by continuously ramping down the threshold for evaporation.

For an ODT, forced evaporative cooling is carried out by ramping down the power of the laser beam. However a single beam ODT is not a good candidate for forced evaporation as the weak axial confinement results in a decrease in the density of the atomic sample. This then causes a reduction in the rate of evaporation and, consequently, yields the stagnation of evaporation. To avoid this drawback, a CODT is utilized. One configuration for a CODT uses two ODTs where their foci are intersected. It provides extra

confinement along the beam axes and removes the drawback from a single beam ODT setup for forced evaporation. A detailed review of evaporative cooling of trapped atoms can be found in [Ket96, Wal96].

2.3.2 Elastic Collisions

When the temperature of the trapped atoms is sufficiently low such that high partial waves do not contribute to the scattering cross section, the elastic collision rate Γ_{el} of an atom in the center of three-dimensional harmonic trap can be expressed by the s-wave approximation [Ket96]

$$\Gamma_{el} = \frac{n}{\sqrt{8}} \sigma_t \overline{u} \tag{2.19}$$

where n is the peak density of trapped atoms in a harmonic trap. σ_t is the elastic scattering cross section, and $\overline{u} = 4\sqrt{k_B T/(\pi m)}$ is the mean relative velocity, which are both dependent on the energy.

Without considering the interaction potential in detail, the elastic scattering cross section, which is with energy dependent, is given by

$$\sigma_t = \frac{8\,\pi\,a^2}{(k_{th}\,a)^2 + 1} \tag{2.20}$$

where $k_{th} = m\overline{u}/(2\hbar)$ is the thermal wave vector and a is the scattering length. $\sigma_0 = 8\pi a^2$ is the elastic scattering cross section, which is independent of the energy.

2.3.3 Speed of Evaporation

Following Ref. [Ket96], for a large value of truncation parameter η, the rate of evaporation is

$$\Gamma_{ev} = \frac{n}{4} \sigma_t \overline{u} \exp(-\eta)\,\eta \tag{2.21}$$

where η is defined by $U/(k_B\,T)$ and U is the trap depth.

This is the rate that elastic collisions produce atoms with energy larger than $\eta k_B T$ in a untruncated Boltzmann distribution. It is due to that in a untruncation Boltzmann distribution, every evaporation involves an atom in the high-energy tail removes the other atoms from the high-energy tail [Ket96].

2.3.4 Effective Evaporation

The success of evaporative cooling depends on whether the atoms will be sufficiently cooled before all of the atoms are lost from the trap. A quantitative measure generally known as α_{EV} is defined as the ratio of the rate of change in temperature to rate of change in number

$$\alpha_{EV} = \frac{d \ln T}{d \ln N} \tag{2.22}$$

where T denotes the temperature of the atoms and N denotes the number of atoms.

For experimental considerations, the ultimate goal is to increase the PSD of the atoms while losing as few atoms as possible. Stated quantitatively, the ratio between the change in PSD to the change in atom number should be considered [Ket96]

$$\gamma_{EV} = -\frac{d \ln PSD}{d \ln N}\,. \tag{2.23}$$

For a successful evaporative cooling process, it is important to maintain or increasing elastic collision rate to sustain the evaporation. The regime where this is the case is known as 'runaway evaporation'. In the case of a three-dimensional harmonic trap, the runaway condition is satisfied when α_{EV} and γ_{EV} are larger than 1 [Ket96].

2.4 Collisions of Trapped Atoms

The time evolution of the total atom number N can be described by

$$\dot{N} = -\Gamma_{BG}\, N - \Gamma_{el}\, N - \Gamma_{3B}\, N \tag{2.24}$$

here Γ_{BG}, Γ_{el} and Γ_{3B} are the background, two-body elastic and three-body collision rates, respectively. Γ_{el} was introduced in the last section. Two-body inelastic collisions are excluded in this thesis because the atoms in the ODTs reside in the absolute ground state of ^{40}Ca atoms. A detailed introduction of collisions of ultracold atoms can be found in [Dal98].

Background Collisions

The background collision rate Γ_{BG} takes into account collisions between hot background atoms in the vacuum and the atoms in the trap. If one only considers losses due to background collisions, Equation (2.24) can be solved by a simple exponential decay curve

$$\dot{N} = N_0 \exp(-t/\tau_{BG}) \tag{2.25}$$

where $\tau_{BG} = 1/\Gamma_{BG}$ denotes the 1/e lifetime and N_0 denotes the initial atom number. τ_{BG} is approximately 1 s for atoms trapped in an ODT with a vacuum pressure of 3×10^{-9} mbar.

Three-Body Collisions

When the density of the atoms reaches the order of $10^{14}\,\mathrm{cm}^{-3}$, three-body collisions play an important role not only causing losses but also leading to heating of the trapped atoms. The three-body collision rate Γ_{3B} mentioned in Equation (2.24) is given by

$$\Gamma_{3B} = \frac{L_{3B}}{\sqrt{27}}\, n^2 \tag{2.26}$$

where L_{3B} is the three-body loss coefficient.

When three atoms are close to each other, two of them may form a dimer or a molecule while the third atom carries away the released energy. The molecule and the third atom receive $\mathrm{E}_b/3$ and $2\mathrm{E}_b/3$, respectively, where $\mathrm{E}_b = \hbar^2/(ma^2)$ is the binding energy of the universal dimer state. For an atom with a large scattering length, such as ^{40}Ca atoms, the binding energy of the weakest bound state is significantly lower than the trap depth which is of the order of $10\,\mu$K. Therefore, after such collisions, the third atom is not immediately lost from the trap but may distribute this energy among the trapped ensemble [Web03a, Kra09]. Besides, due to the n^3 dependence, three-body losses predominantly occur at the trap center where atoms carry an energy less then the average. Thus, three-body collisions provide a significant heating mechanism of cold ^{40}Ca atoms.

Taking into account the three-body collisional loss in the system only, Equation (2.24) can be solved. The corresponding 1/e three-body half time τ_{3B} is given by

$$\tau_{3B} = \frac{1}{2\, L_{3B}\, n^2}\,. \tag{2.27}$$

Given an ensemble of ^{40}Ca atoms with a density of $5\times10^{14}\,\mathrm{cm}^{-3}$ and L_{3B} of $10^{-27}\,\mathrm{cm}^6\mathrm{s}^{-1}$ [Kra09], the resulting τ_{3B} is 2 ms. Thus, for a dense ^{40}Ca atomic ensemble, three-body collision is an significant issue which may cause losses and lead to heating of the atoms.

2.5 Absorption Imaging

2.5.1 Number of Atoms

Absorption images provide information on the optical density (OD), which is proportional to the atomic density. First, let Equation (2.28) be the column number density $\widetilde{n}$ along the axis of the imaging beam (z-direction)

$$\widetilde{n}(x,y) \;=\; \int n(x,y,z)dz\,. \tag{2.28}$$

The column number density is related to the OD by

$$OD(x,y) \;=\; \widetilde{n}(x,y)\frac{\sigma_{sc}}{1+\delta^2} \tag{2.29}$$

where frequency detuning is $\delta = \Gamma/2$. The imaging beam at 423 nm is on resonance with the optical transition in our experiments. i.e., $\delta = 0$.

Now, consider a number density distribution with a Gaussian shape along the imaging beam axis, i.e.,

$$\widetilde{n}(\vec{r}) \;=\; n_0(x,y)\exp(\frac{z^2}{{\sigma_z}^2}) \tag{2.30}$$

where the peak density is $n_0(x,y)$ and σ_z is the Gaussian radius of the cloud along the axis of the beam.

Combining Equations (2.28), (2.29) and (2.30), the OD is then given by

$$OD(x,y) \;=\; n_0(x,y)\sigma_{sc}\sigma_z\sqrt{\pi}\,. \tag{2.31}$$

To extract the OD, three successive images are taken with a CCD camera to calculate the fractional absorption of the cloud. Here Beer's law, $I/I_0 \;=\; \exp(-OD(x,y))$, where I is the laser intensity along the beam axis and I_0 is the initial intensity of the beam is used. The first image records the intensity of the shadow of the atoms within the imaging beam, I_{atoms}. The second image takes a bright-field image of the imaging beam without atoms, $I_{no-atoms}$. The third image takes a dark-field image without atoms and without the imaging beam, I_{dark}. This last image accounts for a CCD dark current and a read-out noise as well as any stray light during imaging.

To correct for intensity fluctuations in the imaging beam, the bright-field image is normalized with respect to an area in the images without atoms. The OD is obtained by

$$OD(x,y) \;=\; -\ln(\frac{I_{atoms}-I_{dark}}{I_{no-atoms}-I_{dark}})\,. \tag{2.32}$$

Since only the axial and longitudinal widths, σ_x and σ_y, of the OD can be deduced from images, we evaluate the OD at x = y = 0 to find the peak OD (OD_{peak})

$$OD_{peak} = n_0 \sigma_{sc} \sigma_z \sqrt{\pi} \tag{2.33}$$

and substituting n_0, from the integration of Equation (2.30) into Equation (2.33), the atom number N is given by

$$N = OD_{peak}\, \sigma_x \sigma_y \pi / \sigma_{sc}\,. \tag{2.34}$$

2.5.2 Temperature of Atoms

Time-of-Flight (TOF) measurements allow determination of the temperature of an atomic ensemble. After release from the trap when it is switched off, the atoms follow their last trajectory and ballistically expand. The temperature of the atomic ensemble can be deduced directly from the increase in the cloud's radius over free-flight times.

In **a thermal cloud**, the velocity distribution follows Maxwell's distribution

$$f(v)dv \propto \exp(-\frac{mv^2}{2k_B T})\,. \tag{2.35}$$

Taking the x direction as an example, the density after time t and with velocity $v = x/t$ becomes

$$f(x)dx \propto \exp(-\frac{x^2}{{\sigma_x}^2}) \tag{2.36}$$

where $\sigma_x = \sqrt{2k_B T t^2/m}$ is with atoms of mass m, the Boltzmann constant k_B and the temperature of the ensemble T.

The time dependent width is given by

$$\sigma_x(t) = \sqrt{{\sigma_i}^2 + (\frac{2k_B T}{m})t^2} \tag{2.37}$$

where σ_i is the initial radius of the initial spatial distribution, which is Gaussian in shape. Thus, the temperature of the atomic ensemble can be deduced directly from the increase in the cloud's radius over free-flight times.

2.5.3 Image Analysis

Analysis of the images obtained by the imaging system is a challenge due to the small size of an atomic cloud trapped in a dimple. An image can suffer from limited spatial resolution, vignetting, blurring and a low signal-to-noise ratio (SNR). Therefore, these problems are discussed in detail here.

The following analysis focuses on our experimental system. The setup of the imaging system shown in Figure (3.2) is a one lens system and thus vignetting can be neglected. A limited spatial resolution may become a problem for observing a condensate, while blurring and a low SNR of the imaging system may limit reliability of the measurements.

Resolution

Under realistic experimental conditions even after a free expansion, the size of the atomic ensemble trapped in the dimple is below $60\,\mu$m. In order to detect and measure the atoms, it is important to achieve an imaging system with the best possible optical resolution and a high magnification.

For an ideal imaging system, the diffraction-limited resolution Δl_{min}, the smallest distance a lens can resolve, is given by [Hec98]

$$\Delta l_{min} = 1.22 \frac{f\lambda}{D_{dia}} \tag{2.38}$$

where f is the focal length of the lens, D_{dia} is the diameter of the lens and λ is the wavelength of the light.

The spatial angle of the imaging setup at position 2[1] is restricted by the MOT setup. The effective diameter and the focal length of the lens are approximately 17.6 mm and 250 mm, respectively. Using Equation (2.38), the resulting diffraction-limited resolution is about $7.3\,\mu$m. According to the experimental data, however, the actual resolution is $14\,\mu$m which means that the spatial angle is limited and there are optical aberrations in the lens.

The spatial resolution is significant for TOF measurements, used in particular for BEC observations. Considering a thermal cloud, the initial radius cannot be extracted if the ensemble size is below the imaging system's resolution. However, the temperature of the atomic ensemble still can be detected by fitting the cloud sizes after expansion, see Equation (2.37). In case of a condensate, a change of the aspect ratio occurs indicating the formation of a quantum degenerate gas. However, limited resolution may conceal this information.

[1] see Section (3.1)

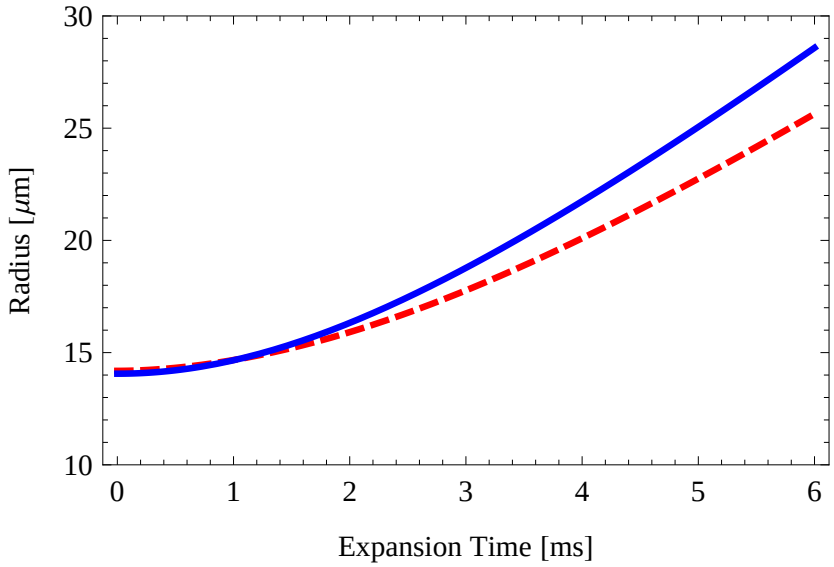

Figure 2.3: Expansion of a condensate released form the trap. The dashed line and the solid line correspond to the radii in the axial and radial directions, respectively. Parameters for calculations are as follows: The radial and axial trap frequencies are $\omega_{\perp,0} = 2\pi \times 508\,\mathrm{Hz}$ and $\omega_{z,0} = 2\pi \times 287\,\mathrm{Hz}$, respectively. The atom number in the condensate is 4400 with a temperature of $0.31\,\mu\mathrm{K}$. The spatial resolution of the absorption imaging is $14\,\mu\mathrm{m}$.

Free expansion of a cigar shaped condensate ($\lambda_{asp} << 1$) released instantaneously from a trap is found [Ket99] to lead to an aspect ratio given by Equation (2.39)

$$\frac{R_\perp(\tau)}{R_z(\tau)} = \frac{\lambda_{asp}\sqrt{1+\tau_e{}^2}}{1+\lambda_{asp}{}^2[\tau_e \arctan\tau_e - \ln\sqrt{1+\tau_e{}^2}]} \tag{2.39}$$

here $R_\perp = R_x = R_y$ and R_z are the radii of the condensate in the radial and axial directions of the trap, respectively. λ_{asp} is the aspect ratio of the trap given by the ratio of the axial and radial trap frequencies. τ_e is equal to the radial trap frequency multiplied by the expansion time.

Now, including a finite spatial resolution, the radius changes with respect the expansion time, and is given by

$$R_{ir}(\tau) = \sqrt{\Delta l_{min}{}^2 + R_i(\tau)^2} \tag{2.40}$$

where $i = \perp, z$. R_{ir} is radius of the condensate when considering a limited resolution Δl_{min}.

Expansion of a condensate released from the trap are shown in Figure (2.3). Parameters for calculations are as follows. The radial and axial trap frequencies are $\omega_{\perp,0} = 2\pi \times 508\,\mathrm{Hz}$ and $\omega_{z,0} = 2\pi \times 287\,\mathrm{Hz}$, respectively. The atom number in the condensate is 4400 with a temperature of $0.31\,\mu\mathrm{K}$. The spatial resolution of the absorption imaging is $14\,\mu\mathrm{m}$. The dashed line and the solid line correspond to the radii in the axial and radial directions, respectively. Therefore, evidently, the feature of a condensate, an inversion of aspect ratio, cannot be observed by the imaging system due to the limited resolution.

Blurring

Blurring occurs because of recoil-induced motion of atoms while an image is taken. Following the description of [Ket99], if an atom scatters N_p photons in a period Δt, the random velocity of the atom leads to a random position shift γ_{rms} given by

$$\gamma_{rms} = \frac{v_{rms}\Delta t}{\sqrt{3}} = \sqrt{\frac{N_p}{3}} V_{rec} \Delta t \tag{2.41}$$

where v_{rms} is the random velocity of atoms and V_{rec} is the recoil velocity of a single photon.

Taking into account the experimental parameters (the intensity of the imaging beam is $2.64\,\mathrm{W/m^2}$ and the exposure time is $30\,\mu\mathrm{s}$), the resulting γ_{rms} is $1.5\,\mu\mathrm{m}$. On the other hand, assuming the intensity of the imaging beam reaches its saturation intensity ($59.9\,\mathrm{mW/cm^2}$ for the 423 nm laser beam), the resulting γ_{rms} is $13.2\,\mu\mathrm{m}$, which is much larger than the pixel size of the CCD Chip at position 2. Therefore, the intensity of the imaging beam should remain low enough to avoid any visible blurring.

Signal-to-Noise Ratio

The SNR of a CCD sensor is given by the ratio of generated charge carriers (signal electrons) to the number of unwanted charge carriers (noise electrons) [PCO].

The signal electron number is dependent on the intensity of incoming photons, described by

$$n_{signal} = \frac{I}{h\nu}\, t\, A\, \eta_{ef} \tag{2.42}$$

with the light intensity I, the photon energy $h\nu$, the exposure time t, the pixel area A and the quantum efficiency η_{ef}.

Noise usually comes from three main sources: shot noise, CCD image sensor noise and read-out noise.

The number of shot noise electrons of a CCD sensor is given by

$$n_{photon} = \sqrt{\frac{I}{h\nu} t A \eta_{ef}} . \tag{2.43}$$

Taking into account these sources of noise, the SNR is given by

$$\frac{S}{N} = \frac{n_{signal}}{\sqrt{n_{photon}^2 + n_{CCD}^2 + n_{read-out}^2}} \tag{2.44}$$

where, n_{CCD} is the number of CCD image senor noise electrons, only taking into account the dark current here. $n_{read-out}$ is the number of read-out noise electrons.

In order to calculate the SNR of the imaging system, the following parameters are used. I is $2.64\,\mathrm{W/m^2}$, t is $30\,\mu$s, the pixel size is $3.2\,\mu$m, η_{ef} of the CCD sensor at 423 nm is approximately 0.35, $n_{read-out}$ is 13 electrons per image and n_{CCD} is 20 electrons per pixel, per second at 20° C. Thus, the SNR of one pixel of the imaging system calculated by Equation (2.44) is 60. Comparing with values of n_{photon}, n_{CCD} and $n_{read-out}$, the SNR is dominated by shot noise. The SNR of the imaging system for one pixel is considered due to the fact that the image size of the atomic sample in the dimple is about one pixel after evaporation.

Chapter 3

Experimental Setup

This chapter outlines the experimental setup and mainly focuses on describing the modifications and discussing the experimental challenges. The general setup of the MOT systems, the vacuum system and the beam transfer system are described in the works of Jan Grünert [Gru02a] and Dirk Hansen [Han06a].

3.1 Experimental Overview

The experimental procedures during the MOT phases of the experiment are described in [Gru01, Gru02b]. The relevant transitions of the system are plotted in Figure (3.1). A Zeeman-cooled atomic beam is used to load the $^1S_0$ singlet-MOT as a starting point. The $^1S_0$ singlet-MOT uses the strong principal transition from $^1S_0$ to $^1P_1$ at 423 nm for which Γ is $2\pi \times 34.6$ MHz. Since this transition is not closed, 78 % of the atoms directly decay to the $^1S_0$ ground state or return to the $^1S_0$ state via the $^3P_1$ state in 3 ms and are then trapped by the $^1S_0$ singlet-MOT. The rest of the atoms are transferred to the $^3P_2$ metastable state via the $^1D_2$ state and are continuously trapped by the $^3P_2$ triplet-MOT. The $^3P_2$ triplet-MOT uses the infrared transition from $^3P_2$ to $^3D_3$ at 1978 nm ($\Gamma = 2\pi \times 57$ kHz).

In the experiment, the same magnetic field gradient of 12.5 Gauss/cm is used for both MOTs in order to operate them simultaneously. The value of the magnetic field is a compromise between the best value for the $^1S_0$ singlet-MOT of 60 Gauss/cm and the best value for the $^3P_2$ triplet-MOT which is below 1 Gauss/cm. The optimum magnetic field gradient is decided by the capture range of the MOTs, see Section (2.1.2). In order to operate the $^3P_2$ triplet-MOT with the magnetic field gradient of 12.5 Gauss/cm, the $^3P_2$ triplet-MOT beams are strongly saturated. The saturation parameter

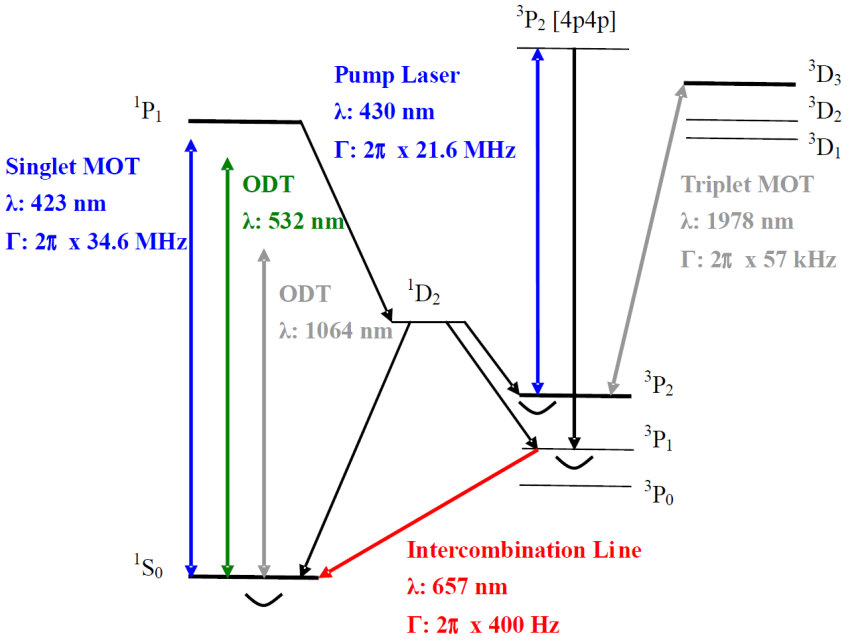

Figure 3.1: The scheme of the relevant energy levels and transitions in ^{40}Ca. It includes the strong principal transition at 423 nm (blue line), the cooling and probing transition for atoms in the $^3P_2$ metastable state at 1978 nm (gray line) and at 430 nm (blue line) as well as the intercombination line at 657 nm (red line). For ODT studies, relevant optical potentials caused by ODT lasers at 532 nm and 1064 nm are shown by parabolic curves. Energy differences are not properly scaled. The details are described in the text.

is about 2000. Moreover, in order to capture the atoms lost from the $^3P_2$ triplet-MOT, the diameter of the $^1S_0$ singlet-MOT laser beams is on the cm scale, which takes into account the atoms' velocities and the decay time to the $^1S_0$ state. Finally, these two MOTs are superposed to load the most of atoms into the $^3P_2$ triplet-MOT.

The absorption imaging method is applied to detect the number and temperature of the atoms in the MOTs, see Sections (2.5) and (3.2.1). The imaging beam at 423 nm is on resonance with the strong principal fluorescence line. To detect the number and temperature of $^3P_2$ atoms in the $^3P_2$ triplet-MOT, the pump laser is applied after the loading process of the $^3P_2$ triplet-MOT is finished. The wavelength of the pump laser is 430 nm ($\Gamma = 2\pi \times 21$ MHz) addressing the transition from $^3P_2$ [4s4p] to $^3P_2$ [4p4p]. The pump laser excites the atoms in the $^3P_2$ triplet-MOT to the $^3P_2$ [4p4p]

state and then subsequently decay to the $^1S_0$ state via the $^3P_1$ state within 0.42 ms. This time period is due to the finite lifetime of the $^3P_1$ state. Afterwards, the absorption imaging beam is applied for measurements. The lifetime of the $^3P_1$ state gives rise to some small undesired expansion of the $^3P_2$ atomic ensemble, which should be accounted for the interpretation of the images obtained. An analogous procedure for imaging is described in our previous work [Han06b, Han06a].

Typically, the vacuum level of the system is about 5×10^{-10} mbar. After 3 s of loading time, there are 2×10^8 atoms at a temperature of 200 μK in the $^3P_2$ triplet-MOT. Its atomic peak density is of the order of 10^{10} cm^{-3}.

The experimental procedure for loading atoms into the $^1S_0$ ODT are described in brief below. A more detailed description is provided in Section (4.1). The atomic reservoir of the ODT is $^3P_2$ atoms in the $^3P_2$ triplet-MOT. While atoms are loaded into the $^3P_2$ triplet-MOT for a few seconds, the $^1S_0$ singlet-MOT loading is terminated and the ODT laser is switched on. The pump laser beam at 430 nm is turned on for loading atoms into the ODT. The pump laser beam, which has an intensity below the saturation intensity, is shaped to match the profile of the ODT in order to pump atoms inside the volume of the ODT only. The foci of the pump beam and ODT beam are well superimposed at the center of the $^3P_2$ triplet-MOT. The atoms are excited from the $^3P_2$ [4s4p] state to the $^3P_2$ [4p4p] state and further decay to the $^1S_0$ ODT via the $^3P_1$ state. After loading is terminated, the number and temperature of the atoms in the $^1S_0$ ODT are detected by the absorption imaging method. Optical potentials related to loading processes of the ODT are shown by the parabolic curves in Figure (3.1).

Figure (3.2) presents an overview of the experimental setup. There are two experimental setups for the ODT. The first one is for investigating the novel loading scheme. The second one is for CODT studies. Plot (A) presents a sketch of the optical setup of the bichromatic MOTs and the HODT at 1064 nm. Plot (B) illustrates a sketch of the optical setups of the bichromatic MOTs and the VODT at 532 nm. Notice, the setup of the ODT for the study of the novel loading scheme is similar to the setup shown in Plot (A). The details of the setups are described in the following sections.

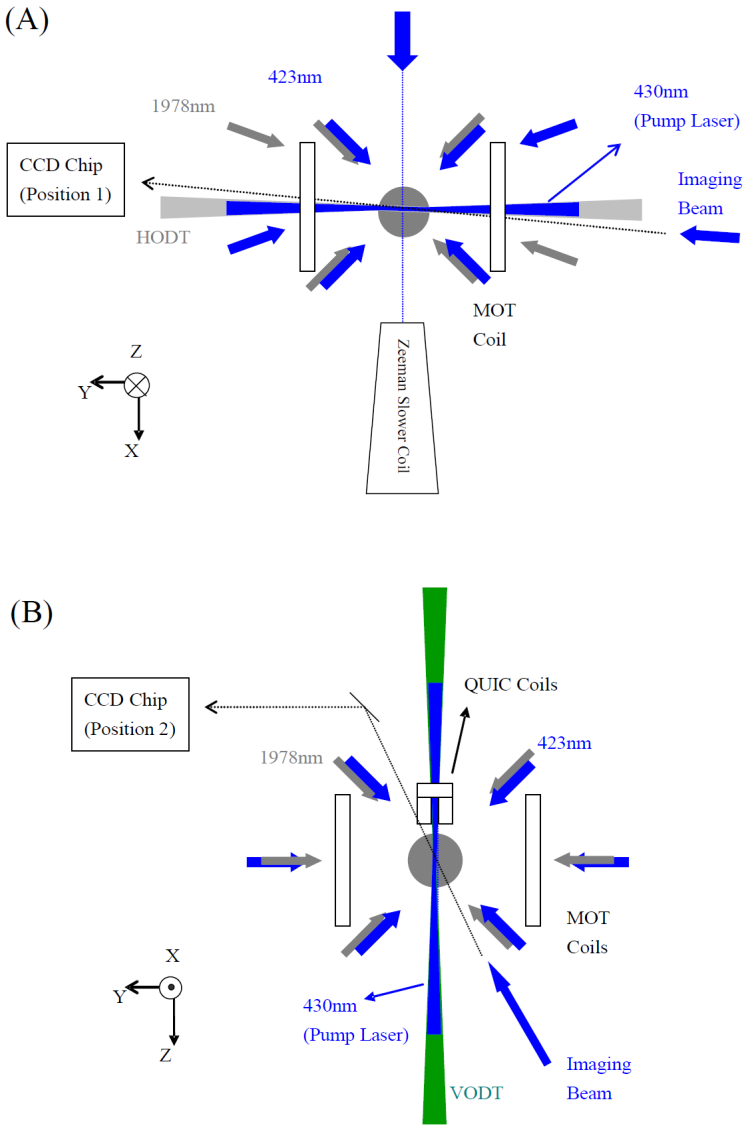

Figure 3.2: An overview of the experimental setup. Plot (A) shows the optical setup of the MOTs and the HODT. Plot (B) shows the setup of the MOTs and the VODT. Beams for the $^1S_0$ singlet-MOT and the $^3P_2$ triplet-MOT are shown by blue and gray arrows, respectively. Two shaped pump laser beams (blue beam-shaped lines) and ODTs at 532 nm (the green beam-shaped line) and at 1064 nm (the gray beam-shaped line) are well superimposed and located at the center of the $^3P_2$ triplet-MOT (the gray circle). Notice, the setup of the ODT at 532 nm for the study of the novel loading scheme is the same as that of the HODT shown in Plot (A). The z-direction corresponds to the axis of gravity. Further information is provided in the following sections.

3.2 423 nm Laser System

3.2.1 Setup of the 423 nm Laser System

The schematic setup of 423 nm laser system is illustrated in Figure (3.3). 423 nm radiation is generated by two lasers and a frequency doubling ring resonator. The commercial Verdi laser[1] at approximately 532 nm with 10 W laser output power is used to pump the homemade Ti:Sapphire laser [Zim95]. The Ti:Sapphire laser yields 2 W of output laser power at approximately 845 nm with two longitudinal modes due to a standing-wave designed laser resonator. The frequency doubling ring resonator with a LBO crystal doubles the frequency of the infrared beam and emits about 300 mW at approximately 423 nm.

The frequency doubling ring resonator is stabilized to a frequency approximately equal to that of 845 nm radiation by the Pound-Drever-Hall (PDH) technique [Dre83, Bla01]. The photo-diode detects the beat signal, between the carrier frequency and 40 MHz side-bands generated by the electro-optic modulator (EOM), from an infrared beam that is reflected by an in-coupling mirror in the frequency doubling ring resonator. After this, the mixer generates an error signal which depends on the phase difference between the beat signal and the modulation frequency from the voltage controlled oscillator (VCO). The integrated error signal generated by an integrator is fed to the piezo-ceramic tube glued to a mirror of the frequency doubling ring resonator to adjust the length of the resonator.

The frequency of 423 nm radiation is stabilized to the atomic transition by polarization spectroscopy [Wie76]. There are two blue spots leaving the back side of the LBO crystal in the frequency doubling ring resonator due to the fact that there is no AR-coating on it. Their polarizations are perpendicular to the infrared light because of a Brewster cutting of the edges. One of the beams is used as the pump beam after its polarization is changed to circular by a quarter wave-plate (QWP). The second beam is used as the probe beam which is passed through the acousto-optic modulator[2] (AOM) for frequency shifts. Further frequency shifts are carried out by a magnetic field which is provided by a pair of Helmholtz coils located near the homemade glass cell[3]. The pump and the probe beams counter-propagate through the glass cell which contains a calcium oven. After passing through the cell, the probe beam is split in two by a polarizing beam-splitter cube (PBC). The beams are detected by two photo-diodes. The induced birefringence in the calcium

[1] Coherent Inc., Verdi V10
[2] IntraAction, ADM-40
[3] glass cells and discharge cells are made by Mr. Dieter Barloesius in ILP

vapor is given by the difference between the signals of the two photo-diodes. Afterwards, the integrated error signal is fed back to the intra-cavity piezo in the resonator of the Ti:Sapphire laser. The frequency of the blue light is set to maximize the atom number in the $^1S_0$ singlet-MOT by adjusting the electronic offset of the error signal.

The experiment is set up on two optical tables. After generation, the blue beam is transferred to the second optical table where the vacuum system is located, and its path between the tables is controlled by the beam transfer system[4]. The blue beam is then separated into two beams. The first one is used for the $^1S_0$ singlet-MOT. The second one propagates through the AOM[5]. The frequency of the beam is shifted by 274 MHz which is used for the Zeeman slower beam and the absorption imaging system. The QWP before the entrance of the Zeeman slower beam converts the polarization state to circular.

The imaging beam is passed through another AOM[6] to tune the frequency back to resonance. The frequency is tuned by 315 MHz which is 41 MHz above the atomic transition and set to obtain a maximal absorption imaging signal of the atoms in the MOT. A pinhole after the AOM is used to block higher order modes of the beam. The imaging beam is intensity stabilized by the side-of-fringe technique, that is used to lock the optical cavity to TEM_{00} modes given by a transmission spectrum. The magnetic base after the AOM is used as a switch to change the beam paths. The first imaging beam path is titled 4° with respect to the horizontal plane (the X-Y plane in Figure (3.2). The beam is collimated and then focused by a 200 mm achromatic focusing lens. The CCD chip[7] behind the vacuum system is mainly used for detecting the characteristics of atoms in the MOTs. One pixel corresponds to 4.4 μm. The second beam path is titled 45° with respect to the horizontal plane. The collimated imaging beam is focused by a 250 mm achromatic lens and a CCD chip detects the characteristics of atoms trapped in the dimple. One pixel is equal to 3.2 μm.

Experimental time sequences are controlled by the ADwin system with a LabView front panel. Switching of beams is controlled by a mechanical shutter and an AOM depending on the required switching time. Due to a 250 μs switching time of a mechanical shutter, an AOM is applied as a fast switch and is set after a mechanical shutter in order to block residual light.

[4]The system was developed by C. Zafiu

[5]Crystal Technology 3250-190

[6]IntraAction, ATM-2701A1

[7]PixelFly scientific, PCO computer optics GmbH, resolution 1280x1024 pixels, CCD sensor diagonal 11 mm

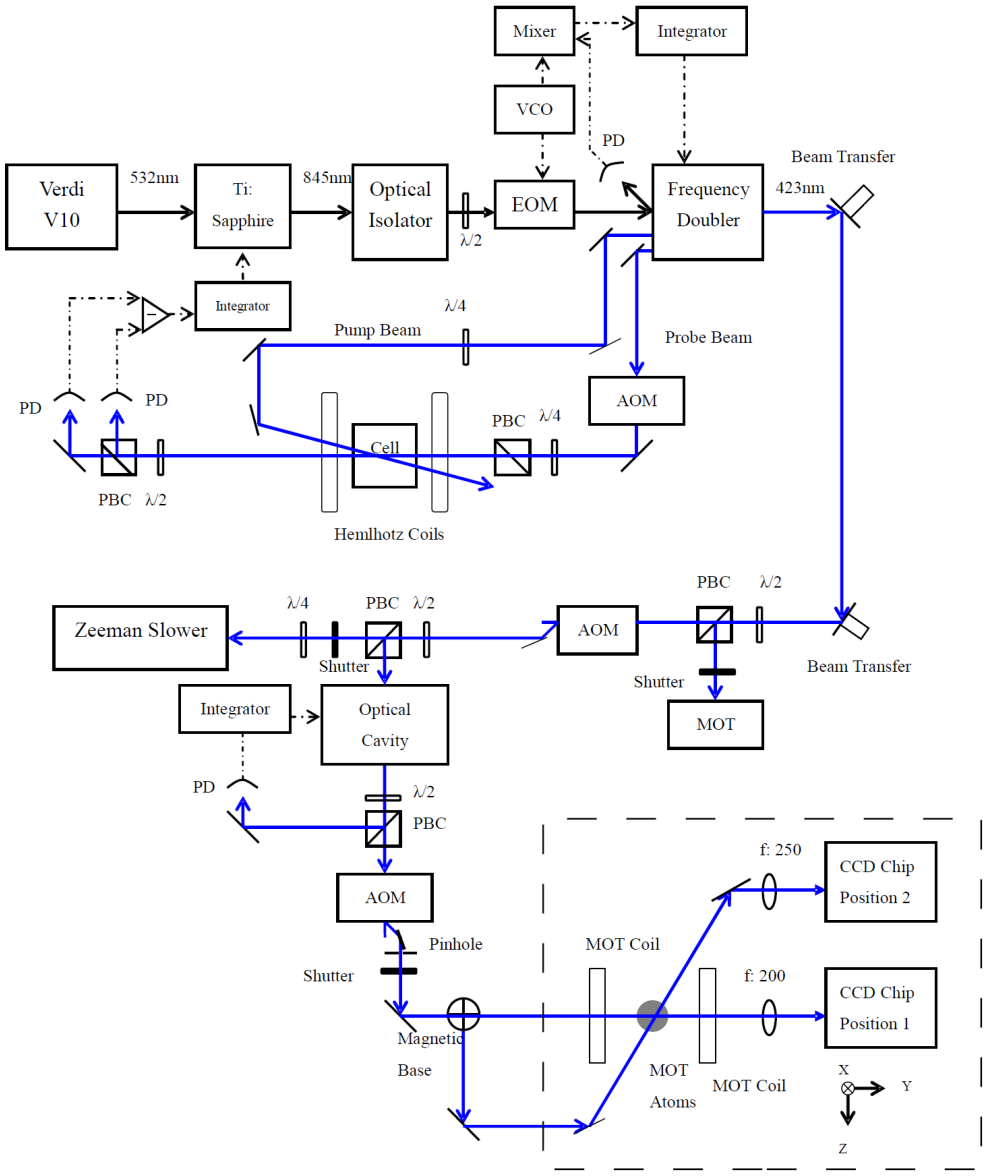

Figure 3.3: Schematic setup of the 423 nm laser system. Blue lines represent 423 nm radiation. $\lambda/2$: half-wave plate (HWP). $\lambda/4$: QWP. PD: photo-diode. The coordinate system is only valid for the area enclosed by the dashed line, where the z-axis corresponds to the axis of gravity. Besides the focusing lenses for the imaging system, lenses used in the system are not shown in the figure. The unit of the focal length f is given in mm. Further details are given in the text.

3.2.2 Modifications and Discussion

Several modifications have been made to the 423 nm laser system. Firstly, the Ti:Sapphire laser has a new design utilizing an out-coupler étalon. Two mirrors of the out-coupler étalon are glued onto two separate aluminum bases where one mirror is glued to a piezo-ceramic tube. The new design of the laser has benefits for adjusting the length of the resonator and for cleaning the resonator. The old-design of the Ti:Sapphire laser is described in the Ph.D. thesis of Jan Grünert [Gru02a]. The details of the new design and characteristics of the Ti:Sapphire laser will most likely be described in the work of Purbasha Halder.

Secondly, the optical isolator[8] is positioned after the Ti:Sapphire laser's output to prevent the beam feeding back from the frequency doubling ring resonator.

Thirdly, the finesse of the optical cavity in the imaging beam path has been increased from 14 to 30. The previous optical cavity often became dirty resulting in two adjacent transmission peaks which cannot be distinguished. An optical cavity with a higher finesse generates sharper transmission peaks which improves the intensity-locking process.

Besides the modifications above, improvement of performance of the Ti:Sapphire laser and exchange the LBO crystal base in the frequency doubling ring resonator are necessary. A stability of the $^1S_0$ singlet-MOT is essential for operating the $^3P_2$ triplet-MOT and for the loading process of the ODTs. During experiments, the unstable performance of the Ti:Sapphire laser and the unstable LBO crystal base in the frequency doubling resonator often cause serious power fluctuations of the blue light. Therefore, the experimental system has to be readjusted accordingly. Thus, these improvements are necessary.

3.3 1978 nm Laser System

3.3.1 Setup of the 1978 nm Laser System

The schematic setup of the 1978 nm laser system is presented in Figure (3.4). The 1978 nm laser source is generated by three lasers. The commercial Verdi laser[9] at approximately 532 nm with 5.5 W of laser output power is used to pump the homemade Ti:Sapphire laser. The Ti:Sapphire laser emits 1.3 W of infrared radiation at approximately 786 nm which is used to pump the home-

[8] Polytec, M713A, Optical Isolator
[9] Coherent Inc.,Verdi V5

made Tm:YAG laser. The Tm:YAG laser emits 140 mW at approximately 1978 nm. The details of the laser system are described in the work of Jan Grünert [Gru02a].

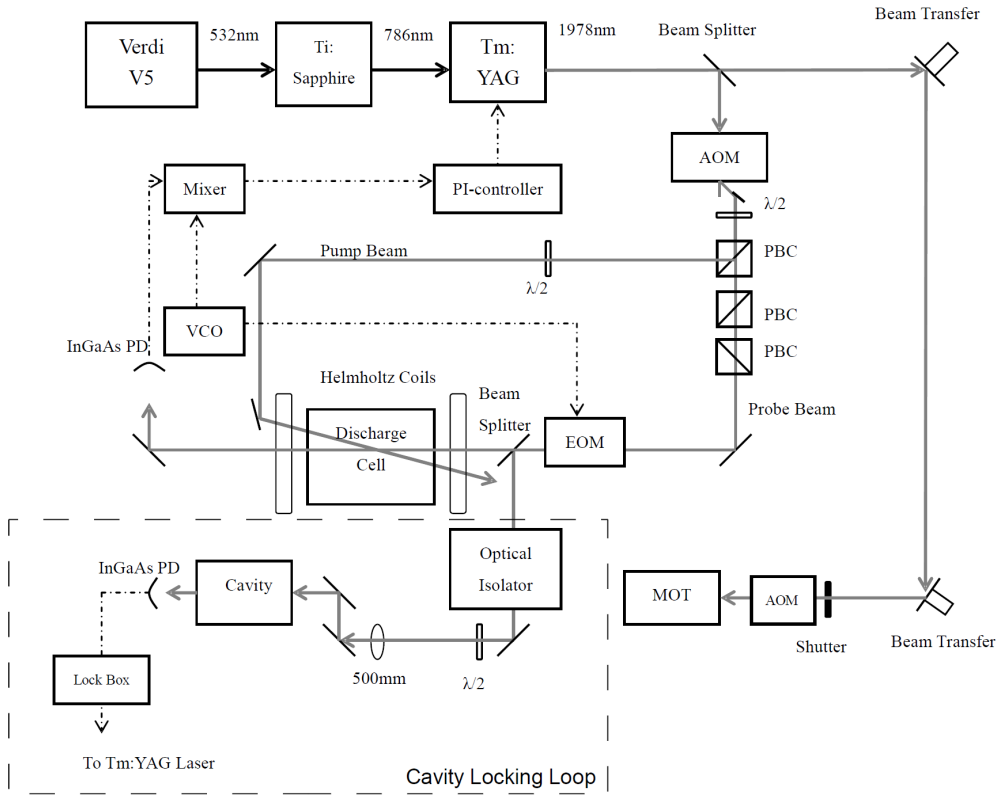

Figure 3.4: Schematic setup of the 1978 nm laser system. Gray lines represent 1978 nm radiation. The area enclosed by the dashed line shows the setup of the cavity locking loop. The abbreviations of the optical elements are given in Section (3.2.1). Besides the lens for cavity mode-matching, lenses used in the system are not shown in the figure. The details are described in the text.

The frequency of the Tm:YAG laser is stabilized by the PDH technique. The beam splitter splits the beam in two. One of the beams, with approximately 20 % of the beam power, passes through the AOM[10] for the polarization spectroscopy. The beam after the AOM is split into the pump beam and the probe beam. The ratio of intensities between these two beams is adjusted by the HWP and the PBC behind the AOM. The probe beam is modulated

[10]IntraAction, ACD 402A A3

by the EOM which generates sidebands at 36 MHz. The pump beam and the probe beam counter-propagate though the discharge cell which provides metastable calcium atoms. The function of the discharge cell is described in Section (3.6). The pair of Helmholtz coils near the cell provides a magnetic field for frequency shifts. The fast InGaAs photo-diode[11] detects the absorption signal from the probe beam [Han05]. The mixer de-modulates the signal and the PI-controller generates an error signal which feedbacks to the piezo-ceramic tube in the Tm:YAG laser resonator, which is used to adjust the length of the resonator. The frequency of the beam is set to maximize the number of atoms loaded in the $^3P_2$ triplet-MOT by adjusting the electronic offset of the error signal.

The other beam after the beam splitter is transferred to the second optical table for the $^3P_2$ triplet-MOT. The beam path between the two optical tables is controlled by the beam transfer system. The infrared beam passes through the AOM, which is used as a fast switch. Experimental time sequences are controlled by the ADwin system with a LabView front panel.

The area enclosed by the dashed line in Figure (3.4) shows the setup of the cavity locking loop which is used to stabilize the frequency of the infrared beam in the 100 kHz range. The purpose is to reduce the temperature of the atoms trapped in the $^3P_2$ triplet-MOT. This locking loop is not used at the same time as the frequency stabilization loop of the Tm:YAG laser described in the previous paragraph.

Part of the probe beam in the spectroscopy setup is picked off for the locking loop. The beam passes through the isolator[12] which is used to suppress reflected beams from the spectroscopy setup. The size of the beam is modified by a 500 mm achromatic lens in order to mode-match to the cavity. The cavity is set up vertically and is located in the vacuum chamber in order to eliminate noise. The cavity consists of two plane-concave mirrors, one piezo-ceramic tube and a spacer. The two mirrors have a radius of curvature of 2000 mm and a reflectivity of 99.7%. Such a high reflectivity is required in order to reach the required finesse of the cavity. The length and the material of the spacer and the piezo-ceramic tube have been chosen to achieve the required free-spectral-range and stability of the cavity. Temperature stabilization is applied for elimiating thermal fluctuations. The frequency of the Tm:YAG laser is stabilized by using the side-of-fringe technique. The fast InGaAs photo-diode detects the transmitted photons passing through the cavity. Taking the polarization spectroscopy signal as a reference, the frequency of the peak of a transmission signal will be shifted to the atomic

[11] Hamamatsu, G8422-03
[12] Doehrer electrooptik GmbH, I-21-B4-H

resonance. This is carried out by applying a DC voltage to the piezo-ceramic tube which is glued to one cavity mirror for cavity length adjustment. The signal is amplified and subsequently sent to an integrator. The error signal is fed back to the piezo-ceramic tube in the Tm:YAG laser resonator for the length adjustment.

3.4 430 nm Laser System

3.4.1 Setup of the 430 nm Laser System

430 nm laser radiation is generated by a diode laser and a frequency doubling resonator. The schematic setup of the system is shown in Figure (3.5). The diode laser emits infrared radiation at approximately 860 nm with about 27 mW of output power. After passing through the optical isolator[13] and the anamorphic prism pair (A.P.), the beam is sent to the frequency doubling resonator with a $KNbO_3$ crystal. The frequency doubling resonator emits blue light at 430 nm with about 3 mW of laser power.

The frequency of the frequency doubling resonator is stabilized by the PDH technique. The technique is similar to the setup in the 423 nm laser system. Since the sidebands of the beam can be generated by modulating the current of the diode laser, an EOM is not necessary here.

The frequency of the diode laser is stabilized by polarization spectroscopy which is similar to the technique used in the 423 nm laser system. After the frequency doubling resonator, the beam is split into two parts by a PBC. One of the beams, of approximately 1 mW power, is used for the spectroscopy setup. The beam passes though the AOM[14] which is needed to compensate the frequency shift of the AOM on the other optical table. The HWP and the PBC after the AOM are used for adjusting the intensities of the circularly polarized pump beam and the linearly polarized probe beam. The pump beam and the probe beam counter-propagate through the discharge cell. The pair of Helmholtz coils near the cell provide a magnetic field for further frequency shifts. After passing through the cell, the probe beam is split in two by a wollaston prism. The beams are detected by two photo-diodes. The difference signal between the two photo-diodes is sent to the lock box. The integrated error signal is fed back to the current controller of the laser diode for the frequency adjustment. The frequency of the beam can be shifted by adjusting the electronic offset of the error signal.

[13] Faraday isolator, 60dB
[14] Crystal Technology, 3080-120

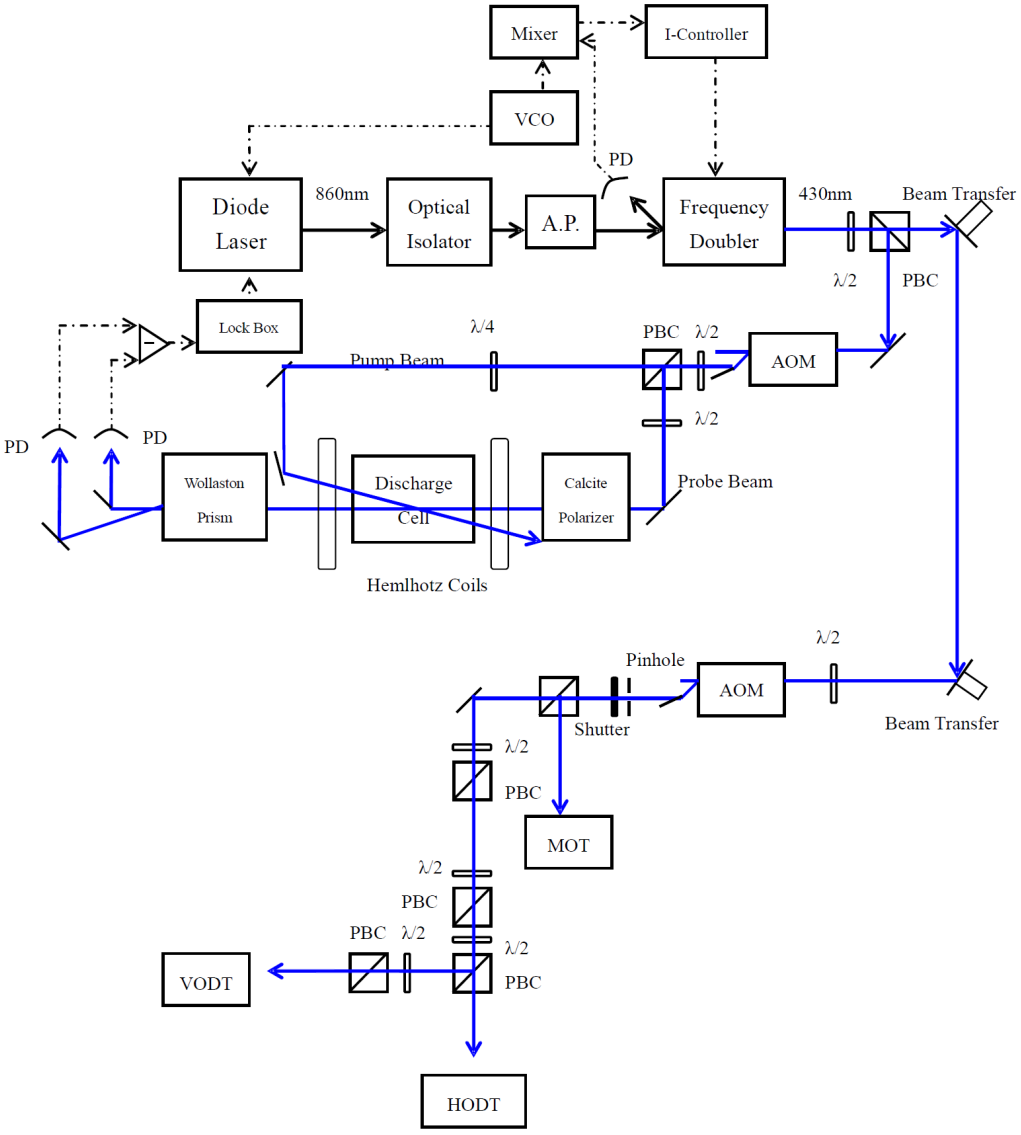

Figure 3.5: Schematic setup of the 430 nm system. Blue lines represent 430 nm radiation. The abbreviations of the optical elements are given in Section (3.2.1). Lenses used in the system are not shown in the figure. Further details are described in the text.

Another beam is transferred to the second optical table. The beam path between the two optical tables is controlled by the beam transfer system. The AOM in the beam path works as a fast switch and, moreover, is used for fine

adjustment of the intensity of the pump beams for the atoms loading into the ODTs. This is carried out by adjusting the amplitude of the RF frequency of the AOM. After the AOM, the first diffracted beam is separated into two parts by a PBC. With use of the HWP in front of the AOM, the intensities of the two beams can be adjusted. One of the beams is used for pumping the atoms trapped in the $^3P_2$ triplet-MOT to the $^1S_0$ state for detecting the number and temperature of the atoms by the absorption imaging method. The other beam is split in two used for loading atoms into the ODTs. Here, several pairs of HWPs and PBCs are used to attenuate the intensities of the beams used to load atoms into the ODTs.

Experimental time sequences are controlled by the ADwin system with a LabView front panel.

3.5 ODT Systems

3.5.1 ODT System for Studies of Continuous Loading

A sketch of the optical setup of the ODT for the novel loading scheme is shown in Figure (3.6). Linearly polarized radiation at 532 nm is used for the ODT. The beam is provided by the commercial Verdi laser[15] with an output laser power of 5 W.

The geometric size of the 532 nm beam is scaled by the telescope, a 100 mm and a 75 mm achromatic focusing lens, in order to achieve a sufficient diffraction efficiency of the AOM[16]. To obtain the ideal required beam size of the ODT, the size of the first order diffracted beam is modified by the telescope setup, consisting of a 50 mm and a 500 mm achromatic focusing lens, and focused by a 500 mm focusing lens before it propagates into the vacuum system. The resulting beam waist of 532 nm radiation is 22.5 μm in radius. The 500 mm focusing lens before the vacuum system is set on a base which can be translated in μm steps in three dimensions for fine position adjustment of the beam focus. Considering the power loss from the vacuum viewport and the diffraction efficiency of the AOM, the 532 nm radiation generates a 350 μK optical potential for the $^1S_0$ state with 3 W laser power in the vacuum system. The power of the ODT laser beam is controlled by the AOM by adjusting the amplitude of the RF frequency.

Linearly polarized radiation at 430 nm is generated by the laser system described in Section (3.4.1). The size of the first order diffracted beam after

[15] Coherent Inc., Verdi V5
[16] IntrAction, ACD 402AA3

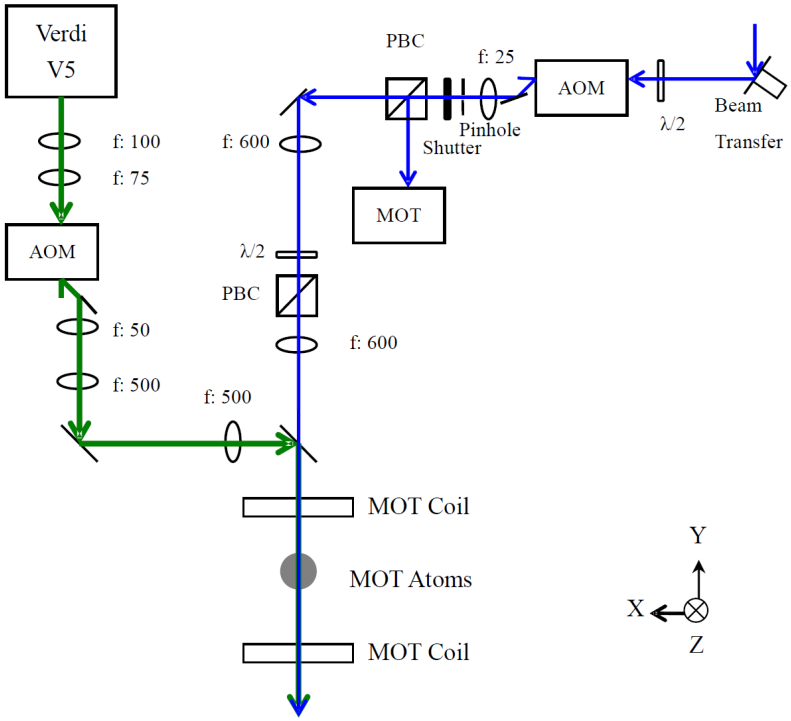

Figure 3.6: Sketch of the 532 nm ODT system. Green and blue lines represent 532 nm radiation and 430 nm radiation. The foci of 532 nm radiation and 430 nm radiation are well superimposed at the center of the $^3P_2$ triplet-MOT. The z-direction corresponds to the axis of the gravity. The unit of the focal length f is given in mm. The abbreviations of the optical elements are given in Section (3.2.1). The details of the setup are described in the text.

the AOM[17] is scaled by the telescope setup, a 25 mm achromatic focusing lens before a pinhole and a 600 mm achromatic focusing lens. After being scaled, the beam is focused by a 600 mm achromatic focusing lens before being sent to the vacuum system. This 600 mm focusing lens is set on the base which can be translated in μm steps for fine position adjustment of the beam focus. The resulting beam waist of blue radiation is 17 μm in radius. The intensity of the blue beam is mainly attenuated by two pairs of PBCs and HWPs. The fine intensity of the blue beam is controlled by adjusting the amplitude of the RF frequency of the AOM.

The foci of 532 nm radiation and 430 nm radiation are carefully super-

[17]Crystal Technology, 3080-120

imposed in the center of the $^3P_2$ triplet-MOT. Both beams are located in the horizontal plane (the X-Y plane marked in Figure (3.6)). AOMs in the system are not only used for intensity adjustment but are also applied as fast switches. The timing steps of AOMs are controlled by the ADwin system with a LabView front panel.

3.5.2 ODT System for Studies of the CODT

The CODT setup is shown in two separate figures. Figure (3.7) shows the optical setup of the HODT at 1064 nm as well as 430 nm radiation. Figure (3.8) presents the optical setup of the VODT at 532 nm as well as 430 nm radiation.

A fiber laser[18] at 1064 nm with 20 W of output power is used as the HODT, see Figure (3.7). The beam is sent to the AOM[19] after modification of the size. The AOM here is for controlling the intensity of the laser beam and as a fast switch. The first order diffracted beam is guided through the QWP to obtain a circularly polarized beam. The polarization of the beam is determined by the optical pumping process described in Section (5.1). The telescope setup, consisting of two achromatic focusing lenses of 50 mm and 750 mm focal length, and an additional 500 mm achromatic focusing lens are used to derive the optimal size of the HODT beam for the experiment. The 500 mm focusing lens is set on a base which can be translated in three different dimensions in μm steps for adjusting the position of the beam focus. Besides taking into account the diffraction efficiency of the AOM, two more factors cause losses of the beam power. Because of unavoidable beam distortions by the AOM, the first order diffracted beam after the AOM is elliptical and part of it is cut by the 45° reflection mirror before the vacuum system. Moreover, since the viewport of the vacuum system is AR-coated for 423 nm and 1978 nm, approximately 17 % of the power of the HODT beam is lost. The resulting depth of the HODT for the $^1S_0$ state is 372 μK which takes into account a power of 13.5 W and a beam waist radius of 31 μm. The beam waist of the HODT is determined from trap frequency measurements, see Section (5.2.1).

A commercial Verdi laser[20] at 532 nm is used for the VODT, see Figure (3.8). The linearly polarized beam is passed through the AOM[21] and the first order diffracted beam after the AOM propagates through the telescope setup consisting of a -40 mm lens and 400 mm focusing lens. Then, the beam

[18] IPG Photonic, Ytterbium Fiber laser, YLR-20-1064-LP-SF, 20W
[19] PEGASUS OPTIK GmBH, AA.MTS80-A3-10
[20] Coherent Inc.,Verdi V5
[21] IntraAction Corp., ADM-402A1

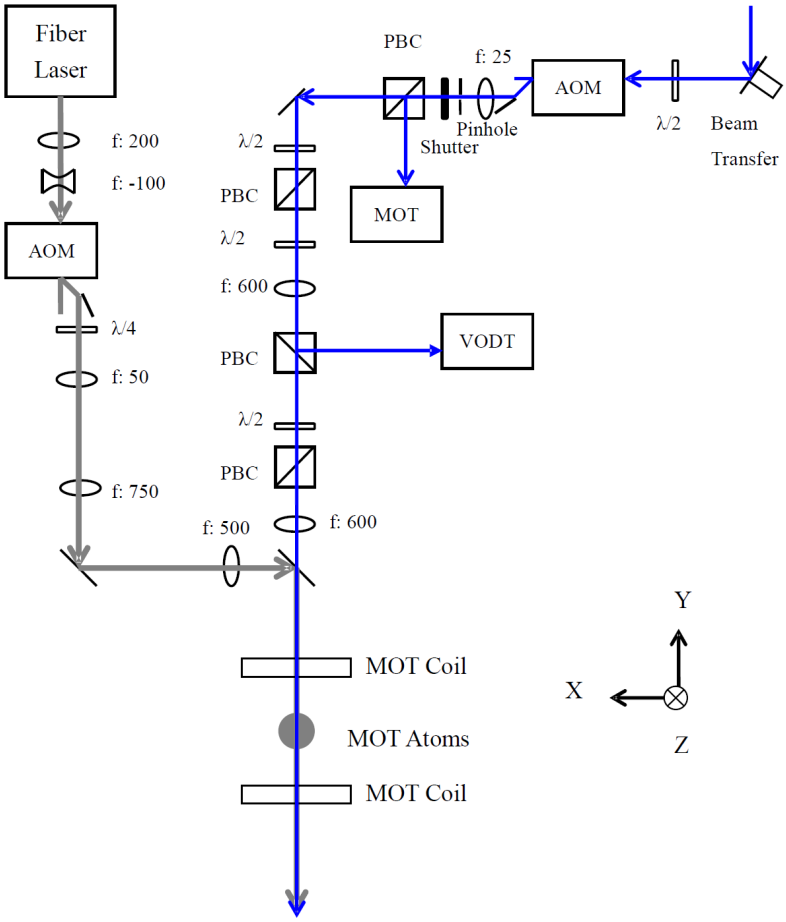

Figure 3.7: Schematic setup of the HODT at 1064 nm. Gray and blue beams represent radiation at 1064 nm and 430 nm, respectively. The foci of the HODT and 430 nm radiation are well superimposed at the center of the $^3P_2$ triplet-MOT. The z-direction corresponds to the direction of gravity. The unit of the focal length f is given in mm. The abbreviations of the optical elements are given in Section (3.2.1). A detailed description is given in the text.

is focused by the lens with a focal length of 500 mm before entering the vacuum chamber. The 500 mm focusing lens before the vacuum system is set on a base which may be translated in μm steps in three dimensions for fine position adjustment of the beam focus. The resulting beam waist is 15.8 μm which is determined by trap frequency measurements. The VODT generates a trap depth of 615 μK for the $^1S_0$ state with a power of 3.22 W in the vacuum

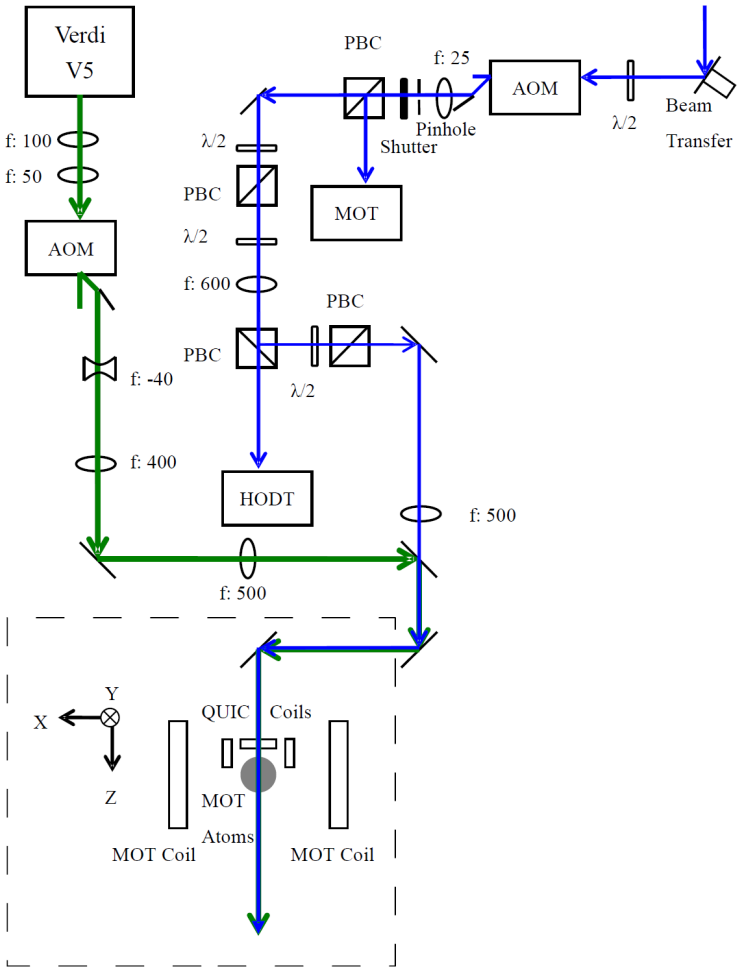

Figure 3.8: Schematic setup of the VODT at 532 nm. Green and blue beams represent 532 nm radiation and 430 nm radiation, respectively. The foci of the VODT and 430 nm radiation are well superimposed at the center of the $^3P_2$ triplet-MOT. The coordinate system is only valid for the area enclosed by the dashed line, where the z-axis corresponds to the axis of gravity. The unit of the focal length f is given in mm. The abbreviations of the optical elements are given in Section (3.2.1). Detailed explanations are given in the text.

chamber where the gravitational potential and the loss of 8 % of the beam power at an uncoated viewport are taken into account.

Blue radiation at 430 nm is generated by the laser system described in

Section (3.4.1) and the general idea of the setup is similar to the one described in Section (3.5.1). The beam size is adjusted by the telescope setup which consists of a 25 mm achromatic focusing lens immediately after the AOM[22] and a 600 mm focusing lens afterwards. The beam is separated into two branches. One of the beam branches is used for the HODT loading process. Before entering the vacuum system, the beam is focused by a 600 mm focusing lens. The resulting beam waist is 17 μm in radius, see Figure (3.7). The other beam is used for the VODT loading process. It is focused by a 500 mm focusing lens before being sent into the vacuum system. The resulting beam waist is 16 μm in radius, see Figure (3.8). The focusing lenses of the pump beams are positioned in front of the vacuum system, and are set on bases which can be translated in μm steps in three dimensions for fine position adjustment of the beam focus. The foci of blue and ODT laser beams are well superimposed in the center of the $^3P_2$ triplet-MOT. Pairs of PBCs and HWPs are used not only for attenuating the power level of the blue beams, but also for setting the power ratio of the two beam branches. After the power ratio of the two pump beams is adjusted, the fine adjustment of the two beam powers can be adjusted simultaneously which is provided by the AOM to obtain a maximum of atoms loaded into the ODTs. The timing procedures are controlled by the ADwin system with a LabView front panel.

The foci of the HODT and the VODT intersect in the center of the $^3P_2$ triplet-MOT. After the loading processes of the ODTs are finished, the alignment of the ODT beams is done by mounting the CCD camera in two different positions[23], see Figure (3.9). Using the highest optical density of the atoms as a reference point to locate the center of the ODT beam, the foci of the ODT beams can be aligned. Image (A) in Figure (3.9) is an image of the CODT taken by the CCD camera at position 1 and image (B) shows an image of the CODT taken by the CCD camera at position 2. The HODT and the VODT are marked in the images. The obtained maximum number of atoms trapped in the dimple indicates a good overlap of the foci of the ODTs. The two foci of the CODT beams can be aligned with an error smaller than the Rayleigh ranges of the two ODT beams.

[22] Crystal Technology, 3080-120

[23] See Section(3.2)

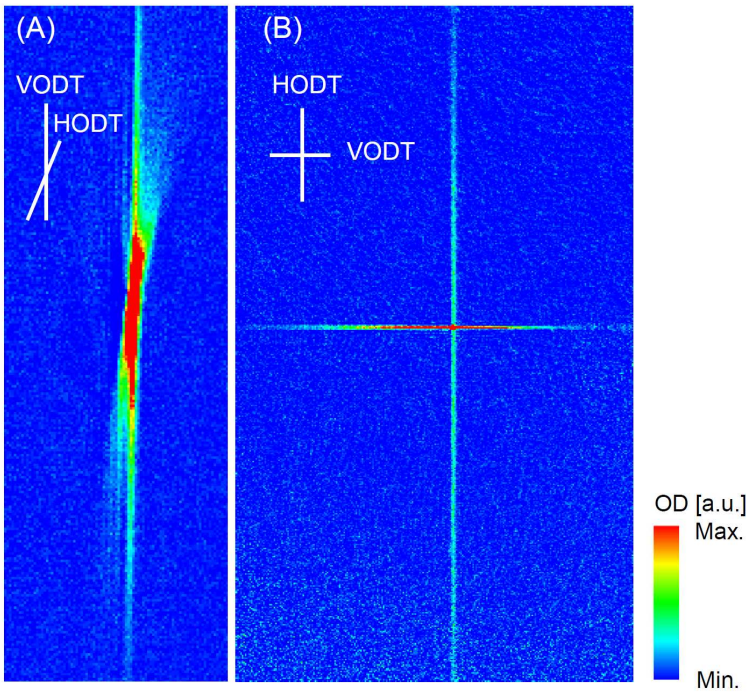

Figure 3.9: Images of the $^1S_0$ CODT. The image (A) is taken by the CCD chip located at position 1. The image (B) is taken by the CCD chip located at position 2. The positions of the CCD chip are shown in Figure (3.2). The beam waist radius of the HODT and the VODT are 31 μm and 15.8 μm, respectively.

3.6 Modifications to Discharge Cells

To provide the frequency reference, discharge cells are used to produce the necessary metastable calcium atoms. Photos and a schematic of a discharge cell are shown in Figures (3.10) and (3.11), respectively. The discharge cell made following the old design had to be exchanged often. One reason is that the noble gases flow away from any leaks in a Pyrex cell. The other reason is that calcium atoms attached on the inner surface of the cell cause short circuits between electrodes and changes the behaviors of the discharge. To prevent the drawbacks of this discharge cell, some modifications have been made.

Our previous work describes details of the function of discharge cells [Han05]. The cell containing a calcium oven is evacuated by a turbopump to 10^{-8} mbar and subsequently filled by 2 torr of neon. Calcium vapor is heated out of the oven and calcium atoms are excited to the metastable state by collisions with discharged neon gas. The onset voltage of the discharge is 200 V and typically the operation discharge voltage is 1 kV. When the discharge voltage reaches the onset voltage without heating the calcium oven, an orange luminescence appears in the cell which is characteristic of neon gas. When the temperature of the oven reaches the operation state, purple fluorescence appears in the cell because photons are emitted from the strong principle transition line of ^{40}Ca atoms at 423 nm. The heating current for the oven is set to obtain an adequate amplitude of the spectral signal for the experiment. The sketch of a discharge cell with the old design is presented in Figure (3.10(B)) and a photo of this cell is displayed in Figure (3.10(A)).

The discharge cell has been modified in several ways. First of all, the configuration of the cell has been changed to eliminate leaks of the neon gas. As shown in Figure (3.10(C)), the electrodes used for discharging and heating are embedded in a Pyrex cell. Due to imperfect contact between the glass and the electrodes, neon gas often escapes in a few weeks. In order to suppress this process, a newly designed cell has been made consisting of a glass tube and a glass-to-metal Pyrex tube[24] with three electrical feed-throughs on a CF35 Flange[25] as shown in the photo in Figure (3.11(B)). Three electronic feed-throughs are connected to the calcium oven. One of the feedthroughs is used for the anode of the discharge and the other two are used for the heating electrodes. Besides reducing leakage, the flange design makes the processes of evacuation and filling with neon gas easier. The new design discharge cell can be operated for some months without significant losses of neon gas.

[24] Hositrad, ssp-1500 with CF35 Flange
[25] Hositrad, 17064-05-CF, Feed-through 3 Pins

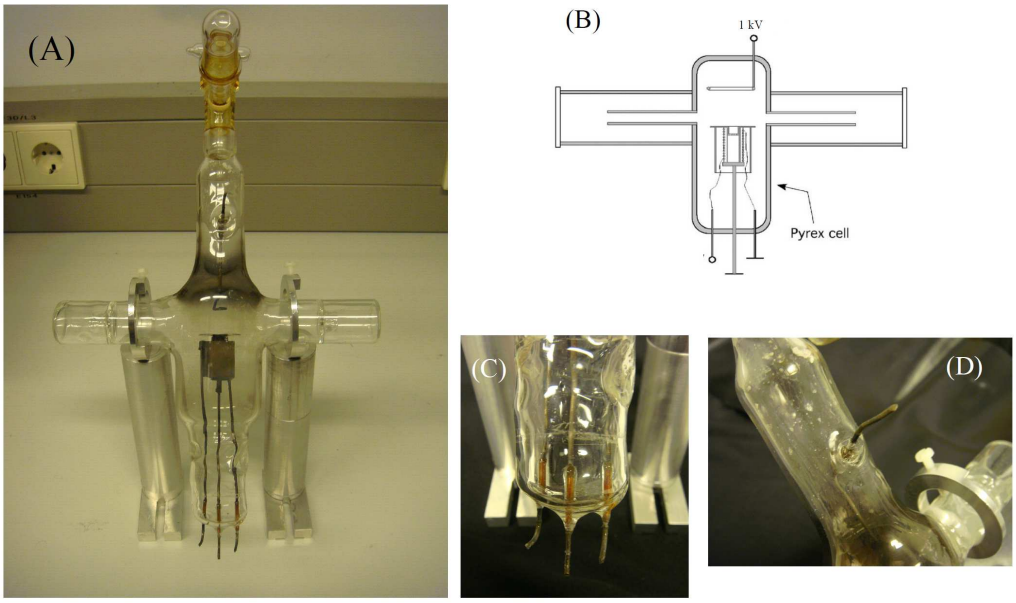

Figure 3.10: (A) A photo of the old-design discharge cell. (B) A schematic of the old-design discharge cell [Han05]. Horizontal tubes are attached in opposite directions slightly above the oven exit. They are sealed with transparent windows for laser beam transmission. A vertical tube is connected to the electrodes for the discharge and for heating the oven. The cylinder in the cell, an oven, is filled with calcium powder. The end cup of the oven is connected to ground and acts as the anode of the discharge cell. The two wires connected to the oven are the electrodes of heating. The ring above the oven acts as the cathode of the discharge. The details of the sketch are described in our previous work [Han05]. (C) Connections between electrodes and the Pyrex cell. (D) The connection between the cathode of the discharge and the cell.

Moreover, the configuration of the discharge cell has been changed to avoid short-circuits. Calcium vapor flows mainly in the vertical tube[26] of the cell and thus calcium attaches to the inner surface of the vertical tube after operation, as can be seen by the black calcium layers in Figures (3.10(A)) and (3.11(A)). The cathode of the discharge is easily covered by calcium layers which enable short circuits, see Figure (3.10(D)). In order to solve this problem, the location where the discharge cathode is connected to the Pyrex cell protrudes, as shown in the photo of Figure (3.11(C)). This new design

[26] [Han05]

reduces the amount of calcium atoms attached on the surface around the discharge cathode. Besides resulting in short circuits, calcium layers attached to the inner surface of the cell change the distribution and behavior of the discharge. Thus, the operating discharge voltage is often varied in order to obtain the best operational condition. The method to prevent calcium atoms from attaching to the surface is still an open question.

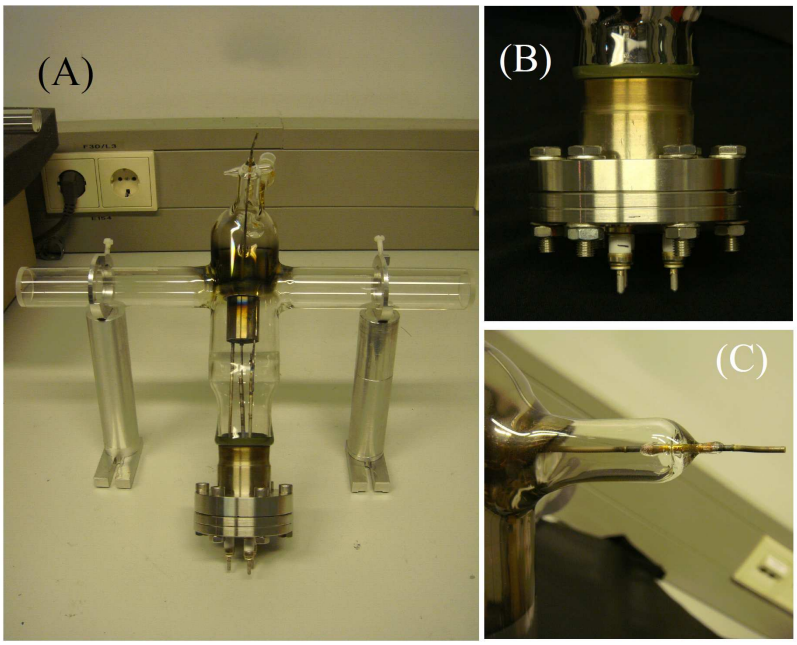

Figure 3.11: (A) A photo of the new-designed discharge cell. (B) The three feed-throughs for the three electrodes. (C) A newly designed connection for the discharge cathode.

Chapter 4

The Continuous Loading Scheme

Previous theoretical work [Kok03] investigated the collisional properties of metastable $^3P_2$ ^{40}Ca atoms in a magnetic field. It indicates that inelastic collisions are dominated by partial waves with large momenta, such as spin-exchanging collisions. The inelastic collision rate is predicted to be comparable with the elastic collision rate at relatively high temperatures, $T > 100\,\mu K$; however, at lower temperatures, $T \sim 1\,\mu K$, the inelastic collision rate is predicted to become substantially larger than the elastic collision rate. Thus, the largely inelastic rate appears to rule out the possibility of achieving a BEC with metastable ^{40}Ca atoms using magnetic traps.

Our previous work [Han06b] has clearly confirmed this prediction by measuring the collisional properties of ^{40}Ca atoms in the metastable $^3P_2$ state in a miniaturized Ioffe trap. By analyses of the loss of the atoms and the re-equilibration measurement, the inelastic collision rate and the elastic collision rate were measured, respectively. The results show that inelastic collision rates are comparable to or even one order of magnitude larger than the theoretical value. Our results are obtained in magnetic fields varying between 2 and 10 Gauss which are smaller than the applied magnetic fields (of the order of 100 Gauss) in the theoretical work. Therefore, the results indicate that, particularly at low magnetic field besides values due to the long-range mechanism described in the theoretical work [Kok03], other contributions need to be accounted for. One potential role of inelastic collisions is fine-structure changing collisions due to short-range interactions between colliding atoms. Such unusually large inelastic collision rates of ^{40}Ca atoms in the $^3P_2$ state exclude the implementation of evaporation in a magnetic trap. The essential condition for evaporation is that the time for re-thermalization has to be shorter than the lifetime of the atoms. The time for re-thermalization

is given by the elastic collision rate. The lifetime of the atoms is typically dominated by inelastic collisions.

In order to eliminate inelastic collisions, an ODT is used because it is able to trap all Zeeman substates and thus only fine-structure changing collisions remain. A linearly polarized laser beam at 532 nm is used for the ODT, which provides a trap depth of approximately 300 μK for the $^3P_2$ ($m = \pm 2$) states. The atoms loaded into the ODT are prepared by the $^3P_2$ triplet-MOT. In the experiments, unusually short trap lifetimes and low densities of atoms are observed, even for vanishing magnetic field strength. Low densities of the atoms in the ODT result from the density limited $^3P_2$ triplet-MOT due to the radiation trapping effect[1], density dependent losses and light assisted collisions. The short trap lifetimes (≈ 20 ms) indicate large inelastic collisions of metastable ^{40}Ca atoms. Recent experiments demonstrate that fine-structure changing collisions [Yam08] and principal-quantum-number changing collisions [Tra09], dominated by partial waves with small momenta, cause significant losses of metastable AEAs in ODTs. Accordingly, a metastable AEA BEC is unlikely to achieve.

Hence, in order to achieve a BEC, ^{40}Ca atoms are loaded into an ODT in the $^1S_0$ ground state. The $^1S_0$ ground state of ^{40}Ca atoms is the absolute ground state; therefore, two-body inelastic collisions cannot arise. Since the polarization gradient cooling technique is not available in the $^1S_0$ state and the intercombination transition is not applicable to our system, the resulting temperature of the atoms in the $^1S_0$ singlet-MOT is in the range of a few mK. This temperature is much higher than the depth of the $^1S_0$ ODT (350 μK). Therefore, the atoms in the $^3P_2$ triplet-MOT are chosen to be the reservoir for the $^1S_0$ ODT. To effectively load $^3P_2$ atoms in the density limited reservoir into the ODT, a novel loading scheme is needed.

Investigations of the new loading scheme are presented in this chapter. Besides experimental observations, two numerical models are developed for quantitative studies of the loading scheme. Some results of the novel loading scheme presented in this chapter have been published on Phys. Rev. A. 76, 033418 (2007) [Yan07].

4.1 Preparation of the Atoms in the $^1S_0$ ODT

The novel loading scheme is based upon a spatial energy selective optical pumping transfer. Only the $^3P_2$ atoms within the volume of the $^3P_2$ ODT are pumped and subsequently loaded into the $^1S_0$ ODT. The intensity of the optical pumping beam is kept so small that the transfer is only efficient

[1] see Section (2.1.4)

for slow atoms spending sufficient time in the pumping volume. Thus, the transfer provides significant energy selectivity.

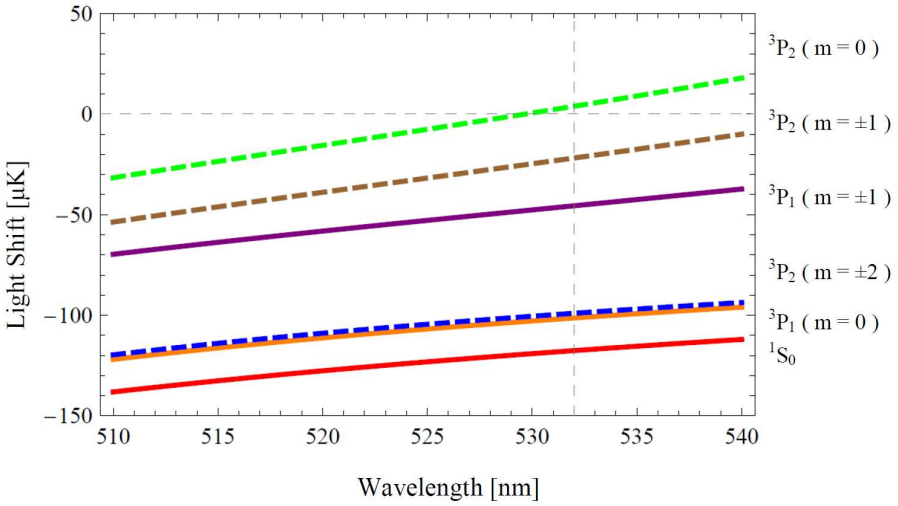

Figure 4.1: Light shifts of the relevant energy levels in ^{40}Ca atoms are shown as a function of wavelength for the dipole trap parameters used in this work at a power of 1 W. The graph shows the light shifts in μK. The orange line, the purple line and the red line represent the light shift of the $^3P_1$ (m = 0), the $^3P_1$ (m = ±1) metastable sublevels and the $^1S_0$ ground state, respectively. The green dashed line, the brown dashed line and the blue dashed line are negative light shifts of the m = 0, m = ±1 and m = ±2 states of $^3P_2$ metastable sublevels, respectively.

A linearly polarized Verdi laser at 532 nm with a 3 W maximum laser power and a 22.5 μm Gaussian beam radius is applied as the ODT laser beam. It provides negative light shifts in the ^3P_J metastable substates and the $^1S_0$ ground state, except for the $^3P_2$ (m = 0) state. Optical potentials in different quantum state can be calculated by Equations (2.13) and (2.14) with the spectral database found in [AD]. The curves in Figure (4.1) show the light shifts for the dipole trap parameters at a power of 1 W. Taking the light shift of the $^3P_2$ (m = ±2) metastable substates for example, the significant couplings of the $^3P_2$ states to higher lying states arise at 612 nm, 445 nm, and 430 nm. The coupling at 612 nm is due to a J = 1 level which has no effect on the $^3P_2$ (m = ±2) substates due to the π-polarization of the ODT laser. The negative light shift of the $^3P_2$ (m = ±2) substates are calculated by summing up the 45 most strongly coupled transitions. For the ODT at 532 nm, the deepest trap depth arises for the $^1S_0$ ground state.

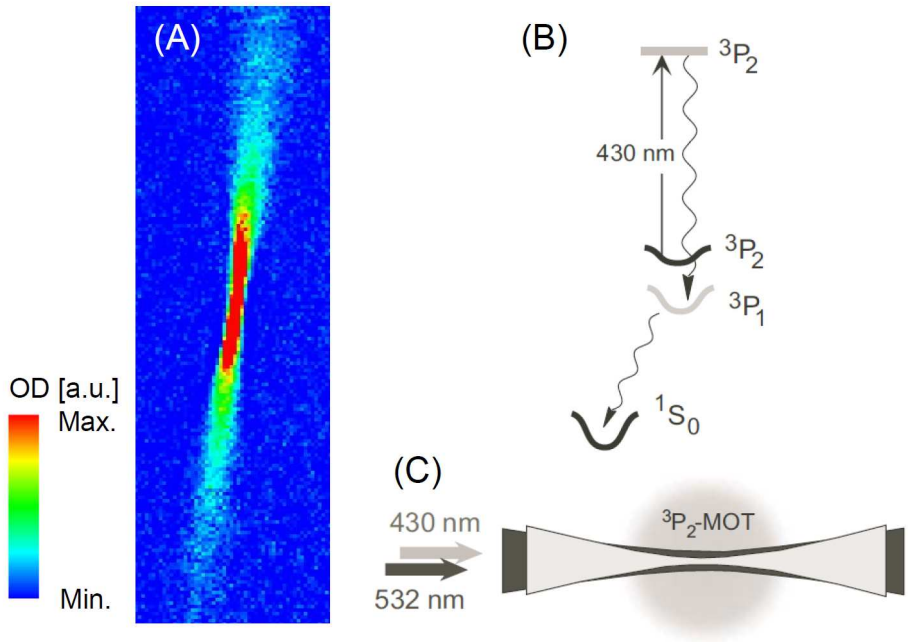

Figure 4.2: (A) Absorption image of the $^1S_0$ ODT. (B) Energy levels relevant for loading of the $^1S_0$ ODT. (C) Geometry of the ODT and optical pumping beam (not to scale).

The atoms loaded into the ODT are prepared by a moderately cold ($\approx 300\,\mu$K) and dense ($\approx 9 \times 10^9\,\mathrm{cm}^{-3}$) reservoir of $^3P_2$ atoms in the $^3P_2$ triplet-MOT. The loading process is carried out by the linearly polarized laser at 430 nm, the so-called pump laser, which addresses the transition from $^3P_2$ [4s4p] to $^3P_2$ [4p4p]. The pump laser, which has an intensity lower than the saturation intensity, is shaped to match the profile of the ODT. The foci of the pump laser beam and the ODT beam are well superimposed at the center of the reservoir. Therefore, the pump laser only pumps $^3P_2$ atoms inside the volume of the $^3P_2$ ODT to the $^3P_2$ [4p4p] state and the atoms decay to the $^1S_0$ ODT via the $^3P_1$ ODT within 0.42 ms. A continuous stream of cold atoms is transferred to the $^1S_0$ ODT since the volume of the $^3P_2$ ODT refills with $^3P_2$ atoms from the $^3P_2$ triplet-MOT before the $^3P_2$ population of the $^3P_2$ triplet-MOT is exhausted. Figure (4.2(B)) shows the energy levels relevant for loading of the $^1S_0$ ODT and figure (4.2(C)) illustrates the geometry of the ODT and optical pumping beam.

The experimental procedure of loading atoms into the $^1S_0$ ODT is illus-

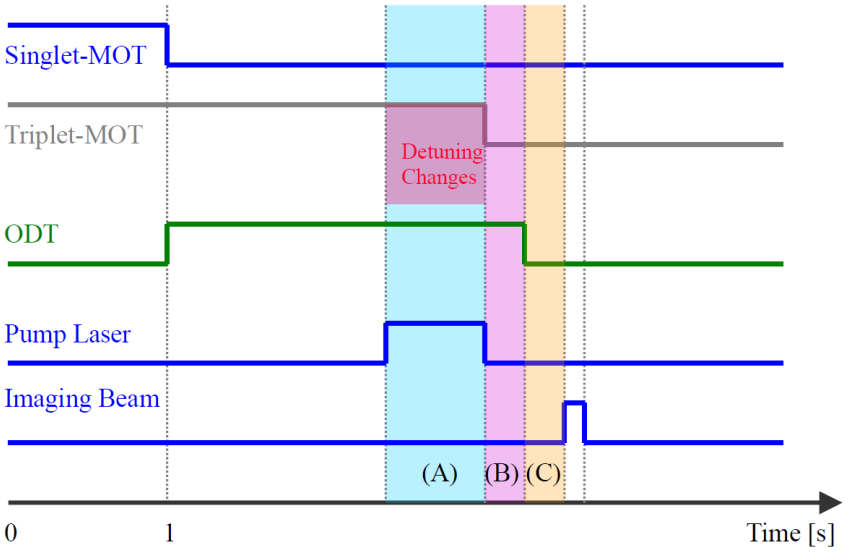

Figure 4.3: Timing diagram for loading atoms into the $^1S_0$ ODT. The traces show the steps of the experimental procedure. After loading atoms into the $^3P_2$ triplet-MOT for 1 s, the $^1S_0$ singlet-MOT is extinguished and the ODT laser is applied. During the loading phase, the pump laser is applied and the negative light shift of the $^3P_2$ triplet-MOT beams is increased which is shown by the red block. The blue block (A) denotes the time slot for atoms loading into the ODT, used in studies of the loading dynamics. The purple block (B) denotes the time slot for the holding of atoms in the trap, for example used in trap decay measurements. The orange block (C) denotes the variable time slot for expansion of the atoms in TOF measurements. The details are provided in the text.

trated in Figure (4.3). The experimental setup is described in Section (3.5.1). The preparation of the MOTs is described in Section (3.1). After loading the $^3P_2$ triplet-MOT for 1 s by the $^1S_0$ singlet-MOT, the $^1S_0$ singlet-MOT is extinguished and the ODT beam is applied. The pump laser beam with a 17 μm Gaussian radius is turned on to load atoms resonately into the $^1S_0$ ODT. The pump laser is shaped to match the profile of the ODT. The foci of the ODT beam and the pump laser are well superimposed at the center of the $^3P_2$ triplet-MOT. During the loading phase (the blue block (A) in Figure (4.3)), the negative detuning of the $^3P_2$ triplet-MOT beam (the red block in Figure (4.3)) is increased to compensate for the light shift of the $^3P_2$ triplet-MOT transition within the volume of the ODT. This increase of

the light shift of the $^3P_2$ triplet-MOT transition is caused by the ODT laser beam. Thus, Doppler cooling is still functional in the region of the ODT. Therefore, the temperature of the atoms trapped in the $^3P_2$ triplet-MOT increases to 300 μK. After the loading is terminated and subsequently the trap is switched off, the absorption imaging beam is applied to detect the number and temperature of the atoms. Figure (4.2(A)) shows an absorption image of the $^1S_0$ ODT.

4.2 Loading Dynamics

This section focuses on studying the dynamics of the atoms when loading the $^1S_0$ ODT. Besides presenting the experimental observations, the numerical model is applied to study the loading process quantitatively.

4.2.1 Experimental Observations

The dynamics of the loading process are studied by varying the power of the pump laser used for loading the atoms into the $^1S_0$ ODT. After a various time, the loading process of the ODT is finished and an absorption imaging beam is applied to detect the instantaneous number of the atoms in the trap.

The experimental results are shown in Figure (4.4(a)), where loading curves are shown for four different pump power levels. The loading curves lets us determine the capture rate R which is obtained as the initial slope of the exponential fits in Figure (4.4(a)) and is depicted by open circles in Figure (4.4(b)), the 1/e loading time constant τ which is plotted by black squares in Figure (4.4(c)), and, the steady state atom number $\overline{N}$ is shown using black triangles in Figure (4.4(b)).

Starting from a very low pump laser power, $\overline{N}$ and R increase with increasing pump laser power. The photon scattering rate is proportional to the intensity of the pump beam before the onset of saturation. Therefore, for a very low pump laser intensity, an increase of the pump laser power results in an increase of the value of R and thus an increase of $\overline{N}$. Accordingly, τ decreases because of an increase of evaporative loss as the density in the ODT is increased.

When the intensity of the pump laser approaches the saturation intensity, the values of R and $\overline{N}$ decrease and the number of τ slightly increases. When saturation of the pumping transition is approached, the effective pumping volume begins to exceed the capture volume of the ODT. This means that many $^3P_2$ triplet-MOT atoms are pumped outside this capture volume which is less effectively refilled. Therefore, for high pump powers, R decreases again

yielding a decrease of $\overline{N}$, which should be accompanied by an increase of τ due to reduced evaporation.

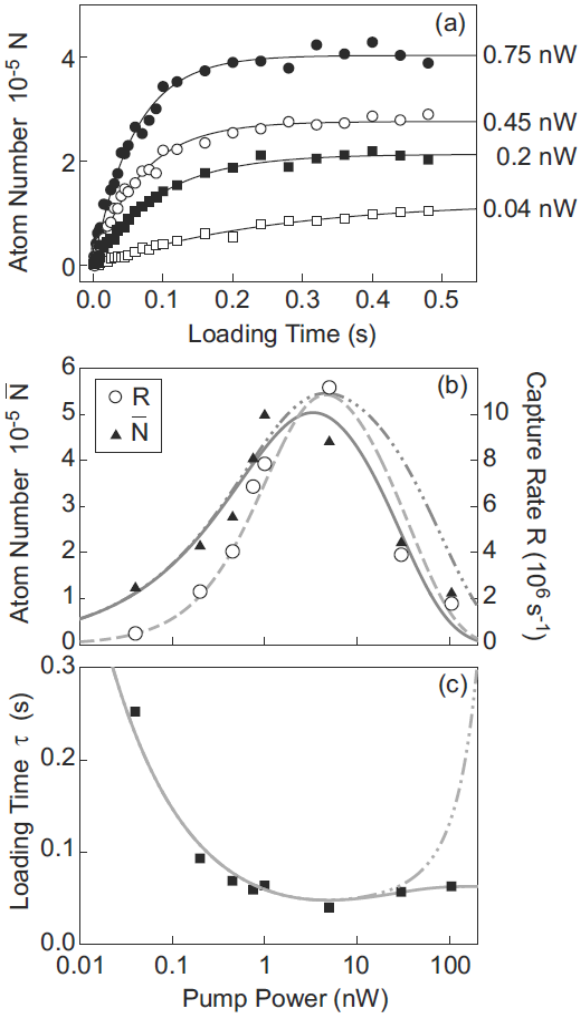

Figure 4.4: (a) Trap loading measurements, shown for different values of the optical pumping power indicated on the right margin. The solid lines are exponential fits. (b) The black triangles show the measured steady-state number of atoms $\overline{N}$. The solid and the dashed-dotted lines depict the results of the model discussed in Section (4.2.2), when γ_B is included and when $\gamma_B = 0$, respectively. The open circles show the measured capture rate R and the respective calculations given by the dashed line. In (c) the 1/e loading time τ is plotted. The solid and the dashed-dotted lines show the calculated values, if γ_B is included and if $\gamma_B = 0$, respectively.

4.2.2 The Numerical Model

Although some of the experimentally observed features can be understood qualitatively from intuitive considerations, a numerical analysis allows for quantitative studies of the more complicated effects.

The instantaneous number of atoms N in the $^1S_0$ ODT is given by

$$\dot{N} = R(P) - (\gamma + \gamma_B(P))N - \gamma_{ev}(T)N^2 \tag{4.1}$$

here $R(P)$ is the effective capture rate of the $^1S_0$ ODT for singlet atoms at a given pump laser power P. γ is the loss rate independent of the pump laser power which includes collisions with fast background atoms or the atoms trapped in the $^3P_2$ triplet-MOT. $\gamma_B(P)$ is the additional loss rate depending on the pump laser power P. This parameter takes into account the collisions between the $^1S_0$ atoms trapped by the $^1S_0$ ODT, and, $^1S_0$ and $^3P_1$ atoms which are optically pumped outside of the ODT volume when larger pump powers are applied. $\gamma_{ev}(T)$ is the temperature-dependent two-body loss parameter accounting for evaporative loss via elastic binary collisions between trapped singlet atoms.

To understand $R(P)$ and $\gamma_B(P)$, the ballistic trajectory $\xi(t)$ of an atom in the $^3P_2$ triplet-MOT passing through the volume of the ODT, V_{ODT}, and the optical pumping rate $\Gamma(P, \xi(t))$ are utilized. The assumption of the ballistic nature of the atomic motion appears well justified on the tens of microns length scale given by the waist of the ODT beam. A typical $^3P_2$ triplet-MOT atom with mean velocity $\overline{v}$ (according to its temperature of 300 μK) randomly scatters few tens of infrared photons during the time in which it traverses thought the V_{ODT}, which yields a negligible change of $\overline{v}$. Assuming an atom in the $^3P_2$ triplet-MOT enters V_{ODT} at t_{in} and leaves it at t_{out}, integration of $\Gamma(P, \xi(t))$ along $\xi(t)$ yields the probability for an atom to enter V_{ODT} without being optically pumped, $P_{1,\xi}(P)$, and the probability for an atom that has entered V_{ODT} to leave it unpumped, $P_{2,\xi}(P)$. Thus, the probability of the atoms entering V_{ODT} and being pumped is $P_{in,\xi} \equiv P_{1,\xi}(P)(1 - P_{2,\xi}(P))$ and the probability of the atoms being pumped outside of the V_{ODT} is $P_{out,\xi} \equiv 1 - P_{1,\xi}(P)$. $P_{1,\xi}(P)$ and $P_{2,\xi}(P)$ are given by

$$\begin{aligned} P_{1,\xi}(P) &= \exp(-\int_{-\infty}^{t_{in}} \Gamma(P, \xi(t))dt) \\ P_{2,\xi}(P) &= \exp(-\int_{t_{in}}^{t_{out}} \Gamma(P, \xi(t))dt)\,. \end{aligned} \tag{4.2}$$

Averaging over trajectories and velocities according to the specific temperature of the $^3P_2$ triplet-MOT yields the corresponding average probabil-

ities $P_{in}(P)$ and $P_{out}(P)$. $\Gamma(P, \xi(t))$ is calculated from an average Clebsch-Gordan coefficient taking into account the magnetic substructure of the transition $^3P_2$ [4s4s] to $^3P_2$ [4p4p] in connection with π-polarization of the pump laser beam for a two-level system. t_{in} and t_{out} mentioned here are calculated using the mean velocity at the temperature of the atoms trapped by the $^3P_2$ triplet-MOT ($\approx 300\,\mu$K) and the boundary condition of the V_{ODT} defined by 1/3 of the size of the ODT, corresponding to the trap volume. Thus, the effective capture rate $R(P)$ and the power dependent loss rate $\gamma_B(P)$ can be written as

$$\begin{aligned} R(P) &= R_0 P_{in}(P) \\ \gamma_B(P) &= \gamma_{B,0} P_{out}(P) \end{aligned} \tag{4.3}$$

where R_0 and $\gamma_{B,0}$ are fitting parameters.

Secondly, the evaporative loss parameter may be written as

$$\gamma_{ev}(T) = 0.5\,\gamma_{coll}(T)\,P_{loss}(T) \tag{4.4}$$

where

$$\begin{aligned} \gamma_{coll} &= \sigma_t\,\overline{u(T)}/V_{eff}(T) \\ P_{loss} &\approx 0.5\,\exp(-\eta)\,(\eta^2 + 2\eta + 2) \end{aligned} \tag{4.5}$$

here σ_t is the elastic collision cross section depending on the average temperature of the atoms in the $^1S_0$ ODT and $\overline{u(T)} \equiv 4\sqrt{k_B T/(\pi m)}$ is the mean relative velocity. $V_{eff}(T) \equiv N^2/\int n(r)^2 d^3r$ is the effective trap volume where $n(r)$ is the density distribution of the trapped atoms. $P_{loss}(T)$ is the fraction of collisions yielding evaporation [Ket96], where $\eta \equiv U_0/(k_B T)$ is the truncation parameter and U_0 is the potential well depth.

In order to derive a model for the temperature dependence of the effective trap volume, a harmonic approximation of the ODT potential and η are employed, yielding $V_{eff}(T) = b{w_0}^2\sqrt{\pi^3/2\eta^3}$. Because the ODT potential rapidly opens up towards higher energies, this approach would notably underestimate the trap volume. To account for this factor, a correction factor $\nu(T)$ is introduced writing $V_{eff}(T) = b{w_0}^2\sqrt{\pi^3/2\eta^3}\,\nu(T)$. $b = 2{w_0}^2\pi/\lambda$ is the confocal parameter of the ODT laser beam where w_0 is the beam waist of the ODT laser beam. In the following, the elastic scattering cross-section and the volume correction factor are assumed temperature independent. σ_0 is the elastic collision cross section independent of temperature and ν_0 is the temperature independent correction factor.

According to the previous considerations, the fit parameters in Equation (4.1) can be reduced to R_0, $\gamma_{B,0}$ and σ_0/ν_0. The remaining parameters can

be deduced from the experimental conditions. The well depth U_0 is $350\,\mu$K which has been derived from measurements of the power and the focus of the ODT laser beam. The loss rate has been determined as $1/\gamma = 15\,$s. The initial temperature $T_0 \equiv (T_{ax,0} + 2T_{rad,0})/3 = 157\,\mu$K which results from the initial axial and radial temperatures $T_{ax,0} = 300\,\mu$K and $T_{rad,0} = 85\,\mu$K, respectively. The used radial temperature results from TOF measurements described in the next section. The radial temperature is lower than that of the ^{3}P$_2$ triplet-MOT. It reflects the fact that the energy selectivity of the optical pumping process with respect to the radial degree of freedom of the ODT laser beam. For an extreme aspect ratio difference of the ODT beam, atoms with slow radial velocity remain in the pump beam longer and are efficiently loaded into the ODT. The large axial diameter of the ODT beam prevents any energy selectivity in the loading process. In our experiment, T_{ax} cannot be measured which is impede by a larger axial extension of the trap. Therefore, $T_{ax,0}$ should be roughly given by the temperature of the ^{3}P$_2$ triplet-MOT.

To compare our model with the observations, Equation (4.1) is solved for constant temperature T_0 and fit parameters γ_0, R_0 and σ_0/ν_0, in order to find the $1/e$ loading time $\tau = 1/\sqrt{(\gamma+\gamma_B)^2 + 4R\gamma_{ev}}$ and the steady state atom number $\overline{N} = (1/\tau - \gamma - \gamma_B)/(2\gamma_{ev})$, see Ref. [Gru01].

The fitting procedure is as follows. Firstly, R_0 is adjusted to optimize the agreement with the observed capture rates, the dashed line in Figure (4.4(b)). Secondly, the numbers σ_0/ν_0 and $\gamma_{B,0}$ are adjusted to obtain the solid line in Figure (4.4(c)) to fit the measured loading times. Finally, the steady state atom number $\overline{N}$ has to be multiplied by a factor 0.53 to account for systematic errors in our imaging system and the observed data shown by the solid line in Figure (4.4(b)).

4.2.3 Results

Comparison of the numerical model to the experimental data yields $\sigma_0/\nu_0 = 2.9 \times 10^{-16}\,$m^2. A simple calculation shows that by using a fixed temperature T_0 and a correction factor $\nu_0 \approx 10$, the elastic collision cross section σ_0 is approximately $3 \times 10^{-15}\,$m^2.

In order to understand the power dependent losses $\gamma_B(P)$, the predictions of the model for the case of $\gamma_B(P) = 0$ are plotted, shown by the dashed-dotted curve in Figures (4.4(b)) and (4.4(c)). Obviously $\gamma_B(P)$ is relevant only for pump laser powers exceeding a few nW. For 100 nW, the model predicts a loading time τ given by $1/\gamma_B(p) \approx 60\,$ms. For this high pump laser power, most of the atoms in the ^{3}P$_2$ triplet-MOT outside of V_{ODT} are pumped to the ^{3}P$_1$ state and further spontaneous decay to the ^{1}S$_0$ ground

state yielding a dense background of atoms in the $^1S_0$ state with a density comparable to that in the $^3P_2$ state of the order of $10^{10}\,\mathrm{cm}^{-3}$. Assuming that each trapped $^1S_0$ atom colliding with an untrapped $^1S_0$ atom is lost, $\gamma_B(P) \approx \sigma_0\,\rho_B\,\overline{u} \approx 15\,\mathrm{s}^{-1}$ may be estimated. For a temperature of $300\,\mu$K, we calculate $\overline{u} \approx 50\,\mathrm{cm/s}$ between the atoms in the $^1S_0$ state. Furthermore, a background untrapped $^1S_0$ atoms with comparable density $\rho_B = 10^{10}\,\mathrm{cm}^{-3}$ is produced by means of spontaneous decay. Thus, $\gamma_B(P) \approx 15\,\mathrm{s}^{-1}$ is comparable to the loading time predicted for large pump laser powers. Similarly, collisions between atoms in the $^3P_1$ state and the atoms trapped in the $^1S_0$ ODT can be included, however, the scattering cross section between these atoms is unknown. Consequently, our theoretical analysis indicates that the increased population of $^3P_1$ and $^1S_0$ atoms pumped outside the ODT capture volume acts as an additional background introducing extra losses. Therefore, for larger pump powers, the values of τ is smaller than expected from evaporation of the relatively small ODT population, see the observations in Figure (4.4(c)).

The only three fit parameters ($\gamma_{B,0}$, R_0 and σ_0/ν_0) permit us to model the pump power dependent loading dynamics by the function $R(P)$, $\tau(P)$ and $\overline{N}(P)$ where P is the given pump laser power.

4.3 Evaporative Dynamics

To understand the evaporative dynamics of the atoms in the ODT, the time dependent number and the radial temperature of the atoms after the loading process is finished have been studied. With these results, the axial temperature of the atoms in the ODT can be determined by numerical calculations.

4.3.1 Experimental Observations

After the loading is finished, the atoms are held in the $^1S_0$ ODT for variable times before being released from the trap. Subsequently, the imaging beam is applied for detecting the number and the radial temperature of the atoms. The values of the number and the radial temperatures of the atoms are shown in Figures (4.5(a)) and (4.5(b)), respectively.

4.3.2 The Numerical Model

According to kinetic theory [Ket96] and assuming the atoms have re-thermalized, the time evolution of axial temperature T_{ax} and radial temperature T_{rad}

are given by

$$\begin{aligned} \dot{T}_{ax} &= -1/3\,\gamma_{ev} N (T_{ev}/T - 1) T_{ax} - 2/3\,\gamma_{rel} \Delta T + 4/3\,\gamma_{sc} T_{rec} \\ \dot{T}_{rad} &= -1/3\,\gamma_{ev} N (T_{ev}/T - 1) T_{rad} + 1/3\,\gamma_{rel} \Delta T + 2/3\,\gamma_{sc} T_{rec} \end{aligned} \quad (4.6)$$

where $T \equiv (T_{ax} + 2T_{rad})/3$ and $\Delta T \equiv T_{ax} - T_{rad}$. $k_B\,T_{ev}$ denotes the energy removed per evaporated particle, $k_B\,T_{rec}$ is the photon recoil energy, γ_{sc} is the photon scattering rate of the ODT ($9\,\mathrm{s}^{-1}$), γ_{ev} is the evaporative loss parameter in Equation (4.1) and γ_{rel} is the cross-dimensional relaxation (CR) rate.

The temperature changes in the axial and the radial direction shown in Equation (4.6) account for evaporative cooling processes, energy exchange between different axes due to ergodic mixing of the atomic ensemble, and heating arising from scattering of the trap laser photons. Using Equations (4.6) and (4.1), the dynamics of the atoms after the loading process can be understood.

According to Ref. [Kav00], the CR-rate can be expressed as $\gamma_{rel} = C_{rel}\,\gamma_{coll}\,N$ with a constant C_{rel} depending on the exact model of the scattering cross section and the collision parameter γ_{coll} from Section (4.2.2). The theoretical value of the CR-rate is predicted to be $C_{rel} = 2/5$ [Han06b, Mon93, Hop00, Arn97, Sch03, Spo05]. The best overlap with experimental results is achieved for $C_{rel} = 1/11$ using a temperature independent scattering cross section. The adjustment of C_{rel} yields a decent description of the decay dynamics including a prediction of the final radial temperature and particle number.

The value of T_{ev} can be obtained from the detailed balance model [Ket96] used in the context of Equation (4.1) as

$$k_B T_{ev} = U_0\,(\eta^3 + 3\eta^2 + 6\eta + 6)\,/\,(\eta^3 + 2\eta^2 + 2\eta)\,. \quad (4.7)$$

Applying the same parameters obtained from Section (4.2.2) namely that $T_{ax,0} = 300\,\mu\mathrm{K}$, $T_{rad,0} = 85\,\mu\mathrm{K}$ and the value of σ_0/ν_0 obtained from Figures (4.4(b)) and (4.4(c)), Equation (4.6) can be solved by using Equation (4.1) for the case of $R(P) = 0$ and $\gamma_B = 0$. Also, N can be calculated using a calibration factor of 0.53. The results for N and T_{rad} are plotted by the solid line in Figures (4.5(a)) and (4.5(b)). The axial temperature T_{ax} calculated is provided by our model. The results are plotted by a dashed line in Figure (4.5(b)).

4.3.3 Results

The graphs in Figures (4.5(a)) and (4.5(b)) show that during the first 50 ms a fast loss of atoms occurs, while the radial temperature decreases from

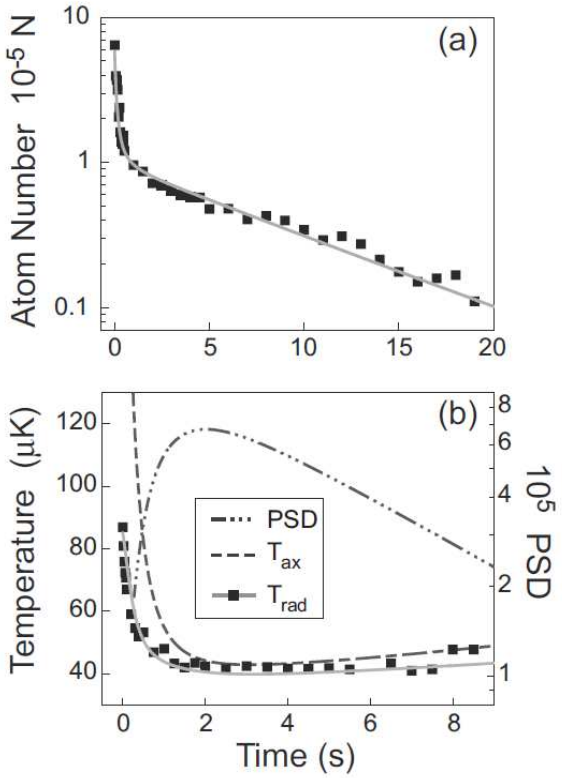

Figure 4.5: The decay measurement and TOF measurements of the atoms in the $^1S_0$ ODT. The time dependent number of the atoms in the $^1S_0$ ODT is shown by the black squares in (a). The radial temperatures of the trapped atoms are presented by black squares in (b). The solid gray lines in (a) and (b) are the results from the numerical model. The dashed line and the dash-dotted-dotted line in (b) are the calculated axial temperature and PSD of the trapped atoms, respectively. The details are described in the text.

$T_{rad,0} = 85\,\mu$K to a value close to $40\,\mu$K, which is attributed to evaporation. For later times, the slower particle loss results from collisions with atoms from the hot background. Additionally, a slow temperature increase results from heating arising from scattering of the trap laser photons and collisions with hot background atoms.

The PSD of the trapped atoms can be obtained by the results from the numerical models that have been developed. Using the harmonic approximation with the constraint that the value of η is large, the PSD is given by $N\hbar^3\omega_{ax}{\omega_{rad}}^2/(k_BT)^3$. The axial frequency ω_{ax} and the radial trap frequency ω_{rad} of the trap is $2\,\pi\times 20.3\,$Hz and $2\,\pi\times 3.8\,$kHz, respectively, see Section

(2.2). The calculated PSD is indicated by the dashed-dotted-dotted line in Figure (4.5(b)). The PSD of the atoms in the $^1S_0$ ODT reaches 6×10^{-5} which is approximately three orders of magnitudes larger than that of the atoms in the $^3P_2$ triplet-MOT, 4.1×10^{-8}. The much larger PSD indicates that the loading process is not limited by an extreme volume difference between the $^3P_2$ triplet-MOT and the ODT, the radiation trapping effect in the $^3P_2$ triplet-MOT and inelastic collisions between the atoms in the $^3P_2$ state.

4.4 Conclusion

An efficient loading scheme has been demonstrated. It is based on an energy selective optical pumping with respect to the radial degree of freedom of the ODT laser beam and is mainly limited by evaporation. Utilizing the continuous loading scheme, an excellent capture rate of up to $10^7\,s^{-1}$ is obtained. In the steady state, there are 5×10^5 atoms in the ODT with $300\,\mu$K axial temperature and $85\,\mu$K radial temperature resulting in a peak density of $3.5 \times 10^{10}\,cm^{-3}$. After 50 ms of efficient plain evaporation, there are 10^5 atoms at $42\,\mu$K with a peak density of $5.3 \times 10^{11}\,cm^{-3}$. The low initial radial temperature indicates a selection of low-energy atoms during the pumping process.

The numerical models are applied to understand the dynamics of ODT atoms during the loading process and after the loading is terminated. Moreover, using the developed numerical models, the axial temperature of atoms in the ODT is determined. Notice, there are many simplifications applied in the models, such as the harmonic approximation of the ODT potential and the use of an average temperature in the determination of the elastic collision rate. Although the models are simple, the good fitting of experimental observations indicate the relevant physical mechanisms are presented. The models provide us with important insights of the dynamic loading process.

Chapter 5

The Crossed Optical Dipole Trap

As shown in Chapter 4, the PSD of the atoms in the ODT is increased by nearly three orders of magnitude compared to that in the $^3P_2$ triplet-MOT. But, the PSD of the atoms in the ODT cannot be increased further after about 2 s of holding time in the trap, see Figure (4.5(b)). In order to prevent stagnation of evaporation, the method of a forced evaporation is required.

Forced evaporative cooling is a standard path to achieve BECs. It is carry out by continuously ramping down the threshold for evaporation in order to maintain a constant or increasing elastic collision rate. For an ODT, forced evaporation is carried out by ramping down the well depth, see Section (2.3.1). Despite this, a BEC is difficult to reach using a single beam ODT system due to the weak confinement along the beam axis. An ODT is an anisotropic trap with a strong confining force in the radial direction and a weak confinement along the beam propagation axis. Since the trap frequency is related to the depth of an ODT, forced evaporation is accompanied with a decrease in the confining force, see Equation (2.16). As a result, during forced evaporation, the weak axial confinement of an ODT results in a decrease in density of the atoms and yields a reduced elastic collision rate. Thus, it leads to a stagnation of evaporation.

To avoid a stagnation of evaporation, a CODT setup is used in the experiment. A CODT consists of two ODTs. The foci of the ODT beams intersect. Therefore, the setup provides additional confinement along the beam axes of the ODTs. The crossed region acts as a dimple in the reservoir formed by the non-crossed region. A large amount of cold atoms are trapped in two ODTs and then loaded into the dimple by elastic collisions. The atoms in the dimple are in thermal contact with the reservoir. Their temperature will be the same, but the density is increased strongly following the Boltzmann

factor $\exp(U/k_BT)$, where U denotes the trap depth. Therefore, the PSD is locally increased. Accordingly, a CODT setup provides an advantageous starting condition for evaporative cooling.

The CODT setup in the system follows that for the ^{174}Yb re-search [Tak03]. Two ODTs are applied in the horizontal and vertical planes, respectively. The experimental results of the CODT setup are presented in two chapters. This chapter shows the characteristics of the two individual ODTs, the characteristics of the trapped atoms in the dimple and the results of the developed numerical model. Experimentally, some atoms remain in non-crossed regions of the CODT, the so-called wings of the CODT, after the loading process is finished. Difficulties arise for investigating collisional properties of the atoms in the dimple due to the fact that the system is not in an equilibrium state. The atoms distributed in the wings may load into the dimple via elastic collisions. Thus, a numerical model is applied for studying the effecs of the atoms trapped in the wings upon the atoms trapped in the dimple. Afterwards, forced evaporation is applied. The results of evaporation are demonstrated in the next chapter.

5.1 Experimental Overview

The loading process for the $^1S_0$ CODT is similar to that for the single $^1S_0$ ODT, see Section (4.1). Initially, after the $^3P_2$ triplet-MOT is loaded for 3 s by the $^1S_0$ singlet-MOT, the $^1S_0$ singlet-MOT is extinguished and two ODTs are enabled. The foci of the ODT beams intersect at the center of the $^3P_2$ triplet-MOT. To load atoms into the CODT, two pump beams are applied. The foci of the pump laser beams and the ODT beams are well superimposed. For the loading process, the frequency of the beams of the $^3P_2$ triplet-MOT and the power of the pump laser beams are adjusted to maximize the number of atoms loaded into the dimple. After the loading process is terminated, the atoms are released from the trap and subsequently absorption images are taken.

The circularly polarized fiber laser at 1064 nm used as the HODT provides a well depth of 372 μK for the $^1S_0$ ground state, that takes into account a laser power of 13.5 W in the vacuum system and a beam waist radius of 31 μm. The linearly polarized Verdi laser at 532 nm used as the VODT offers a depth of 615 μK for the $^1S_0$ ground state which is calculated using a laser power of 3.22 W in the vacuum system and a beam waist radius of 15.8 μm. The beam waists of the two ODTs are determined by trap frequency measurements which are described in Section (5.2.1). Two linearly polarized pump laser beams with Gaussian beam radii of 17 μm and 16 μm are applied

for loading atoms into the HODT and the VODT, respectively.

Considering the optical pumping process, the polarization of the HODT beam is chosen to be circular. Figure (5.1) shows the optical potentials for the different quantum states of ^{40}Ca atoms calculated for a laser beam at different wavelength with a power level of 13.5 W and a beam waist radius of 31 μm for three different polarization states. As shown in Figure (5.1(A)), for a linearly polarized beam at 1064 nm, the deepest negative light shift occurs for the $^3P_2$ ($m = 0$) metastable substate. However, since the pump laser is linearly polarized, the optical transition from the Zeeman substate at $m = 0$ to $m = 0$ is forbidden. This means that the atoms trapped in the deepest metastable ODT cannot be pumped and loaded into the $^1S_0$ ODT. Plots (B) and (C) in Figure (5.1) show the optical potentials calculated for right circularly and left circularly polarized light at different wavelengths for the different energy state of ^{40}Ca atoms, respectively. For 1064 nm radiation, the most negative light shifts occur for the $^3P_2$ ($m = \pm 2$) states. Therefore, the atoms trapped in the deepest metastable ODT can be loaded into the $^1S_0$ ODT.

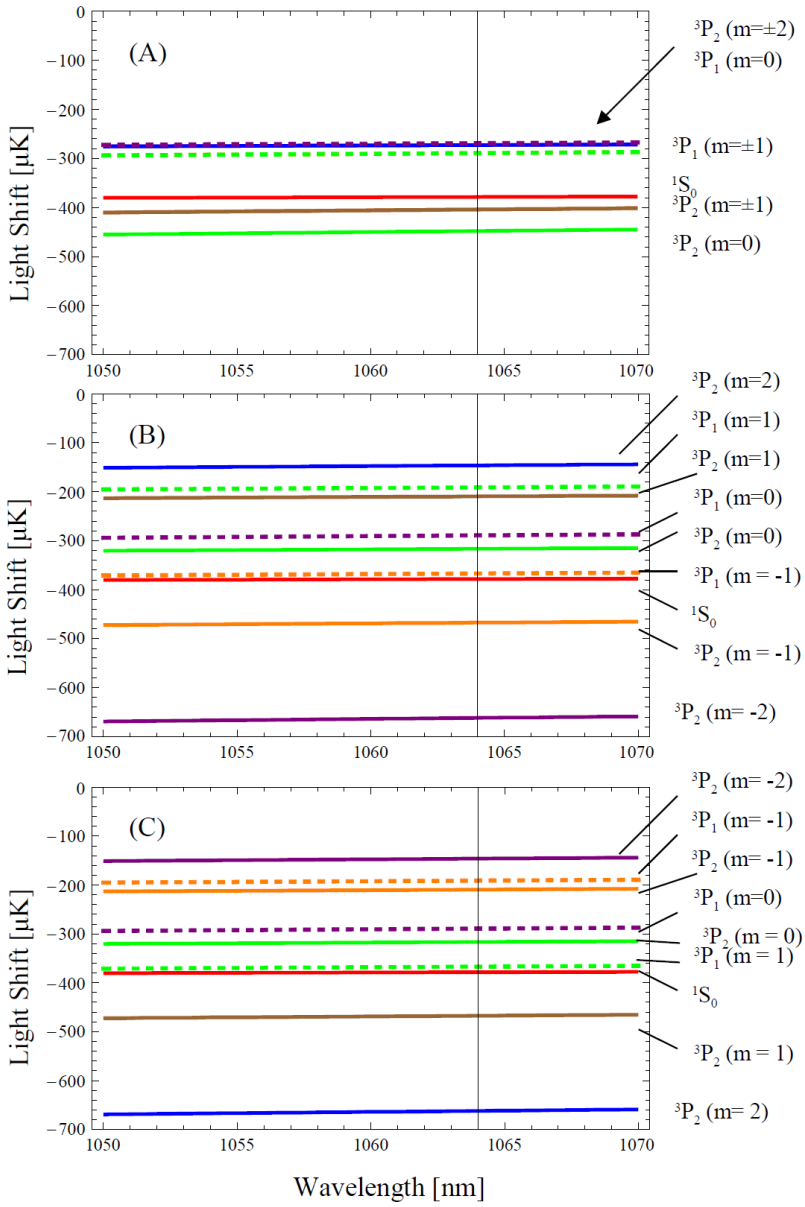

Figure 5.1: Light shifts in μK at different wavelengths of a laser beam for the different energy states of ^{40}Ca atoms. The results are calculated using a laser beam with a beam power of 13.5 W and a Gaussian beam waist radius of 31 μm. Plots (A), (B) and (C) show the light shifts calculated by the beam with π-, σ^+- and σ^--polarization, respectively. Further information is provided in the text.

5.2 Parameters of the $^1S_0$ ODTs

5.2.1 Trap Frequency Measurements

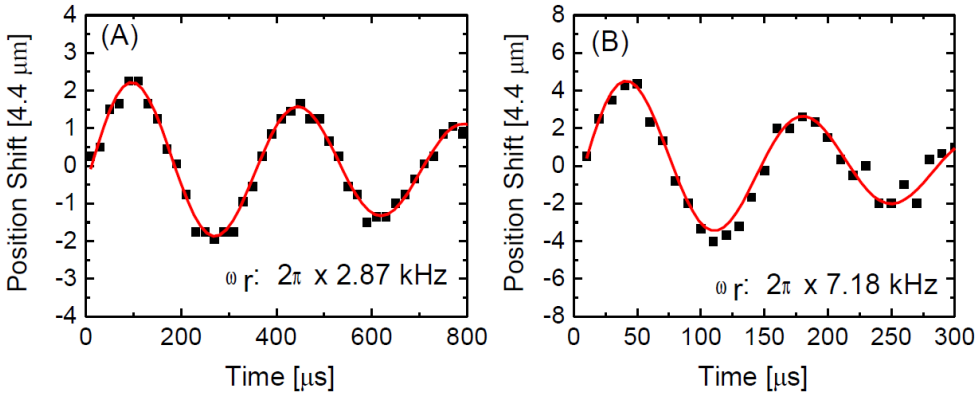

Figure 5.2: Results of the trap frequency measurements. Black squares and red solid lines correspond to the experimental data and fit results, respectively. Plot (A): oscillation frequency measurement of the HODT with the full laser power of 13.5 W in the vacuum system. Plot (B): oscillation frequency measurement of the VODT with the full laser power of 3.22 W in the vacuum system.

To measure the radial oscillation frequency, the ODT beam is suddenly shifted a few μm by adjusting the RF frequency of the AOM after the atom loading process is finished. Note that the position shift was kept small enough to ensure that the atoms were still located in the harmonic potential. After the trap is shifted, the trapped atomic ensemble oscillates between different positions in the trap with respect to trap holding time. Subsequently, the absorption imaging method is applied to record the position of the trapped atoms after the atoms are released from the trap and expand. For the measurements, the CCD chip at position 1 is used, see Figure (3.2).

The results are shown in Figure (5.2). Plots (A) and (B) display the results of the trap frequency measurements of the HODT and the VODT in the $^1S_0$ state with their full laser powers. The resulting radial trap frequency of the HODT is $2\pi \times 2.87$ kHz which derives from the beam waist radius of 31 μm. The resulting trap depth of the HODT is 372 μK. Similarly, for the VODT, the resulting radial trap frequency is $2\pi \times 7.18$ kHz which derives from the beam waist radius of 15.8 μm. The resulting trap depth of the VODT is 615 μK with taking into account the gravitational potential.

5.2.2 Lifetime and Temperature Measurements

Figure (5.3) shows the lifetime and TOF measurements of the atoms trapped in the full power HODT for two different polarizations. The pressure level of the vacuum system for these measurements is about 6×10^{-10} mbar.

Plot (A) presents the results of the lifetime measurements. Initially, there are 2×10^6 atoms trapped in the circularly polarized HODT (black squares) and about 5×10^5 atoms trapped in the linearly polarized HODT (open hexagons). The resulting 1/e lifetime is about 5 s for both polarizations of the HODT. This result is given by fitting the time dependent atom number after 0.5 s of trap holding time with an exponential decay curve (red solid lines), see Equation (2.25), assuming that the atom losses are only due to collisions with fast background atoms.

TOF measurements are shown in Plot (B). For the linearly polarized HODT (open hexagons), the radial temperature of the trapped atoms is reduced from 52 μK to 27 μK after plain evaporation. For the circularly polarized HODT (black squares), the radial temperature of the trapped atoms is reduced from 43 μK to 25 μK after plain evaporation. Thus, comparing this to the linearly polarized HODT, the circularly polarized HODT can trap more atoms at a lower temperature.

The axial temperature of the trapped atoms cannot be measured, which is impeded by the extreme aspect ratio of the ODT. Following the numerical models which were developed in Chapter 4, the axial temperature of the trapped atoms can be inferred. The parameters used here are $R = 0$, $\gamma_B = 0$, $\nu_0 = 10$, $C_{rel} = 0.095$, $\gamma = 1/4.5$ and the $^1S_0$ ground state scattering length of $440\, a_0$ [Kra09]. These parameters are defined in Chapter 4. Other parameters for modeling can be deduced from the experimental conditions.

Plot (C) shows the radial and axial temperature fits as well as the calculated PSD of the trapped atoms in the circularly polarized HODT. The fits to the radial and axial temperatures of the trapped atoms are presented by the red solid line and the blue dashed-dotted line, respectively. Using the fit temperatures and the fit number of the atoms, the PSD of the trapped atoms can be calculated[1] which is shown by the black dashed line. The highest PSD of the trapped atoms in the circularly polarization HODT is about 3×10^{-4}.

Figure (5.4) shows experimental results of measurements the atoms trapped in the VODT with its full beam power. Plot (A) shows the lifetime measurement of the atoms. Initially, there are about 1×10^5 atoms trapped in the VODT. The resulting 1/e lifetime is 1.7 ± 0.05 s. This result is given by fitting the time dependent atom number after 0.5 s of trap holding time with an exponential decay curve (red solid lines), assuming that atom losses

[1] see Section (4.4)

are only due to background collisions. Plot (B) shows the results of the TOF measurements of the trapped atoms, the fit results of the temperatures and the calculated PSD of the trapped atoms. These results show a reduction of the radial temperature of the trapped atoms from $83\,\mu$K to $52\,\mu$K after plain evaporation. The axial temperature of the trapped atoms is inferred from the numerical models which were developed in Chapter 4. The parameters used here are $R=0$, $\gamma_B=0$, $\nu_0=10$, $C_{rel}=0.11$, $\gamma=1/1.7$ and the ^{1}S$_0$ ground state scattering length of $440\,a_0$ [Kra09]. These parameters are defined in the same way as in Chapter 4. Other parameters for modeling were deduced from the experimental condition. Using the fit temperatures and atom numbers, the highest PSD of the atoms in the VODT calculated is about 7.4×10^{-5}, shown by the black dashed line.

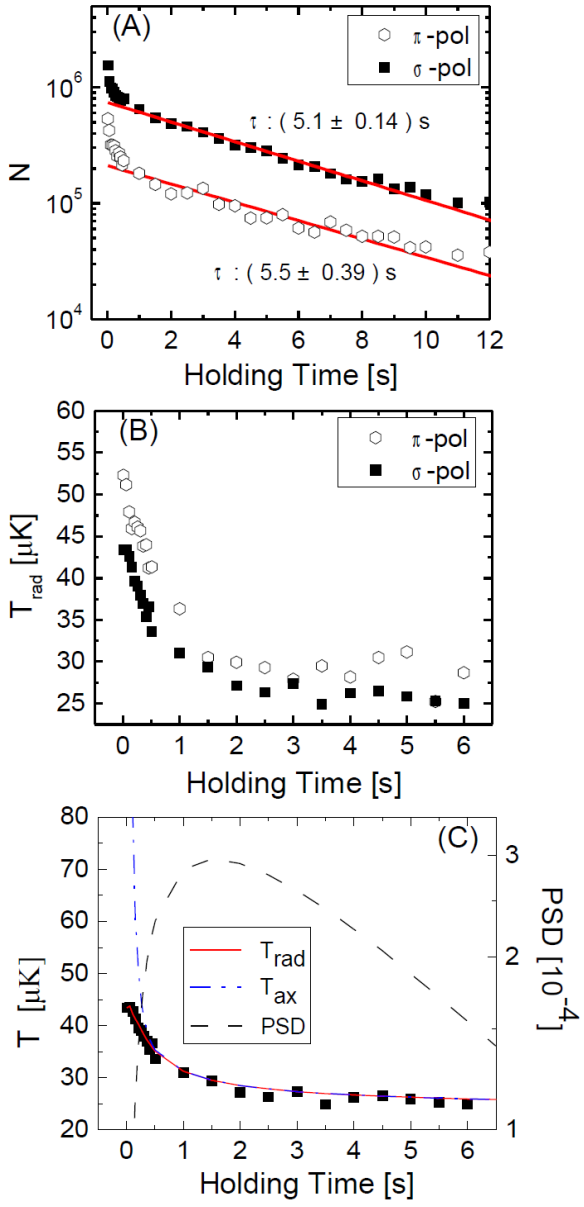

Figure 5.3: Lifetime and temperature measurements of the atoms in the HODT. The HODT parameters are a power level of 13.5 W in the vacuum chamber and a beam waist radius of 31 μm. Black squares are the experimental data measured by the circular polarized (σ-pol) HODT and open hexagons are the experimental data measured by the linear polarization (π-pol) HODT, respectively. Plot (A) shows results of the lifetime measurements, where N is the number of atoms. The resulting 1/e lifetimes are about 5 s (red solid lines). Plot (B) shows the radial temperature of the atoms T_{rad}. Plot (C) shows the fit results of the radial (red solid line) and axial temperature T_{ax} (blue dashed-dotted line) changes of the trapped atoms in the circularly polarized HODT. The PSD of trapped atoms (black dashed line) is calculated using the fit temperatures and atom numbers. Further details are described in the text.

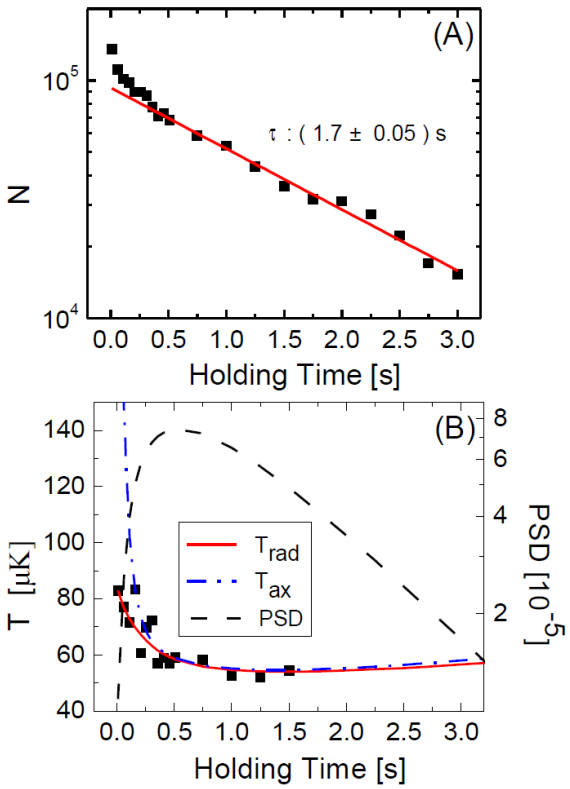

Figure 5.4: Lifetime and temperature measurements of the atoms in the VODT. The VODT parameters are a power level of 3.22 W of linearly polarized light in the vacuum chamber and a beam waist radius of 15.8 μm. Black squares represent the experimental data. Plot (A) shows the result of the lifetime measurement. N is the number of atoms. The resulting 1/e lifetime is 1.7 ± 0.05 s (red solid line). Plot (B) shows fit results of the radial T_{rad} (red solid line) and axial temperatures T_{ax} (blue dashed-dotted line) of the trapped atoms. The PSD of the atoms (black dashed line) is calculated using the fit atom temperatures and atom numbers. Further details are described in the text.

5.3 Characterization of the $^1S_0$ CODT

After the atom loading process for the CODT is finished, the number and temperature of the trapped atoms in the dimple are detected by the absorption imaging method with the CCD camera at position 2, see Figure (3.2(B)). The lifetime and the three-body collision loss coefficient of the atoms could be calculated from the data.

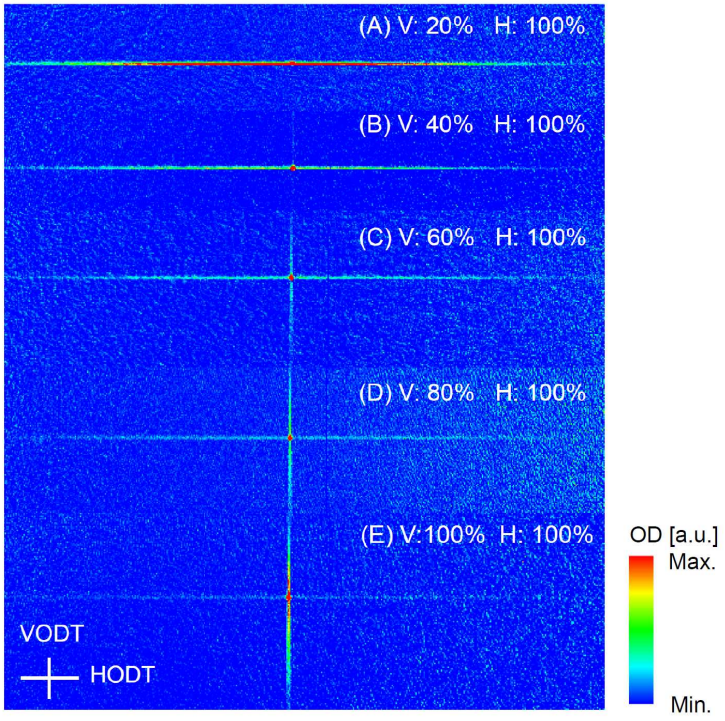

Figure 5.5: Images of the CODT for different powers of the VODT laser beam. The images are taken after the loading process is terminated and 0.5 s of trap holding time. It shows that atoms reside in different positions of the wings depending on the depth of the ODTs. In the images, indices V and H show the percentage of the maximum VODT and HODT beam powers, respectively. The orientations of the VODT and the HODT are marked in the images. Further details are described in the text.

After the loading process is terminated, there are still atoms located in the wings during the 3 s trap holding time. This means that the system is not in the equilibrium state because the atoms in the wings may still collide with the atoms in the dimple and with other atoms in the wings, and then

load into the dimple via elastic collisions. Therefore, due to the limitations from the atoms in the wings, collisional properties of the atoms in the dimple can not be studied. Figure (5.5) presents images of the CODT for different powers of the VODT laser beam. The images are taken after the loading process is terminated and 0.5 s of trap holding time. It can obviously be seen that after the loading process is finished, atoms locate at different positions in the wings depending on the depths of the ODTs. When the depth of the HODT is deeper than that of the VODT, there are still atoms mainly in the wings of the HODT, see images (A) and (B). Similarly, for a deeper VODT, there are atoms mainly in the wings of the VODT, see the images (D) and (E). When the depths of two ODTs are equal, atoms reside in four different wings of the CODT, see the image (C).

Figure (5.6) shows the experimental results and calculated properties of the atoms in the dimple formed by the full power of the CODT. The pressure level of the vacuum is approximately 4×10^{-9} mbar for the measurements. Plot (A) shows the result of the lifetime measurement with respect to trap holding times equal to 4 s. Plot (B) shows the lifetime measurement of the trapped atoms with respect to trap holding time from 0.75 s to 5 s (black squares) and the calculated peak density (open hexagons). Plot (C) shows the result of TOF measurements (black squares) and the calculated PSD (open stars) of the trapped atoms.

Two lifetime measurements were taken in order to estimate the lifetime of the atoms in the dimple. Experimentally, in order to avoid an optical density too high such that the limit of the CCD is reached, the number of the atoms is detected after the atoms are released from the trap and expanded. Therefore, the lifetime measurements in Figures (5.6(A)) and (5.6(B)) are taken for different durations of trap holding time. As shown in Figure (5.6(A)), initially there are about 2×10^5 atoms trapped in the dimple. The number of the atoms increases during the first 60 ms and decays quickly afterwards. As shown in Figure (5.6(B)), the 1/e lifetime of the atoms is 2.6 ± 0.09 s. The lifetime is obtained by an exponential fit of the atom numbers after 3 s of trap holding time assuming that two and three-body collisions of the atoms are excluded, which is shown by the red solid line in Figure (5.6(B)). There is no atom remain in the wings after 3 s of trap holding time.

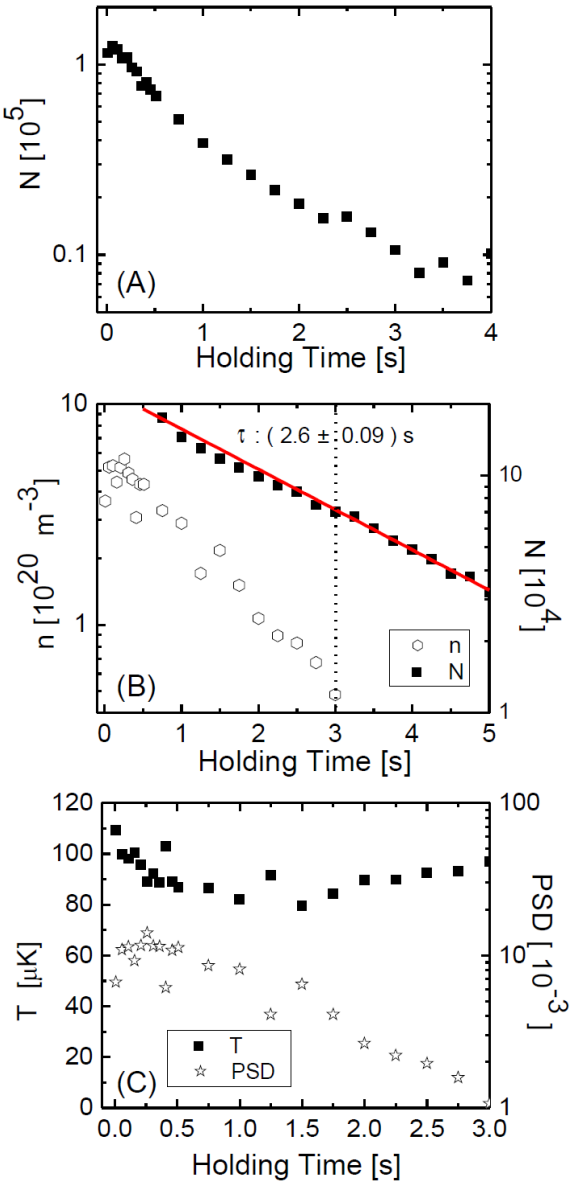

Figure 5.6: Characteristics of the atoms in the dimple formed by the full power $^1S_0$ CODT. (A) shows the results of the lifetime measurements during the 4 s trap holding time. (B) presents the results of the lifetime measurements during the 0.75 s to 5 s trap holding time (black squares) and the calculated peak density n (open hexagons). The lifetime of the atoms in the dimple is given by fitting the atom numbers N after 3 s of trap holding time with an exponential decay curve. The resulting 1/e lifetime of the atoms in the dimple is 2.6 ± 0.09 s. (C) presents the time dependent temperature T (black squares) and the calculated PSD (open stars) of the trapped atoms. Further details are described in the text.

Physical parameters applicable to Figure (5.6) follow the definitions in Section (2.3) assuming a harmonic potential well for the dimple. As one can see in Figures (5.6(B)) and (5.6(C)), the peak density and the PSD of the trapped atoms increase during the first 0.25 s. The peak density of the atoms reaches the level of $10^{20}\,\mathrm{m}^{-3}$. The PSD of the atoms is increased by two orders of magnitude compared to that of a single beam ODT system. The highest peak density and PSD obtained are about $5\times10^{20}\,\mathrm{m}^{-3}$ and 0.014, respectively. In summary, the density and the PSD of the trapped atoms have been successfully increased by the CODT setup compared to those of the single beam ODT system.

5.4 Dynamics of the Atoms in the Dimple

In order to study the effects of the atoms in the wings to the atoms in the dimple, a numerical model has been developed.

5.4.1 The Theoretical Model

In this section, the atoms trapped in the wings and in the dimple are denoted by 'wing-atoms' and 'dimple-atoms', respectively, in order to simplify the writing.

The effects of the wing-atoms upon the dimple-atoms are difficult to estimate due to the fact that the characteristics of the wing-atoms and the dimple-atoms cannot be measured separately by our experimental setup. In order to simplify the situation, the atoms in the wings and the dimple are naively treated as two separate systems. Atoms in each system are able to transfer to the other system by collisions. The processes can be illustrated by the following physical picture. For the wings, the atom number decreases because some atoms are loaded into the dimple via elastic collisions and lost due to background collisions and evaporation. On the other hand, the atom number increases because some dimple-atoms are ' loaded ' into the wings due to evaporation and three-body collision losses. For the dimple, the atom number increases due to the fact that some atoms come from the wings. The total atom number decreases as a result of the losses via evaporation and three-body collisions.

In order to estimate the properties of the wing-atoms, one assumption for modeling is that the dimple is small enough that the wings of the CODT are unaffected by the loading process of the dimple. Therefore, the experimental measurements of the atoms in the individual ODT can provide us a direct way to estimate the properties of wing-atoms. However, since the axial tem-

perature of the atoms in the single beam ODT cannot be measured limited by a extreme large axial trap diameter, the numerical models developed in Chapter 4 are utilized. By fitting the experimental observations with the numerical models, the time dependent number and temperature of atoms in the ODT can be inferred. The numerical models in Chapter 4 have taken into account the factors which causes and internal energy changes of the atoms. i.e., evaporation, background collisions and trap laser photons. Therefore, the given time dependent number of wing-atoms has counted the losses due to evaporation and background collisions. Similarly, the given time dependent temperature of wing-atoms has considered the factor of evaporation.

Theoretically, the dynamics of the dimple-atoms could be investigated if the behavior of the dimple-atoms could be described by differential equations which can be numerically solved to fit the experimental data. Therefore, the dynamics of the atoms are described using differential equations in the following.

The Number of Wing-Atoms

Firstly, let us discuss the number of atoms in the wings. Besides the wing-atoms loading into the dimple, the atoms lost from the dimple are transferred into the wings due to evaporation and three-body collisions. Therefore, the total number of wing-atoms N_{wt} is the sum of three items given by

$$N_{wt} \;=\; N_w + \; F_2 \Gamma_{ev,d}\, N_d + F_3\, \Gamma_{3B}\, N_d \tag{5.1}$$

here N_w denotes the time dependent number of wing-atoms which includes losses due to background collisions and evaporation and is provided by the fit result of the numerical models described in Chapter 4. N_d is the time dependent number of dimple-atoms. The second and third terms correspond to dimple-atom losses due to evaporation and three-body collisions, respectively. $\Gamma_{ev,d}$ is the evaporation rate of the dimple-atom, see Equation (2.21), where the index d refers to the dimple-atoms, the s-wave scattering cross section is energy dependent and the value a is given by Ref. [Kra09]. Γ_{3B} is the three-body collision rate of ^{40}Ca atoms in the $^1S_0$ ground state, see Equation (2.26), where the values of L_{3B} is given by Ref. [Kra09]. In this differential equation, two fitting parameters, F_2 and F_3, are introduced to obtain the best fit results.

The Dynamics of the Dimple Loading

Once the total number of wing-atoms is calculated, one should determine how these atoms load into the dimple. Inspired by Ref. [Com06], the number of

wing-atoms loaded into the dimple could be simply estimated by the flux of wing-atoms entering the dimple area times the probability P_L of each wing-atom to load into the dimple via elastically colliding with other wing-atoms traveling inside the dimple region.

The probability P_L of each wing-atom to load into the dimple depends on the energy change occurring during a collision. There are two types of collisions occurring between atoms to load the dimple from the wings. First: the collisions between two wing-atoms near the center of the dimple. This process causes one colliding atom to transfer into the dimple, which occurs at its energy is smaller than the trapping energy of the dimple. Second: the collision between one wing-atom and one dimple-atom. This process leads to the possibility of the dimple-atom ending up trapped in the dimple. To simplify the model, only the first type of collision is taken into account.

Assuming one wing-atom is loading into the dimple after a collision occurs, the probability of a wing-atom to load into the dimple P_L is given by

$$P_L = \frac{1}{2}\Gamma_{el,w} \tag{5.2}$$

here $\Gamma_{el,w}$ is the elastic collision rate of a wing-atom where the index w refers to the wing-atoms, see Equation (2.19). The factor 1/2 results from one colliding wing-atom loading into the dimple after an elastic collision occurs [Com06].

The rate of the wing-atoms passing through the dimple area needs to take into account both the oscillation time t_{osc} and the collision time t_{coll} between two elastic collisions. Firstly, the oscillation time t_{osc} corresponds to the period of time that an atom is almost back to the same position in a harmonic trap. t_{osc} is defined by $m{V_w}^2 = k_B T$ where $V_w = z_{R,w}/t_{osc}$ and $z_{R,w}$ is the Rayleigh range of the ODT laser beam where the wing-atoms are located. The second time is the average time interval between two collisions in the wings. t_{coll} is given by $1/\Gamma_{el,w}$. To simplify matters, one assumption this model makes is that the wing-atoms are not in the hydrodynamical region, i.e., t_{coll} is larger than t_{osc}.

During the time interval t_{coll}, the number of the wing-atoms entering the dimple region ΔN_{pass} is given by

$$\Delta N_{pass} = N_{wt} \frac{{r_d}^2}{z_{R,w}\, r_w} \frac{t_{coll}}{t_{osc}} \tag{5.3}$$

where the parameter ${r_d}^2/(z_{R,w}\, r_w)$ is derived from the ratio between the areas of the dimple and of the wings, r_w is the beam waist of the ODT where the wing-atoms are, $r_d = \sqrt{{r_h}^2 + {r_v}^2}$ is an effective beam radius of the dimple

where r_h and r_v are the beam radii of the HODT and the VODT at the dimple region, respectively. Before colliding with another atom from the wings, the atom passes through the dimple region a maximum of t_{coll}/t_{osc} times.

During the time interval $\Delta t > t_{coll}$, the number of wing-atoms loaded into the dimple is given by

$$\Delta N_L = R_f \, \Delta N_{pass} \, \frac{\Delta t}{t_{coll}} \, P_L \tag{5.4}$$

and it leads to a differential equation

$$\dot{N}_L = R_f \, N_{wt} \, \Gamma_{el,w} \, {r_d}^2 / (2 \, z_{R,w} \, r_w \, t_{osc}) \tag{5.5}$$

where $\Delta t/t_{coll}$ describes how many times the atoms collide in the time interval Δt and P_L is the probability of loading the dimple of a wing-atom. In Equation (5.4), the fitting parameter R_f was introduced for scaling ΔN_L.

The Dynamics of the Atoms in the Dimple

The dynamics of the dimple-atoms can be studied by the time dependent number and temperature of the atoms. Firstly, the time dependent atom number N_d in the dimple is described by

$$\dot{N}_d = \dot{N}_L - \Gamma_{BG} \, N_d - F_2 \, \Gamma_{ev,d} \, N_d - F_3 \, \Gamma_{3B} \, N_d \tag{5.6}$$

here the first term describes the atoms loading from the wings. The second, third and fourth terms describe dimple-atom losses due to background collisions, evaporation and three-body collisions, see Section (2.4). Since the atoms are trapped in the absolute ground state of ^{40}Ca, inelastic two-body collisions are not taken into account.

Secondly, the internal energy changes of the dimple-atoms are expressed by

$$\dot{T}_d = -\frac{F_2 \, \Gamma_{ev,d}}{3} \, (\eta_d + \frac{\eta_d - 5}{\eta_d - 4}) \, T_d + \frac{F_3 \, \Gamma_{3B}}{3} \, T_d \tag{5.7}$$

here T_d denotes the temperature of the dimple-atoms. The first and the second term in Equation (5.7) are contributed by the evaporative cooling process and the three-body recombination process, respectively. The evaporative cooling process provides a cooling mechanism and the three-body recombination process causes heating of the trapped atoms.

The details of the parameters are described in the evaporative cooling model in Section (6.3.3) of next chapter. In this section, only the outcomes are introduced.

Numerical Calculations

By applying the Mathematica software to solve Equations (5.1), (5.5), (5.6) and (5.7) numerically, the dynamics of the dimple-atoms can be evaluated. Here, the full power CODT is taken as an example for modeling.

After the loading process of the dimple formed by the full power CODT is finished, the wing-atoms mainly reside in the VODT, see Figure (5.5(E)). Therefore, in order to obtain information of the wing-atoms, the lifetime and TOF measurements of the atoms in the full power VODT are measured. By fitting the experimental results with the numerical models developed in Chapter 4, the time dependent number and temperature of the wing-atoms, N_w and T_w are inferred. The lifetime and TOF measurements of the wing-atoms and the fit results have already been shown in Figures (5.4).

The Mathematica software is used to obtain the optimized values of R_f, Γ_{BG}, F_2 and F_3. The best fit results are chosen by minimizing the value of the error sum between the atom number measurement and the numerical solution of Equation (5.6). After 1 s of trap holding time, the dynamics of the dimple-atoms are mainly dominated by background collisions. Until a trap holding time of 1 s, the dynamics of the atoms are dominated by the wing-atoms loading into the dimple, and elastic collisions as well as three-body collisions between the dimple-atoms. By fitting the data in different time intervals, the values of the fit parameters are obtained. The first step is to decide the value of Γ_{BG} by obtaining the best fit for the number of the atoms starting after the first second of the trap holding time. Then, the values of F_2 and F_3 are determined by fitting the number and temperature of the atoms in the time interval from 0 s to 1 s. Afterwards, the value of R_f is adjusted to obtain the least error sum of the time dependent atom number and the numerical calculation of Equation (5.6). The relevant lifetime and TOF measurements of the dimple-atoms have already been shown in Figure (5.6). The parameters for modeling can be deduced from the experimental conditions.

5.4.2 Results and Discussion

Figure (5.7) shows the fit results with different values of R_f where other fit parameters are kept constant. The black squares are the measured number of the dimple-atoms in the full power CODT. The green dashed curve shows the best fit results. The obtained fit parameters are as follows: R_f is 0.00001, Γ_{BG} is 0.56, F_2 is 0.048 and F_3 is 0.43. The orange dashed-dotted-dashed curve ($R_f = 0.0001$) and the blue solid curve ($R_f = 0$) present the fit results with different values of R_f. The three fit curves are scaled by a constant

factor of 1.3. As one can see from the figure, the wing-atoms mainly influence the dimple-atom number during the first 1.5 s of the trap holding time, independent on the amount of wing-atoms transferred into the dimple. As a consequence, the dynamics of the dimple-atoms could not be analyzed by the model.

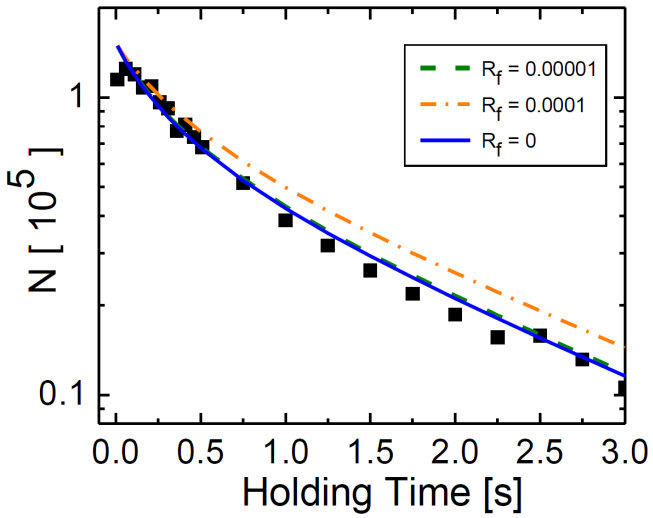

Figure 5.7: The fit results of the number of the dimple-atoms. The parameter $P_L = 1/2\Gamma_{el,v}$ is used for modeling. The experimental data is shown by black squares. The green dashed curve shows the best fit results ($R_f = 0.00001$). The orange dashed-dashed-dotted curve ($R_f = 0.0001$) and the blue solid curve ($R_f = 0$) present the fit results with different value of R_f. Besides the changes of R_f, other fit parameters are kept constant. All the fit results are scaled by a constant factor of 1.3. One can see that the model where the assumption of P_L is $1/2\Gamma_{el,w}$ cannot estimate the influences of the wing-atoms upon the dimple-atoms. A detailed discussion is given in the text.

One of the observations from the modeling results is that the dynamics of the dimple-atoms can be estimated if $P_L = \Gamma_{ev,w}$ is applied in the model. Figure (5.8) shows the best fit results for different assumptions of P_L in the model, see Equation (5.2). The black squares are the measured number of the dimple-atoms in the full power CODT. The green dashed curve and the red solid curve show the best fit results of the model while the applied P_L is defined by $1/2\,\Gamma_{el,w}$ or $\Gamma_{ev,w}$, respectively, where $\Gamma_{ev,w}$ is the evaporation rate of the wing-atoms[2]. One can see that the increase of the dimple-atoms is

[2]see Equation (2.21)

expected by the model using $P_L = \Gamma_{ev,w}$ (the red solid curve). The parameters of the fit curve are as follows: R_f is 0.014, Γ_{BG} is 0.5, F_2 is 0.06 and F_3 is 0.3. The fit result is not scaled. The parameter $\Gamma_{el,w}$ is the average collision rate of an atom locating at the center of the trap. Different from $\Gamma_{el,w}$, $\Gamma_{ev,w}$ is the collision rate of one atom in the high energy tail of a Boltzmann distribution. Comparing the two fit curves, it reveals that for the first few 10 ms, the dynamics of the dimple-atoms is mainly affected by the wing-atoms which have high energy. This observation is not fully understood yet.

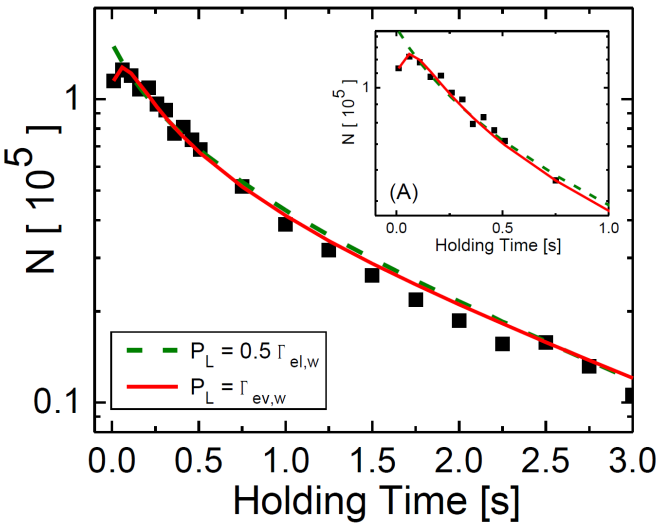

Figure 5.8: The fit results of the time dependent number of dimple-atoms. The experimental data is shown by black squares. The green dashed curve shows the best fit results while $P_L = 1/2\Gamma_{e1,w}$ is applied in the model. The red solid curve shows the best fit results while $P_L = \Gamma_{ev,w}$ is used for modeling. Plot (A) zooms in on the fit results. One can see that the model using $P_L = \Gamma_{ev,w}$ can fit the number of the dimple-atoms well. A further discussion is given in the text.

In order to study the influences of the wing-atoms upon the dimple-atoms, $P_L = \Gamma_{ev,w}$ is applied in the model for further discussion. The modeling results are plotted in Figures (5.9) and (5.10).

Figure (5.9) shows the experimental data and the fit results with different values of R_f where other fit parameters are kept constant. The parameter $P_L = \Gamma_{ev,w}$ is used in the model. The black squares show the experimental data that is the time dependent number of atoms in the dimple formed by the full power CODT. The red solid curve shows the best fit ($R_f = 0.014$).

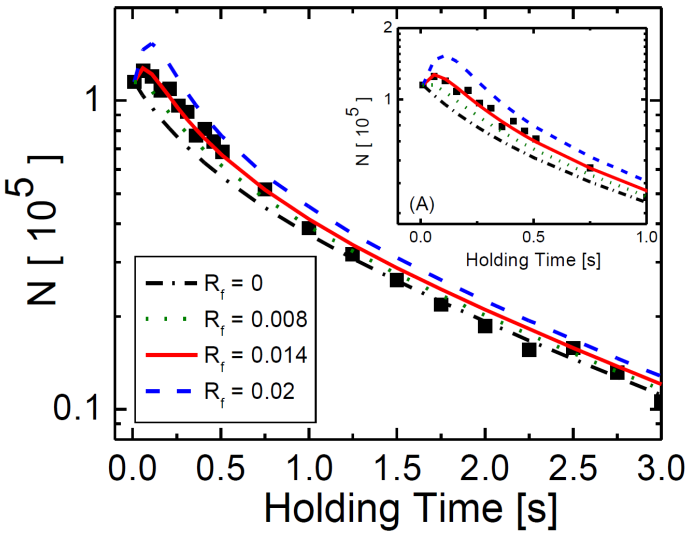

Figure 5.9: The fit results of the time dependent number of dimple-atoms with different values of R_f. The parameter $P_L = \Gamma_{ev,w}$ is applied in the model. The experimental data is shown by black squares. The red solid curve ($R_f = 0.014$) shows the best fit results. The black dash-dotted curve ($R_f = 0$), the blue dashed curve ($R_f = 0.02$) and the green dotted curve ($R_f = 0.008$) present the fit results with different values of R_f. The fit results are not scaled. According to the fit results, the wing-atoms loading into the dimple affect the dynamics of the dimple-atoms during the first few 100 ms. Plot (A) zooms in on the fit results. It clarifies the experimental observation of the increasing dimple-atom number during the first 60 ms as a result from the wing-atoms loading. A detailed discussion is given in the text.

The black dashed-dotted curve ($R_f = 0$), the blue dashed curve ($R_f = 0.02$) and the green dotted curve ($R_f = 0.008$) illustrate the results with different amounts of wing-atoms loading into the dimple. The fit results are not scaled. By comparing the four fit curves, it is apparent that the wing-atoms mainly affect the dynamics of the dimple-atoms during the first few 100 ms. Depending on the amount of the wing-atoms transferred in the dimple, the maximal dimple-atom number is different. With increasing number of wing-atoms loaded into the dimple (R_f is larger), the maximal dimple-atom number increases and the maximum is reached later. Plot (A) in Figure (5.9) zooms in on the fit results. It clarifies that increased number of the dimple-atoms during the first 60 ms is due to the wing-atoms loading into the dimple.

Figure (5.10) shows the fit results of the temporal evolution of the tem-

perature of the dimple-atoms with different values of R_f where other fit parameters are kept constant. As can be seen from the model, the temperature of the dimple-atoms is not affected by the wing-atoms loading into the dimple.

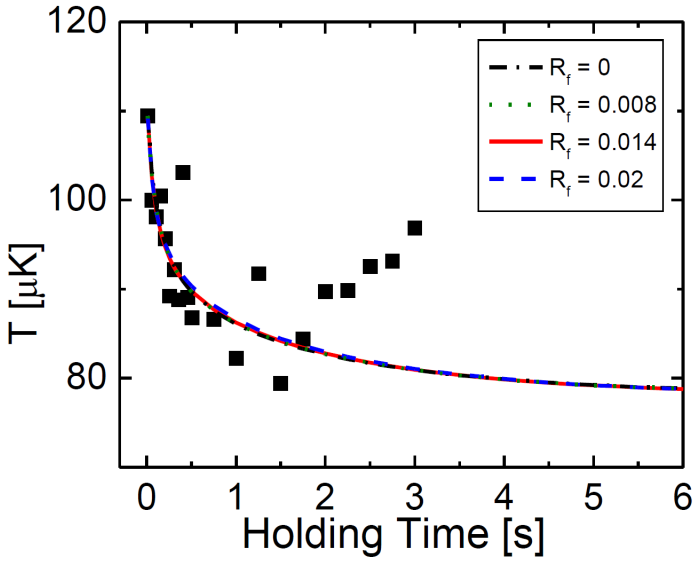

Figure 5.10: The fit results of the time dependent temperature of the dimple-atoms. The parameter $P_L = \Gamma_{ev,w}$ is used for modeling. The experimental data is shown by black squares. The red solid line($R_f = 0.014$) shows the best fit results. The black dash-dotted line ($R_f = 0$), the blue dashed line ($R_f = 0.02$) and the green dotted line ($R_f = 0.008$) present the fit results with different values of R_f. The fit curves are not scaled. Further details are given in the text.

In summary, although the model is strongly simplified, it provides a physical picture to understand some of the influences of the wing-atoms upon the dimple-atoms. The value of R_f (0.014) is approximately 70 times smaller than unity. It indicates that other losses of the wing-atoms may have to be considered for modeling. For example, collisions between one dimple-atom and one wing-atom which may cause the wing-atom to be lost from the trap and reduces the number of the atoms loading into the dimple, see Equation (5.1). Additionally, the dimple-atoms transferred into the wings due to collisions may have to be taken into account as one of the reasons which causes losses of the wing-atoms. These dimple-atoms increase the number of the wing-atoms and enhance collision losses of the wing-atoms due to an

increase of density. Therefore, it reduces the number of the wing-atoms. On the other hand, the values of F_2 (0.06) and F_3 (0.3) are also smaller than expected. This indicates that other losses of the dimple-atoms may need to be considered as well. On the other hand, one may take into account collisions between wing-atoms and dimple-atoms in the model to investigate the internal energy changes of dimple-atoms during the time in which wing-atoms are loading into the dimple.

Chapter 6

Evaporative Cooling

Many groups have successfully reached BEC of atoms with zero total angular momentum in the $^1S_0$ ground state such as the experiments with ^{40}Ca BEC [Kra09], ^{84}Sr BECs [Ste09, Eco09], and, ^{174}Yb and ^{170}Yb BECs [Tak03, Tak09]. To start evaporation, it is necessary to compare our experimental conditions with those of these BEC research groups in order to find a suitable strategy. When putting the chosen strategy into practice, evaporative cooling processes of the atoms in the dimple are possible to study. Moreover, according to experimental observations, an evaporation strategy can be designed to fit our case. The introduction of evaporative cooling strategies and the experimental observations are presented in the second section of this chapter. Experimentally, a further increase of the PSD could not be realized due to a fast loss of particles arising at the end of evaporation, independent of the specific protocol used. In order to investigate the experimental limits, a theoretical model has been developed which is based on the famous work by O. J. Luiten [Lui96]. The model and the modeling results are presented in the final section of this chapter.

6.1 Comparison of Experimental Parameters

Table (6.1) gives an overview of our experimental conditions and that of AEA BECs and ^{174}Yb BEC research. For our system the atoms in the dimple have a higher temperature and one order of magnitude less atoms compared to other research. In spite of this, similar experimental conditions for our system and the ^{174}Yb system indicate the possible feasibility for implementing the evaporative cooling strategy for ^{174}Yb atoms.

However, in contrast to ^{174}Yb atoms, ^{40}Ca atoms have a large ground state scattering length which may lead to serious loss and cause heating of

	^{174}**Yb**	^{40}**Ca**	^{84}**Sr**	^{84}**Sr**	^{40}**Ca**
Group	Kyoto	PTB	Innsbruck	Rice	Hamburg
Nr.(M)	10^7	10^8	2.5×10^7	1.6×10^7	3×10^8
T.(M)	$40\,\mu$K	$15\,\mu$K	$2.5\,\mu$K	$1\,\mu$K	$200\,\mu$K
U	$630\,\mu$K(H) $53\,\mu$K(V)	$180\,\mu$K(H) ——(V)	$110\,\mu$K(H) $37\,\mu$K(V)	$31\,\mu$K(D)	$372\,\mu$K(H) $615\,\mu$K(V)
Nr.(H)	1×10^6				2×10^6
I.T.(H)	$180\,\mu$K				$50\,\mu$K
Nr.(D)	2×10^5	5×10^6	$\approx10^6$	3×10^6	2×10^5
I.T.(D)		$20\,\mu$K	$\approx10\,\mu$K	$5\,\mu$K	$120\,\mu$K
S.L.	$\approx104\,a_0$	$\approx440\,a_0$	$\approx123\,a_0$	$\approx123\,a_0$	$\approx440\,a_0$
Ref.	[Tak03]	[Kra09]	[Ste09]	[Eco09]	

Table 6.1: Comparison of experimental parameters. Nr.: atom number. T.: temperature of the trapped atoms. I.T.: initial temperature of the atoms. U: the trap depth. D: regarding to the dimple. H: regarding to the HODT. V: regarding to the VODT. M: regarding to the MOT. S.L.: the scattering length. a_0: Bohr radius. Ref.: references

trapped atoms during evaporation, especially for situations with a narrow dimple size, as applied for ^{174}Yb atoms. Therefore, besides taking the evaporative cooling strategy for ^{174}Yb atoms into practice, the evaporative cooling strategy for ^{40}Ca atoms developed by the PTB is applied. These experimental observations can help to study evaporative processes of the atoms and develop the optimal evaporative steps for our case.

6.2 Evaporative Cooling Strategies

6.2.1 Evaporative Cooling Strategy for ^{174}Yb Atoms

Description

The evaporative cooling strategy for ^{174}Yb atoms is efficient [Tak03]. The configuration of the CODT involves the use of two ODTs in the horizontal and vertical planes. The foci of the two ODTs intersect. The HODT has a large trap volume and the VODT has a shallow trap depth. By gradually ramping down the depth of the HODT and keeping the depth of the VODT constant, an evaporative process can be obtained.

The principles behind the CODT setup are the following: Firstly, this configuration enables hot atoms to be released easily from the trap. The potential of the VODT is modified by the gravitational potential which lets

hot atoms escape easily from the tilted potential, and hence the rest of the cold atoms can rethermalize in the trap. Secondly, the shallow depth of the VODT is designed to reduce the number of atoms in the wings. Atoms trapped in the wings are likely to collide with the atoms trapped in the dimple. This results in heating of the atoms in the dimple. Thus, the VODT is not able to support atoms against gravity in order to eliminate undesired collisions. Thirdly, the VODT provides extra confinement at the end of the evaporative cooling process which removes the drawback of a single beam ODT configuration for forced evaporation. Consequently, the HODT with a large trap volume is used as a reservoir for trapping a large amount of atoms and the VODT with a shallow depth provides advantageous conditions for evaporation. The details of this strategy are described in Ref. [Tak09].

Experimental Observations

The results obtained when following the strategy for ^{174}Yb atoms are presented in Figure (6.1). The circularly polarized HODT at 1064 nm has a power of 13.5 W and a beam waist radius of 31 μm which corresponds to a trap depth of 372 μK. The linearly polarized VODT at 532 nm has a power of 451 mW and a beam radius of 35.9 μm in the dimple region which corresponds to a trap depth of 17 μK. The VODT cannot support atoms against gravity and its beam size is adjusted by shifting its focus 3 mm away from the dimple region. After the loading process is finished (i.e., we obtain a maximum amount of atoms in the HODT), forced evaporation is carried out by decreasing the depth of the HODT in four linear ramps. In each ramp, the trap depth is lowered by a factor of three. During the evaporation, the depth of the VODT is kept constant.

Figure (6.1) plots the values of the peak density n, the elastic collision rate Γ_{el}, the truncation parameter η and the PSD of the trapped atoms at each ramp. These parameters are defined in the same way as in Section (2.3), where the atoms are assumed to be in a three-dimensional harmonic potential. Initially, there are 1×10^6 atoms at a temperature of 45 μK loaded into the HODT. The corresponding PSD is 2×10^{-4}. During the first ramping process, the atoms start to accumulate in the dimple. After 538 ms of the evaporation, there are about 1.5×10^4 atoms in the dimple with a temperature of 3.8 μK. The resulting PSD is 2×10^{-3}. The parameters of each ramp are optimized experimentally by obtaining a maximum peak density of the trapped atoms.

Experimentally, the temperature of the atoms can be reduced even more by reducing the depth of the HODT. However, this is accompanied by serious atom loss. Accordingly, the PSD of the atoms does not increase. One ex-

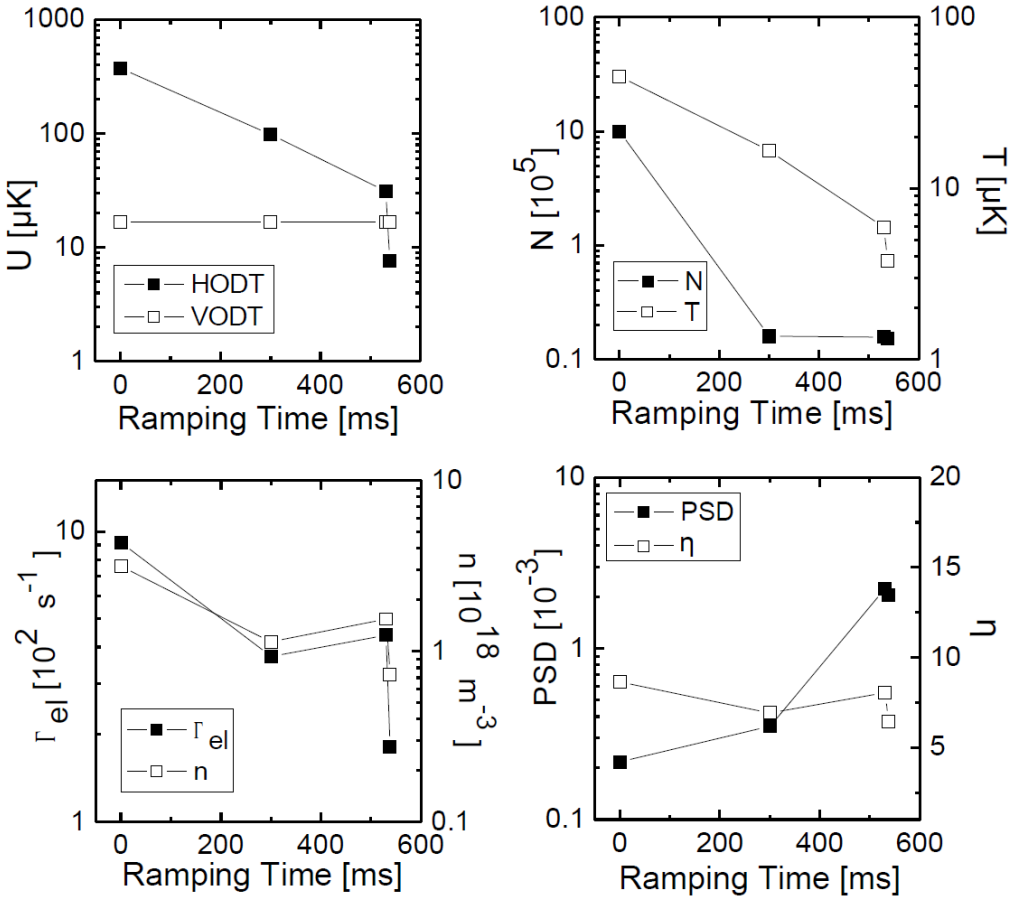

Figure 6.1: The results of the forced evaporation following the strategy for ^{174}Yb atoms [Tak03]. The evaporation is applied by ramping down the depth of the HODT in four linear ramps in 538 ms. During the evaporation, the depth of the VODT is kept constant. The trap depth, number, temperature, elastic collision rate, PSD, peak density and truncation parameter are represented by U, N, T, Γ_{el}, PSD, n and η, respectively. Notice, the lines between the data points are only to guide the eye. The dimple is assumed to be a three-dimensional harmonic potential. The details are described in the text.

perimental observation is that if the depth of the VODT and the HODT are reduced simultaneously, the PSD of the atoms is increased. The results are shown in Figure (6.2). All experimental parameters of the CODT here are the same as in Figure (6.1). But, the depths of the two ODTs are ramped down simultaneously by the same factor in the final ramping step. After

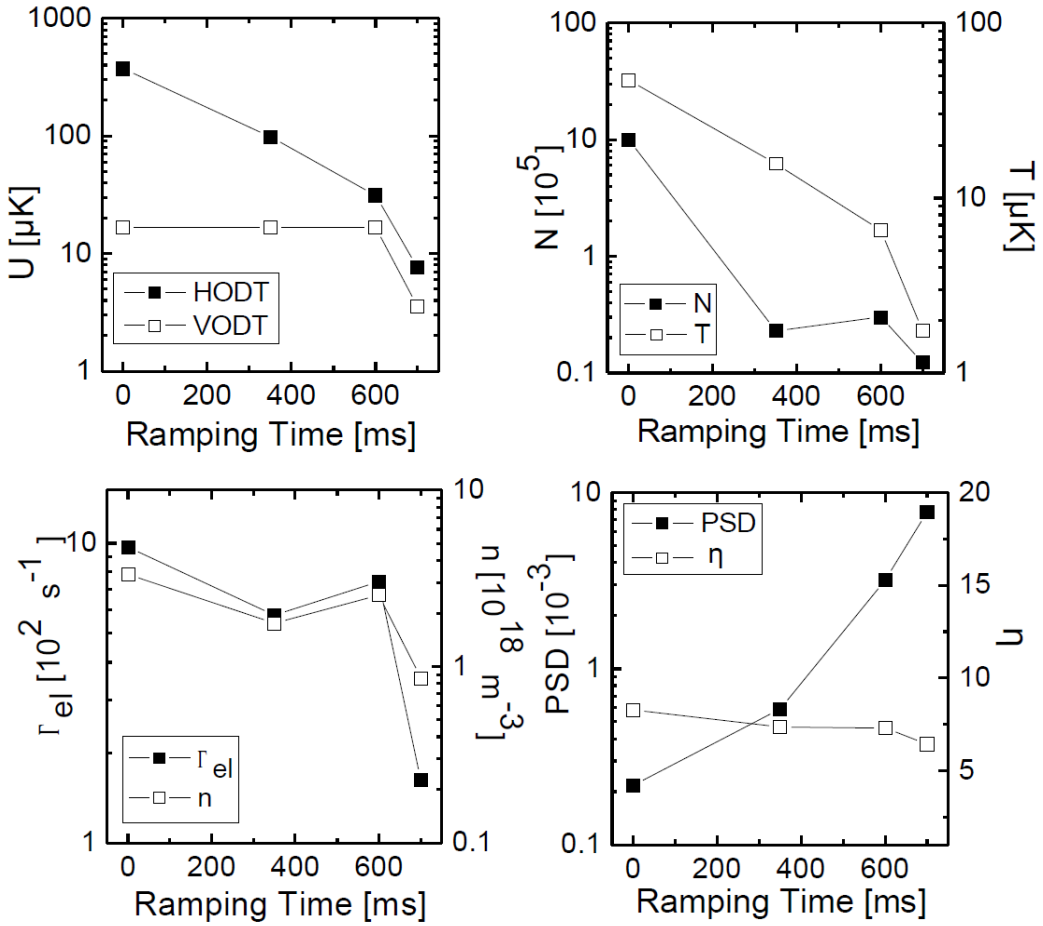

Figure 6.2: The results of the forced evaporation process following the strategy for ^{174}Yb atoms, excluding the final evaporative step. The forced evaporation is implemented for 700 ms. During the first three ramps, the depth of the VODT is kept constant and the depth of the HODT is reduced. For the final evaporative step, the depth of the VODT and the HODT are ramped down simultaneously. All parameters used in the figure are defined in the same way as in Figure (6.1). Notice, the lines between the data points are only to guide the eye. Further details are given in the text.

700 ms of forced evaporation, there are 1.2×10^4 atoms in the dimple at a temperature of 1.75 μK. The resulting PSD is about 8×10^{-3} which is four times larger than that shown in Figure (6.1).

Discussion

Experimental observations indicate that the PSD of the trapped atoms cannot be further increased at the end of the evaporation sequence following the strategy for ^{174}Yb atoms, see Figures (6.1) and (6.2). Moreover, the peak density decreases during the evaporation sequence excluding the first data point which only indicates the atoms loaded into the HODT.

On the other hand, since atoms keep loading into the dimple during the evaporation, the characteristic quantities of this evaporation process cannot be estimated, see Section (2.3.4).

In order to understand the limitations of evaporation, various beam sizes of the VODT in the dimple region were used for studying evaporation following the strategy for Yb atoms. Compared to the parameters in Figure (6.1), the results show that the temperature of the atoms is higher while a narrower beam size of the VODT is applied at the dimple region. Moreover, the duration of evaporation is shorter while the depth of the VODT is deeper. These observations indicate that density dependent losses may limit the evaporation process.

6.2.2 Evaporative Cooling Strategy for ^{40}Ca Atoms

Description

The evaporative cooling strategy developed by the ^{40}Ca research group of the PTB focuses on reducing the three-body collisional losses. The reason is that ^{40}Ca atoms have a large scattering length in the ground state ($\approx 440\,a_0$ [Kra09]) which may lead to serious density dependent losses during evaporation. A CODT setup is applied which basically follows the experimental configuration for ^{174}Yb atoms [Tak09]. To eliminate large three-body losses, the individual CODT beam waists are comparatively broad. The HODT is designed mainly to trap cold atoms. The designed VODT reduces density dependent losses, eliminates undesired collisions between atoms trapped in the wings and in the dimple and provides an extra confining force at the end of the evaporation process.

Different from the evaporation strategy for Yb atoms, the evaporation process is done by gradually reducing the depth of the traps in four linear ramps. For the first step, the depth of the VODT beam is kept constant and the depth of the HODT beam is reduced by a factor of three. For the other steps, the depths of the VODT and the HODT are ramped down simultaneously by the same factor in linear ramps. The details of the strategy are described in [Kra09].

Experimental Observations

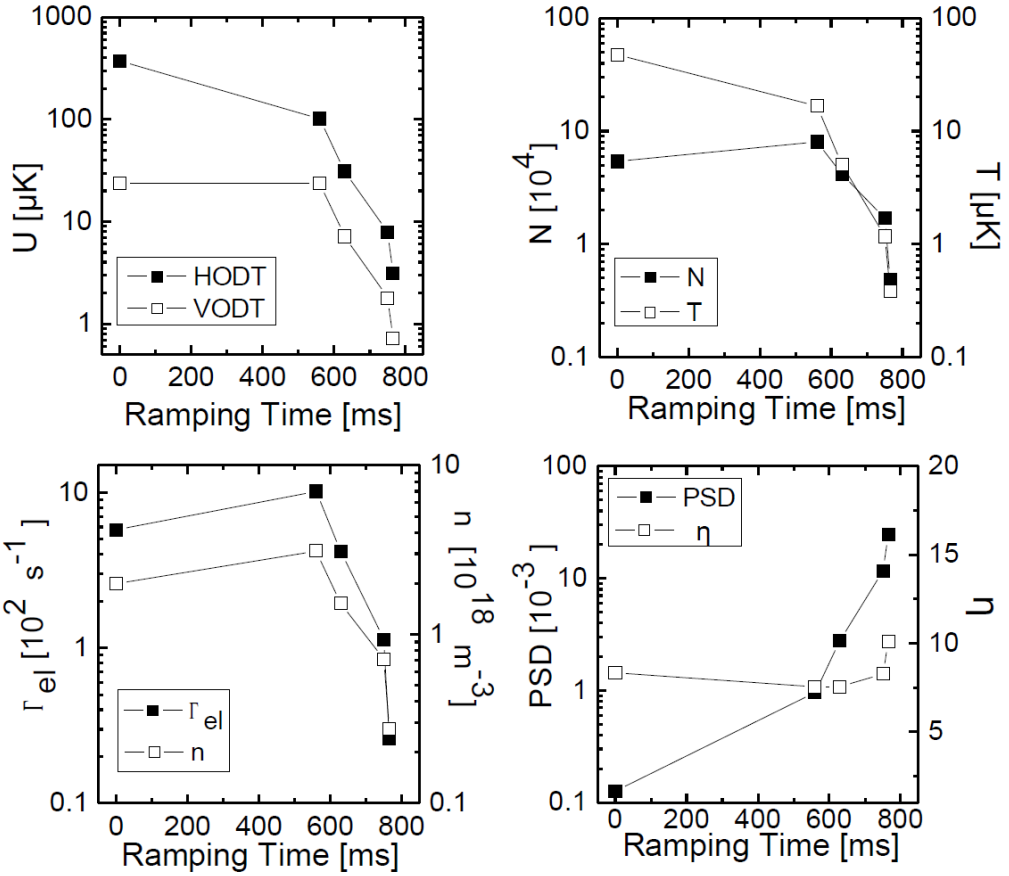

Figure 6.3: The results of the evaporative cooling process following the strategy for ^{40}Ca atoms [Kra09]. The beam radii of the HODT and the VODT at the dimple are 31 μm and 80 μm, respectively. The first evaporative cooling step keeps the depth of the VODT constant and ramps down the depth of the HODT. For rest of the cooling steps, the depths of the HODT and the VODT are ramped down together by the same factors. The parameters used in the figure are defined in the same way as in the last section. Notice, the lines between the data points are only to guide the eye. The details are described in the text.

Figure (6.3) shows the experimental results. The calculated values in the figure and the parameters of the HODT are defined in the same way as in the last section. The linearly polarized VODT at 532 nm with a power level of 3.22 W and a beam size of 80 μm at the dimple region produces a trap depth

of 24 μK. The VODT cannot trap atoms against gravity and its beam size at the dimple region is adjusted by shifting the focus away from the dimple by 7.3 mm. The evaporation is performed by reducing the depths in four linear ramps following the experimental steps for ^{40}Ca atoms, published by the PTB.

Initially, there are about 5.4×10^4 atoms trapped in the dimple at a temperature of about 47 μK. The resulting PSD is about 1.3×10^{-4}. During the first ramping step, the atoms start to accumulate in the dimple. After about 765 ms of the evaporative cooling process, there are about 4.8×10^3 atoms in the dimple with a temperature of about 0.38 μK. The corresponding PSD is 2.5×10^{-2}.

Discussion

Implementing the strategy for ^{40}Ca atoms from the PTB, the PSD of the trapped atoms is increased by almost three orders of magnitude after the forced evaporation. α_{EV} and γ_{EV} in Figures (6.4) and (6.5) have been determined from fits to the data and the values are larger than 1, which excludes the first data point because the atoms in the wings of the CODT still keep loading into the dimple, see Section (2.3.4). Thus, this forced evaporation is in the regime of runaway evaporation.

Comparing the experimental conditions of the ^{40}Ca research group in the PTB and that of our system, it becomes clear that for our case the low initial PSD of the atoms and the rapidly reducing density of atoms at the end of evaporative cooling cancel the possibility of reaching a quantum degenerate gas by implementing this strategy. Besides, a much shorter duration of the evaporation for our case also implies some experimental limitations in the experiment.

6.2.3 Evaporative Cooling Strategy of Our Group

Description

The results of the previous sections indicate, possible density dependent losses, the low initial PSD of the atoms and a rapidly reducing density of atoms during evaporative cooling cancel the possibility to reach the BEC. To eliminate these factors, a new strategy has been developed.

The trap configuration basically follows the design for ^{174}Yb atoms [Tak09]. In order to have advantageous starting conditions for evaporation, the initial depths of the VODT and the HODT used for evaporation are comparable. Therefore, the system is able to trap a large amount of atoms in the dimple.

However, the high density of the trapped ^{40}Ca atoms leads to serious density dependent losses due to three-body collisions. To eliminate this drawback, at the beginning of evaporation, the depths of the ODTs are ramped down simultaneously by large ramp factors in very short time intervals. These rapid ramp steps should reduce the density of trapped atoms which increase the collision time, and keep the PSD of the atom constant. Time scales can be estimated by calculating the three-body collision half time, see Equation (2.27). After the density of the trapped atoms is lower than $10^{20}\,\mathrm{m}^{-3}$, the losses caused by three-body collisions do not play such an important role. Thus, the depths of the ODTs should ramp down in small steps and the durations of evaporative cooling should be long enough for sufficient re-thermalization of the trapped atoms.

Experimental Observations

Figure (6.4) shows the first set of the experimental results. The calculated values and the parameters of the HODT are defined in the same way as in the previous sections. The linearly polarized VODT at 532 nm with a power of approximately 1.77 W and a beam radius of 15.8 μm at the dimple region produces a trap depth of approximately 338 μK. The initial depth of the VODT is determined by experimental observations. The evaporative process is implemented by reducing the well depths in several linear ramps in 281.5 ms simultaneously. The parameters of each ramp step are optimized experimentally by obtaining the most cold and dense atomic ensemble.

In the beginning there are about 1.3×10^5 atoms at a temperature of 67 μK in the dimple. The obtained peak density reaches a level of $10^{20}\,\mathrm{m}^{-3}$. The resulting PSD is 3.7×10^{-3}. After reducing the depths of the ODTs in five linear ramps simultaneously, there are 4.4×10^3 atoms at a temperature of 0.57 μK in the dimple. The PSD is 0.146. Consequently, the PSD of the trapped atoms has been successfully increased by two orders of magnitude compared to the results shown in the previous two sections. However, despite this, the unexpectedly short ramping duration of the evaporation process impedes thermalization of the trapped atoms and the rapidly reducing density of the atoms reduces a chance of achieving a BEC.

In order to understand the limitations, different beam sizes of the VODT at the dimple are investigated. The beam size of the VODT is changed by shifting its focus away from the dimple region. The experimental results are shown in Figure (6.5). The parameters of the HODT are the same as in the previous sections. The linearly polarized VODT at 532 nm with a power of approximately 1.93 W and a beam radius of 20 μm at the dimple region produces a trap depth of about 230 μK. The initial beam power of

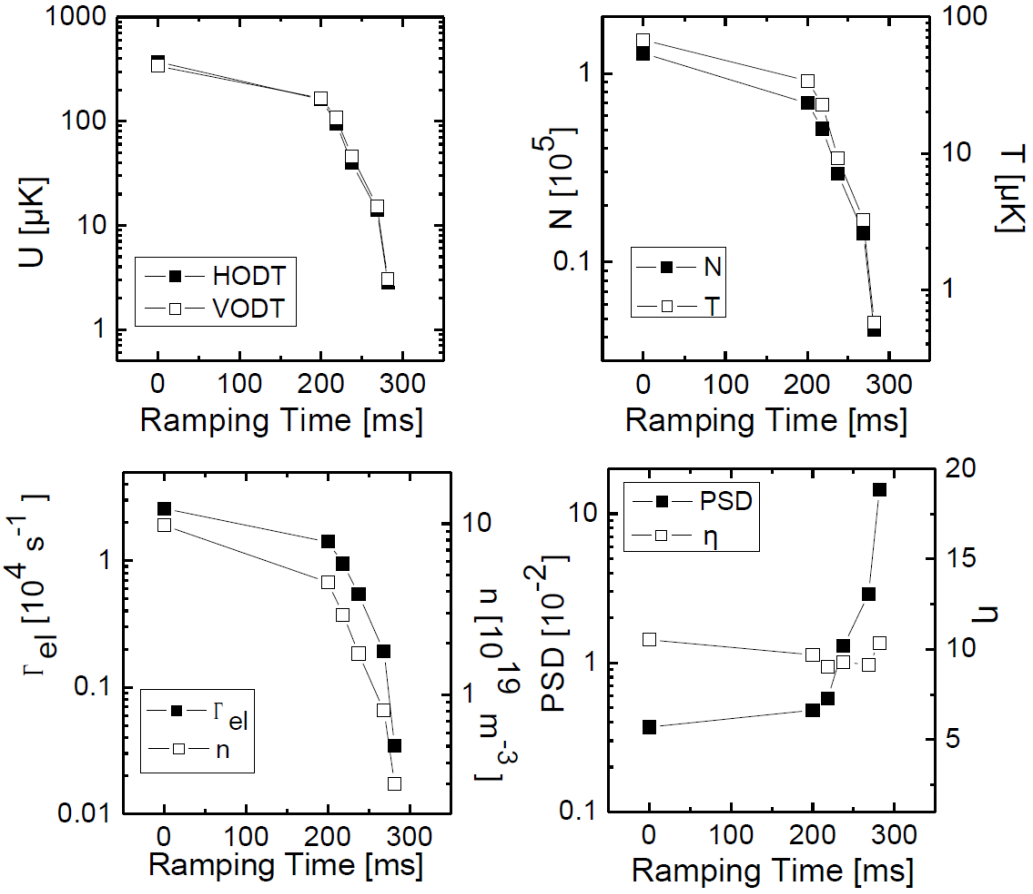

Figure 6.4: The results of the evaporative cooling process using the strategy developed in our group. The beam radii of the HODT and the VODT at the dimple region are 31 μm and 15.8 μm, respectively. The evaporative cooling process is implemented by reducing the well depths in five linear ramps in 281 ms. The parameters and guiding lines applied in the figure are defined in the same way as in the previous sections. A detailed description of the results is discussed in the text.

the VODT is chosen by obtaining the maximal amount of the atoms trapped in the dimple. The evaporative process is implemented by reducing the well depths simultaneously in 423 ms. The duration of each ramp step is optimized experimentally. At the beginning there are about 1×10^5 atoms at a temperature of 65 μK in the dimple. The obtained peak density is decreased to the level of $10^{19}\,\mathrm{m}^{-3}$. The resulting PSD is 1×10^{-3}. After reducing the depth of the trap in seven ramps, there are 3×10^3 atoms at a temperature

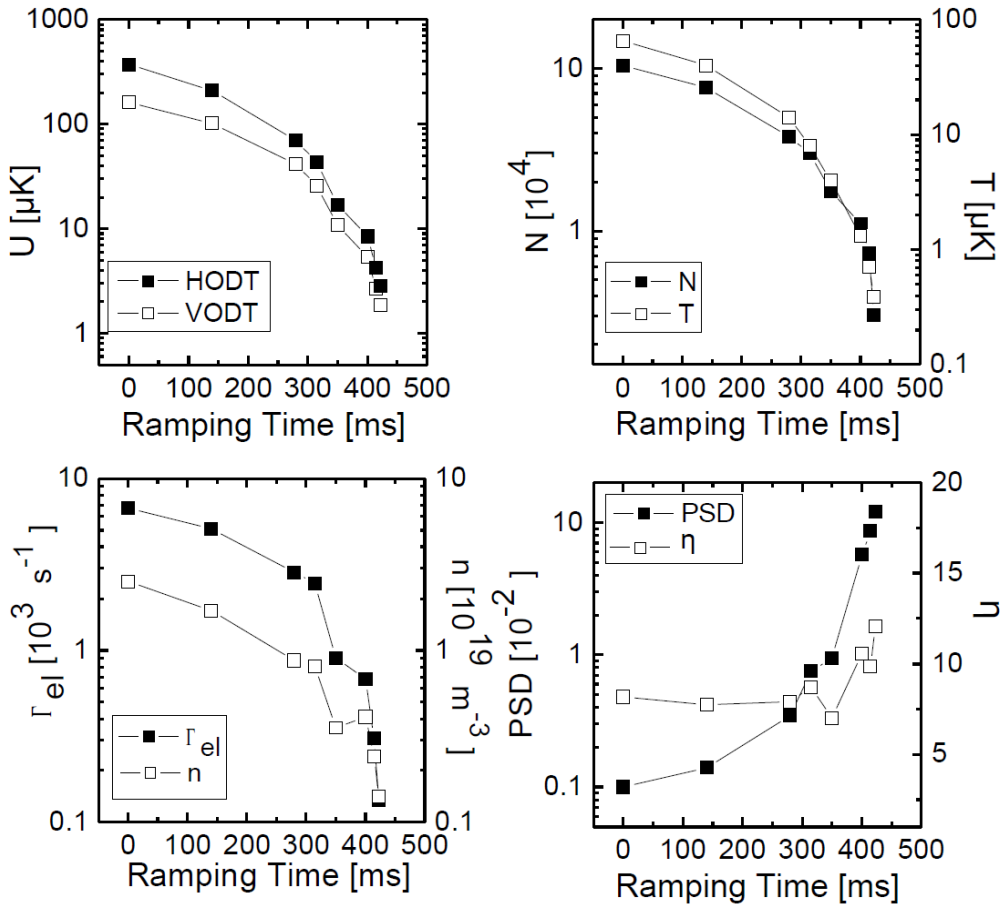

Figure 6.5: The results of the evaporative cooling process using the strategy developed in our group. The beam radii of the HODT and the VODT at the dimple region are 31 μm and 20 μm, respectively. The evaporative cooling process is implemented by ramping down the well depths simultaneously in 423 ms. The parameters and the guiding lines used in the figure follow definitions used in the previous sections. A detailed description of the results is given in the text.

of 0.39 μK in the dimple. The calculated PSD is 0.121.

Discussion

α_{EV} and γ_{EV} in Figures (6.4) and (6.5) have been determined from fits to the data and the values are larger than 1. Thus, this forced evaporation is in the regime of run away evaporation. Until now, the highest PSD of the atoms

in the dimple was 0.146, obtained using the strategy developed in our group. According to the experimental results shown in Figure (6.4), a BEC with 2000 atoms in the dimple could be reached by reducing the depth of the trap further. Unfortunately, the characteristics of the atoms are not detectable due to restrictions of the imaging system by the shot noise level, see Section (2.5.3).

Obviously, unexpectedly short durations and a decreasing atomic density during the evaporation implies experimental limitations. These observations have already been discussed in the previous sections. Here, to study the limits, different beam sizes of the VODT at the dimple region are applied for evaporation. It is observed that a larger size of the VODT results in a longer duration of the evaporation process. However, on the contrary, the PSD of the trapped atoms become smaller for a larger size of the VODT.

6.2.4 Summary

In conclusion, an evaporation duration which is too short and a decreasing density of the atoms during evaporation removes the possibility of reaching BECs. Notice, one can see that, independent of the special protocol used, the peak density of the atoms reduces rapidly at the end of the evaporation, i.e., in the case of a shallow trap. Various volumes and sizes of the dimple have been investigated for evaporation in order to reduce the limits which may arise due to density dependent losses or laser induced losses and heating. However, inevitably a rapidly decreasing density of the atoms indicates that other experimental limits have to be taken into account. Thus, a theoretical model is applied in the next section for evaporative dynamics studies. The model focuses on investigating the experimental limits which cause atom losses at the end of evaporation.

6.3 Modeling Evaporation

The model applied here mainly follows the well-known model by O. J. Luiten [Lui96] instead of the one developed by K. M. O´Hara [O01]. The work by O. J. Luiten [Lui96] applies a truncated Boltzmann distribution to the atomic energy to describe the thermodynamical properties of the trapped atoms. Due to the assumption of sufficient ergodicity, all thermodynamical parameters can be described by the truncation parameter $\eta_t = U_t/(k_B T_t)$ where U_t is the trap depth and the index t emphasizes that the parameters are time dependent. It provides a simple method to develop the model. Although the model developed by K. M. O´Hara [O01] provides a simple scaling law

for understanding the evaporation process and estimating the conditions for achieving a quantum degenerate gas state, it only takes into account atom losses due to background collisions and elastic collisions without considering other losses during the evaporative cooling process. Thus, it can not assist us in investigating the experimental limitations.

The highest PSD for the atoms is reached by applying the strategy developed in our group. Therefore, the data points shown in Figure (6.4) have been used for modeling the evaporation process when considering the actually time dependent trap depth.

6.3.1 Basic Assumptions

In the following analysis we assume:
(1) sufficient ergodicity. The distribution of atoms only depends on their total energy. This allows the use of simple analytical expressions for the elastic collision rate and other physical parameters.
(2) s-wave approximation. For the low temperatures considered here, elastic collisions are isotropic, i.e., in the s-wave regime, and are characterized by the total elastic scattering cross section σ_t.
(3) every atom with a total energy E larger than a truncation energy ϵ_t is removed from the trap before it collides with other atoms. In the model, ϵ_t is equal to the time dependent trap depth U_t.
(4) the system is in the quasi-equilibrium state. Thus all thermodynamic parameters may still be defined by the temperature.
(5) the truncation parameter η_t has to be much larger than one. For a large value of η_t, the energy distribution of the trapped atomic ensemble is close to a Boltzmann distribution with a $E = 3k_BT$ in a three-dimensional harmonic trap [Ket96].

The third assumption is only valid while atoms are in the Knudsen regime. It means the collisional mean free path of the atoms is much larger than the size of the gas cloud, i.e., the collision rate of the atoms should be much smaller than the trap frequency. However, as the data shown in Figure (6.4) indicates, the atoms are not in the collisionless regime for evaporation. Accordingly, atoms with an energy higher than U_t cannot escape from the trap without colliding with other atoms. This means that the efficiency of the evaporation process is reduced. Therefore, notice that the fit results only provide knowledge of the upper limit of the rate of the evaporation.

In the model, the applied truncation energy is the same as U_t because gravity is not considered. i.e., the geometrical trap configuration is not considered, cf. the third assumption. The dimple for modeling is simply approximated by a three-dimensional harmonic trap. This is a very crude

approximation but it has the advantage that analytic expressions for all the below parameters can be obtained easily.

The Ph.D. thesis of Murray D. Barrertt [Bar02] provides a good discussion of the basic assumptions of the evaporative cooling model.

6.3.2 Heating and Losses

Before introducing the model, I briefly introduce the mechanisms which may cause heating and loss of atoms during the evaporation process in the system.

Photon Scattering: The major source of photon scattering heating and losses is caused by the trap laser itself which was introduced in Section (2.2.1). Comparing the two ODTs applied in the system, the full power VODT has a higher photon scattering rate of $9\,\mathrm{s}^{-1}$. One of the conclusions from of the numerical models in Chapter 4 is that losses and heating of the atoms caused by the photons of the full power VODT only appear after 2 s of trap holding time. Therefore, this factor cannot account for limiting the evaporation process.

The other source of photon scattering heating and losses is because of on-resonance stray light. The stray light with very small amounts of optical power ($\approx 10^{-5}$ of the saturation parameter) can lead to serious losses and cause heating of the trapped atoms in the dimple. Thus, the residual on-resonance stray light should be filtered out or reduced to a minimum during the experiment. For the experimental system, the light at 423 nm is close to the resonance with the trapped atoms in the $^1S_0$ ODTs. Therefore, this factor is considered to be one of the causes of unexpected atom losses during evaporation especially since the effects of the stray light becomes more important while the trap depth is reduced. The details are described in the following section.

Density Dependent Losses and Heating: This factor has been introduced in Section (2.4) mainly for an atomic ensemble which has a high density. Three-body collisions may cause serious losses and lead to heating of the atoms. On the other hand, elastic collisions provide a cooling mechanism for the atoms.

Changes of Potential : If the trap potential is changed, some atoms are lost from the trap due to spilling and the remaining atoms may change their energy [Pin98].

Laser Induced Losses and Heating: The discussions of laser induced heating and losses is presented by the Refs. [Sav97, Geh98]. When the frequency scale of the pointing and the intensity fluctuation of the ODT beam is close to its trap frequency or the second harmonic of the trap frequency, these fluctuations will lead to heating and losses of the atoms trapped in the

ODT. The intensity fluctuation leads to an exponential heating of the trapped atoms which depends on their average energy. Contrarily, the pointing fluctuation causes a constant heating of the trapped atoms, i.e., independent of their average energy. Both laser fluctuations result in exponential atom losses. Assuming the system has a constant heating rate due to the laser fluctuations, the values decrease while the trap depth is reduced, that can be seen from Equations (12) and (16) of Ref. [Sav97]. Since the following model mainly focuses on investigating atom losses at the end of the evaporation, instabilities of the trap lasers are neglected for modeling.

Characteristics of ODT Laser Beams: The foci of the HODT and the VODT laser beams shift in position during the evaporation for various reasons.

For the HODT laser beam, the focus gradually shifts away from the dimple region while the power of the HODT beam decreases. The beam radius at the dimple changes from 31 μm to 35.54 μm when the power of the beam changes from the full power to 20 % of the maximum. The position of the focus stops changing while the power of the beam is decreased when already below 20 % of the maximum power. The change in the HODT beam radius at the dimple region is taken into account for all evaporative cooling data shown in the previous sections.

The radius of the HODT beam at the dimple region is estimated using Gaussian optics, taking into account the shifting distance of its focus and the optical elements behind the AOM. The optical setup is shown in Figure (3.7). Here it is assumed that the beam shift is due to thermal effects from the 50 mm achromatic focusing lens right behind the AOM. The position shift of the focus can be observed by the CCD chip at position 2, see Figure (3.2(B)). As a reference, the highest optical density of the trapped atoms is at the trap center, the shift of the focus is shown in Figure (6.6). The focus has been observed to shift 2 mm away from the dimple while the power of the beam is reduced to 20 %, where the distance is calculated using the pixel size of CCD chip. Moreover, for cross checking the focal position shift, the final focusing lens in the beam path has been shifted away from the camera to compensate the focal position change with respect to the beam power.

Although the size of the HODT beam at the dimple gets larger while reducing the power, it changes gradually. i.e., the time scale is much slower than the time scale of the trap frequency. On the other hand, the power dependent beam size change of the HODT affects expectantly only the atomic dynamics at the beginning of evaporation while the power of the HODT is larger than 20% of the full power. For those two reasons, the instability of the HODT beam does not account for limiting evaporation in the following model, which focuses on investigating the reason for fast atom losses at the

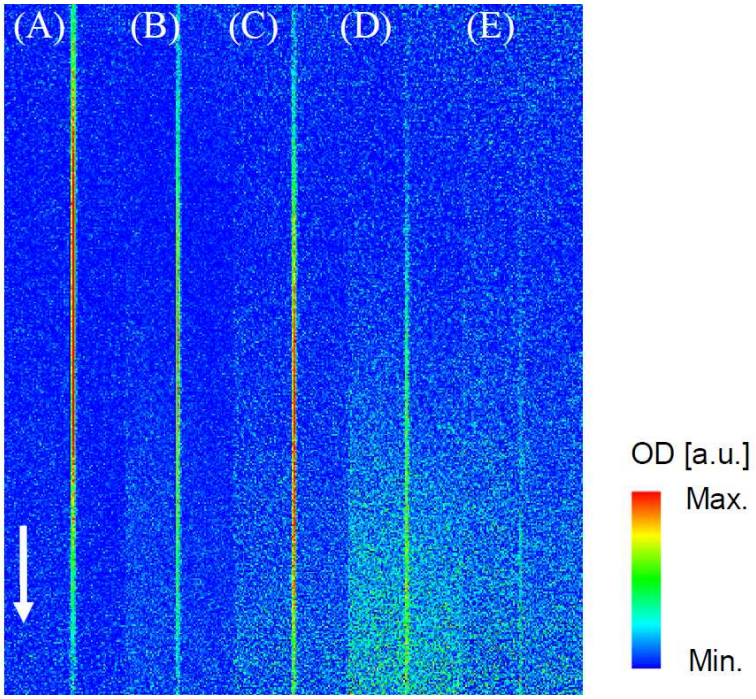

Figure 6.6: Images of the HODT at different optical power levels. (A), (B), (C), (D) and (E) are taken for 100 %, 80 %, 60 %, 40 % and 20 % of the full beam power respectively. As a reference, the highest optical density of the image is at the center of the trap. The focus of the beam shifts depending on the beam power which can be observed. Changing the power of the beam from 100 % to 20 %, the focus of the beam is shifted by 2 mm along the beam propogation direction. The arrow shows the direction towards to the camera. The images are taken by the CCD chip at position 2, see Figure (3.2(B)). The results are described in the text.

end of the evaporation. This instability can be solved by redesigning the telescope behind the AOM. i.e., the focusing lens can be placed at a position further away from the AOM to reduce thermal effects.

For the VODT laser beam, the focus of the full power VODT shifts from image to image, which is shown in Figure (6.7). In order to study the reason causing the focal shift and the beam size change, the beam is strongly focused by a lens with a short focal length after its power is attenuated by two mirrors with high reflection optical coating at 532 nm. The size of the beam at the focal position can be measured by a camera beam profiler[1]. The

[1]BC106UV, BC106-VIS, Thorlabs Inc.

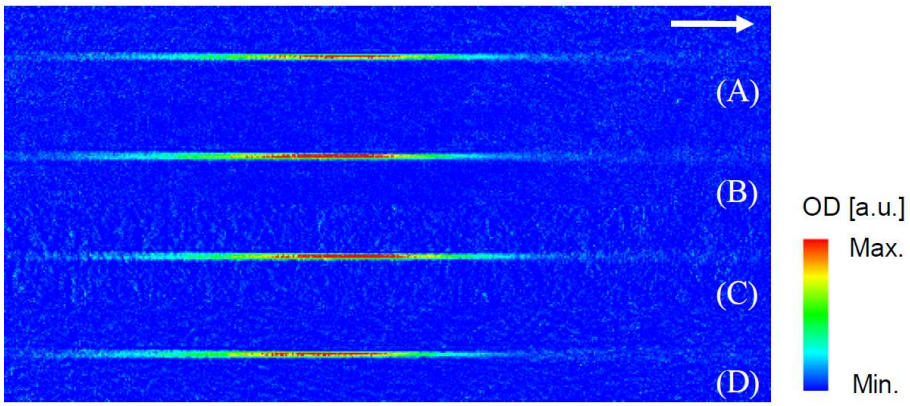

Figure 6.7: Images of the focal shift of the full power VODT laser beam. These images are taken by the CCD chip at position 2, see Figure (3.2(B)). The focus of the VODT shifts randomly along the axis of gravity. The arrow shows the direction of gravity. The details are described in the text.

beam is guided out from the main beam path at two locations. The first position is behind the Verdi laser and the second position is behind the AOM. Consequently, the size of the beam changes by approximately 15 % with the same time scale at both locations. Notice, the result cannot distinguish between a focal position shift and a beam size change.

Accordingly, the instability of the VODT is from the Verdi laser itself and thus it cannot be prevented. We believe it to be coming from a thermal instability of the crystal in the laser cavity. Since the model focuses on investigating losses at the end of evaporation, the instability of the VODT beam is not taken into account in the following modeling, see the discussion of laser induced losses and heating.

6.3.3 Parameters

Under the assumption of sufficient ergodicity, all relevant information can be expressed as a function of E. To keep the calculations simple, all parameters are expressed by η_t.

Evaporation : As described in Sections (2.3) and (2.4), the total number of atoms lost per time unit due to evaporation $\dot{N}_{ev}$ can be expressed as

$$\dot{N}_{ev} \;=\; \Gamma_{ev}\, N \;=\; \sigma_t \,\frac{\overline{\omega}^3\, m}{4\,\pi^2}\,\frac{{\eta_t}^2}{U_t}\,\exp(-\eta_t)\, N^2\,. \tag{6.1}$$

Following the discussion in Ref. [Yan09], in the high - η_t approximation,

the average energy loss per evaporated atom $\overline{E_{ev}}$ is given by

$$\overline{E_{ev}} \;=\; U_t + (\frac{\eta_t - 5}{\eta_t - 4})\,\frac{U_t}{\eta_t}\,. \tag{6.2}$$

Thus, the rate of the total energy change due to evaporation $\dot{E}_{ev}$ is

$$\dot{E}_{ev} \;=\; \overline{E_{ev}}\,\dot{N}_{ev} \;=\; \sigma_t\,\frac{\overline{\omega}^3\,m}{4\,\pi^2}\,(\frac{{\eta_t}^3 \;-\; 3\,{\eta_t}^2 \;-\; 5\,\eta_t}{\eta_t \;-\; 4})\,\exp(-\eta_t)\,N^2 \tag{6.3}$$

here m is the mass of an atom, N is the number of atoms trapped in the dimple and $\overline{\omega}$ is the mean geometric trap frequency, σ_t is the elastic scattering cross section with energy dependence given by Equation (2.20) and Γ_{ev} is the evaporative cooling rate of the atom given by Equation (2.21).

Three-Body Collisions : Following Section (2.4), the total number of atoms lost per time unit due to three-body collisions $\dot{N}_{3B}$ is given by

$$\dot{N}_{3B} \;=\; F_{3B}\,\Gamma_{3B}\,N \;=\; \frac{F_{3B}\,L_{3B}}{\sqrt{27}}\,\frac{\overline{\omega}^6\,m^3}{8\,\pi^3}\,(\frac{\eta_t}{U_t})^3\,N^3 \tag{6.4}$$

where Γ_{3B} is the three-body collision rate given by Equation (2.26). L_{3B} is the three-body loss coefficient, see Section (2.4), and its value is given by Ref. [Kra09]. F_{3B} is a fitting parameter to obtain the best fit results since the value of Γ_{ev} is not scaled for modeling.

The mean potential energy of an atom undergoing a three-body process can be calculated by integrating over a thermal distribution with weighting proportional to n^3, which yields $1/2\,k_BT$, where n is the peak density of the atoms. As the ensemble average energy is $3/2\,k_BT$, for each lost atom an excess energy of $1\,k_BT$ remains in the system [Web03a]. Consequently, the rate of the total energy change due to a three-body recombination process $\dot{E}_{3B}$ is

$$\dot{E}_{3B} \;=\; \frac{U_t}{\eta_t}\,\dot{N}_{3B} \;=\; \frac{F_{3B}\,L_{3B}}{\sqrt{27}}\,\frac{\overline{\omega}^6\,m^3}{(2\,\pi)^3}\,(\frac{\eta_t}{U_t})^2\,N^3\,. \tag{6.5}$$

Changes of Potential : Spilling is independent of collisions. While the trap depth is lower, the eigenstate of the trapping potential with highest energies can become unbound. Atoms in these state are lost from the trap. The total number of atoms lost per time unit due to potential changes $\dot{N}_p$ is given by

$$\dot{N}_p \;=\; \frac{{\eta_t}^3\exp(-\eta_t)}{4P(3,\eta_t)}\,\frac{\dot{U}_t}{U_t}\,N \tag{6.6}$$

here $P(3,\eta_t) = \frac{1}{\Gamma(3)}\int_0^{\eta_t} t^2 \exp(-t)dt$ is an incomplete gamma function where $\Gamma(3)$ is a gamma function [Pin98, Bar02].

The total energy of the atoms is modified by the change of the trap shape. For a large value of η_t, the rate of the total energy change due to potential changes $\dot{E}_p$ is given by

$$\dot{E}_p = \frac{3}{2}\frac{\dot{U}_t}{\eta_t} N \tag{6.7}$$

where $E = 3Nk_BT$ is the total energy of the trapped atoms [Pin98, Bar02].

If the condition of adiabatic changes of potential is valid, there are no atom losses. The condition for adiabatic change is $\left|\dot{\overline{\omega}}\right| \ll \overline{\omega}^2$. For the experimental data in Figure (6.4), the ramps fit this condition except for the final ramp step. In the model, the atom losses due to potential changes is considered.

Stray Light : The atoms absorb photons at the rate $\Gamma' = s/(2\,(\,1 + s\,))$ $\approx \frac{1}{2}\,s\,\Gamma$ where s is the off-resonance saturation parameter. Assuming stray light is detuned by $\delta = \Gamma/2$ and the light shift due to the CODT laser beams is negligible, $\Delta = 0$, which is the case when the light shifts less than a MHz as opposed to 36 MHz of $\Gamma/(2\,\pi)$ of 423 nm radiation, s is given by

$$s = \frac{1}{2}\frac{\Omega^2}{\delta^2 + (\Gamma/2)^2 + \Delta^2} \approx \frac{1}{2}\frac{\Omega^2}{\delta^2 + (\Gamma/2)^2} \approx \frac{\Omega^2}{\Gamma^2} = \frac{s_0}{2} \tag{6.8}$$

here Ω is the Rabi frequency. Therefore, $\Gamma' = s_0\,\Gamma/4$, where s_0 is the ratio between the stray light intensity and the saturation intensity, i.e., on-resonance saturation parameter.

Each absorbed photon adds a recoil energy $E_R = k_B\,T_R/2$ to the trapped atoms where T_R is the recoil temperature, see Equation (2.8), and energy increases at the rate

$$\dot{E}_s = \Gamma'\,E_R\,. \tag{6.9}$$

During the period t, the total energy increases by

$$\int_0^t \dot{E}_s\,d\,t = \Gamma'\,E_R\,t\,. \tag{6.10}$$

Thus, t is the time necessary for an atom to leave the trap, if

$$U_t = \Gamma'\,E_R\,t\,. \tag{6.11}$$

Therefore, the rate of atom loss per unit time is

$$\gamma_s = \frac{\Gamma'\,E_R}{U_t}\,. \tag{6.12}$$

As a consequence, the rate of atom loss due to stray light $\dot{N}_{st}$ can be written as

$$\dot{N}_{st} = \gamma_s N . \tag{6.13}$$

The rate of the total energy change due to the stray light $\dot{E}_{st}$ is given by

$$\dot{E}_{st} = E_R \dot{N}_{st} . \tag{6.14}$$

One can see that γ_s gets larger while U_t decreases. Therefore, the loss and heating of atoms due to stray light become more and more important at the end of evaporative cooling. For the trapped atoms in the $^1S_0$ ground state, 423 nm radiation is the only light source in the experiment that has to been taken into account for this case. The Γ at this wavelength is 2.18×10^8 and the saturation intensity is $59.9\,\mathrm{mW/cm^2}$.

6.3.4 Numerical Results

Combining the parameters considered above, the total atom loss per unit of time $\dot{N}$ during evaporation is given by

$$\dot{N} = -\dot{N}_{ev} - \dot{N}_{3B} - \dot{N}_{st} + \dot{N}_p \tag{6.15}$$

and, the total energy change per unit of time $\dot{E}$ during the evaporation process is

$$\dot{E} = -\dot{E}_{ev} + \dot{E}_{3B} + \dot{E}_{st} + \dot{E}_p \tag{6.16}$$

where the minus sign results from the fact that evaporation provides a cooling mechanism.

With a given U_t and using a Mathematica program to numerically solve the analytic differential Equations (6.15) and (6.16), the evaporative cooling process can be investigated. For the evaporative cooling strategy developed in our group, the depths of the ODTs are reduced simultaneously with the same linear ramps. Thus, U_t can be determined by a linear slope between two adjacent data points which is shown in Figure (6.8). The parameters for modeling can be deduced from the experimental conditions.

F_{3B} and s_0 are the fitting parameters in the model. The best parameters are determined by the least sum of square errors of the time evaluated atom number and the numerical calculation of Equation (6.15) where the first data point is excluded. During the first step of evaporation, there are still atoms in the wings of the CODT. As discussed earlier, the system is not immediately in the equilibrium state after the loading process is terminated. The atoms in the wings still load the dimple by elastic collisions. Accordingly, the dynamics of the trapped atoms during the first ramp step cannot be given

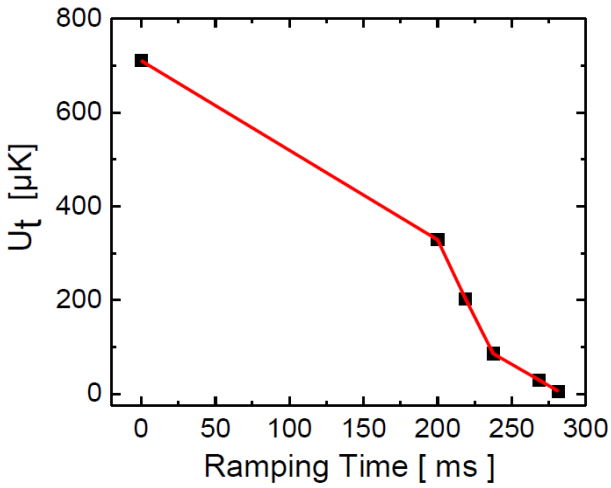

Figure 6.8: The time dependent dimple trap depth U_t. The experimental data is shown by black squares and the linear ramps are presented by red lines.

by the model as more information is needed. i.e., the fit results cannot be scaled.

The fit results are shown in Figures (6.9) and (6.10) where black squares represent the experimental data. Using the numerical solutions of the differential Equations (6.15) and (6.16) and the time dependent geometric mean trap frequency, the time dependent PSD and peak density are evaluated. The resulting F_{3B} is 0.323 and the resulting s_0 is 1.1×10^{-5}.

The black dashed-dotted curve presents the fit results without considering the influence of stray light. The red solid curve shows the fit results when stray light is considered. For both situations, the atom loss is rapid during the beginning of the evaporation process. It is dominated by elastic collisions and three-body collisions due to the high peak density of the atoms. Without considering the factor of stray light, the loss of atoms at the end of the evaporation is due to trap shape changes.

The effects of the stray light become more important while the trap depth is reduced. As shown by the red solid curves in Figures (6.9) and (6.10), firstly, one can observe that the atoms are lost dramatically at the end of the evaporation. From the temperature fit, the temperature of the atoms increases at the end of the evaporation. Therefore, the peak density of the atoms reduces the fastest in a shallow trap. Moreover, the PSD fit for the atoms starts to decrease after a ramping time of 270 ms.

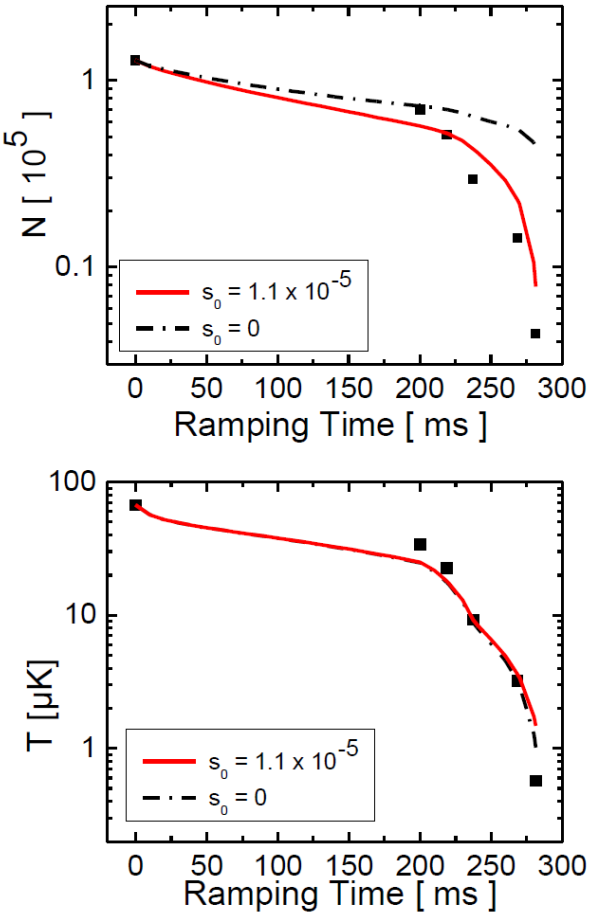

Figure 6.9: The fit results to the number N and the temperature T of the atoms during evaporation. The experimental data is shown by black squares. The black dashed-dotted curve and the red solid curve present the fitting results when loss and heating due to stray light are not, and are, taken into account, respectively. The parameters used in the figure are defined in the same way as in the previous sections. More details are provided in the text.

The resulting value of s_0 indicates that even a very small intensity of stray light (at the level of few hundreds nW/cm^2) causes problems for the evaporation. Consequently, filtering out the stray light in the experimental system is necessary to reach a ^{40}Ca BEC.

As the reader can see, the fitted curves shown in Figures (6.9) and (6.10) have kinks, which result from the changes of U_t during evaporation. i.e., the changes of the ramping slope. One observation of the model is that

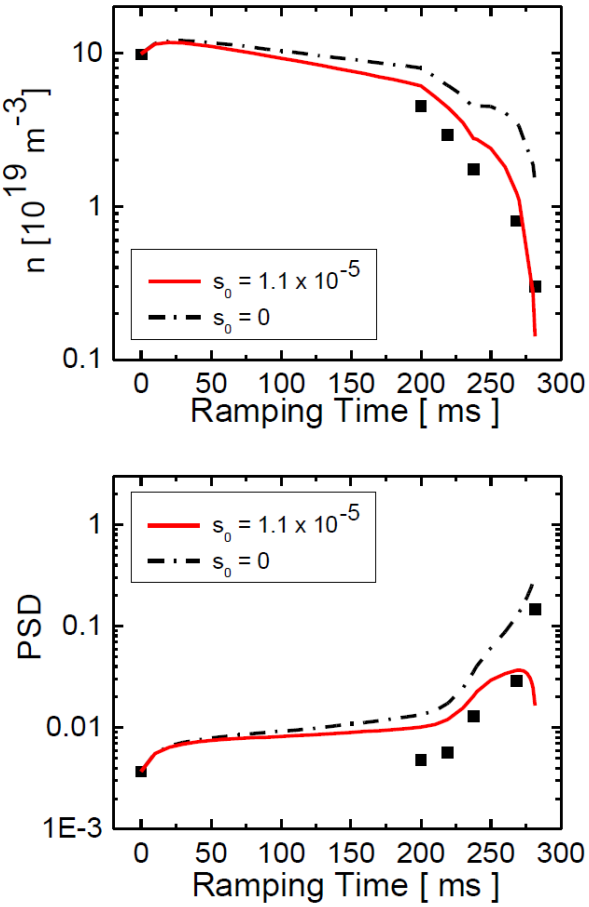

Figure 6.10: The fit results to the peak density n and the PSD of the atoms during evaporation. The experimental data is shown by black squares. The black dashed-dotted curve and the red solid curve present the fitting results when loss and heating due to stray light are not, and are, taken into account, respectively. The parameters used in the figure are defined in the same way as in the previous sections. Further details are provided in the text.

the ramping procedure strongly affects the evaporation process. Therefore, one may use the model and a designed ramping procedure to optimize the experimental parameters and to estimate necessary improvements to reach a BEC. Unfortunately, this could not be done in the frame work of this thesis due to time limitations.

Although the model developed is simple, it offers a straightforward method to study the evaporative dynamics of the atoms. Notice, the fit results

could only show that the density dependent losses and heating are important for the evaporative dynamics of the atoms. As information on the atoms in the wings is lacking, it is a challenge to determinate the value of F_{3B}. Similarly, the value of Γ_{ev} cannot be determined by the model. Besides information on the atoms in the wings, more details of complex collisions between the atoms in the hydrodynamic region have to be considered in the model to determine the value of Γ_{ev}.

6.3.5 Conclusion

The developed model suggests that the observed fast particle loss during evaporation is independent of the density, which excludes collisions as its cause. A strong dependence on the trap depth is found which suggests that residual stray light heating might be the underlying mechanism. In the experiment, there are many mechanical shutters inserted in the beam path of 423 nm radiation at various positions. Blue light reflected from these shutters would affect the trapped atoms even though the intensity is attenuated by the viewports of the vacuum chamber. Therefore, rearranging the mechanical shutters for blue radiation is necessary in order to eliminate any stray light entering the vacuum chamber.

Recently our group has successfully increased the PSD of the trapped atoms by a factor of four (≈ 0.4), using the strategy of the PTB. We have demonstrated that stray light is not the main limitation on evaporation. Instead, the instability of the HODT beam described in Section (6.3.2) causes fast atom loss at the end of evaporation [Hal11]. For modeling, the instability of the HODT was not taken into account as one of the reasons limiting the evaporation, which has been discussed. By adding trap depth dependent atom loss caused by the power dependent beam size changes of the HODT in the model, one may estimate that a transition to a quantum degenerate gas state would occur using the current experimental parameters or if further improvements are required.

Chapter 7

Perspectives

7.1 Continuous Loading Studies of $^3P_0$ Metastable State Atoms

Loading $^3P_0$ samples into ODTs is an interesting topic because of their particular significance for clock applications and because of the prospects for evaporative cooling. This energy level appears to be the most favorable within the triplet system. Since $^3P_0$ is non-magnetic and the lowest energy state of the triplet ground state manifold, the number of possible inelastic collision channels is limited and far lower loss rates may be expected in comparison to $^3P_2$ samples. Accordingly, high atomic densities could be studied. Implementing a continuous loading scheme promises a large population in the $^3P_0$ ODT with densities appropriate for study of collision processes.

The basic loading mechanism is sketched in Figure (7.1(a)). In order to populate the $^3P_0$ state we start with $^3P_2$ samples prepared by a $^3P_2$ triplet-MOT and optically pump these atoms with a pump beam at 431.8 nm via the $^3P_1$ [4p4p] state to the $^3P_0$ state. The optical pump laser beam will be shaped to match the dipole trap potential, such that only $^3P_2$ atoms located within the trap volume are pumped to the $^3P_0$ state and thus can be trapped with high efficiency. The $^3P_2$ light shift potential will be continuously refilled from the reservoir of cold atoms provided by the $^3P_2$ triplet-MOT and thus transfer a continuous stream of cold atoms into the $^3P_0$ ODT until the $^3P_2$ population of the $^3P_2$ triplet-MOT atoms is exhausted. The branching ratio for the decay of $^3P_1$ [4p4p] atoms is such that about 56 % of the atoms are transferred to the desired $^3P_0$ state and while 44 % of the atoms are expected to decay to the $^3P_1$ state and further to the singlet ground state. Other decay channels make a total contribution on the per million scale and may be neglected. This quasi-continuous loading procedure may be extended to

a fully continuous scheme by permanently refilling the $^3P_2$ triplet-MOT by the $^1S_0$ singlet-MOT. This is possible because the 423 nm photons of the $^1S_0$ singlet-MOT do not affect the $^3P_0$ atoms.

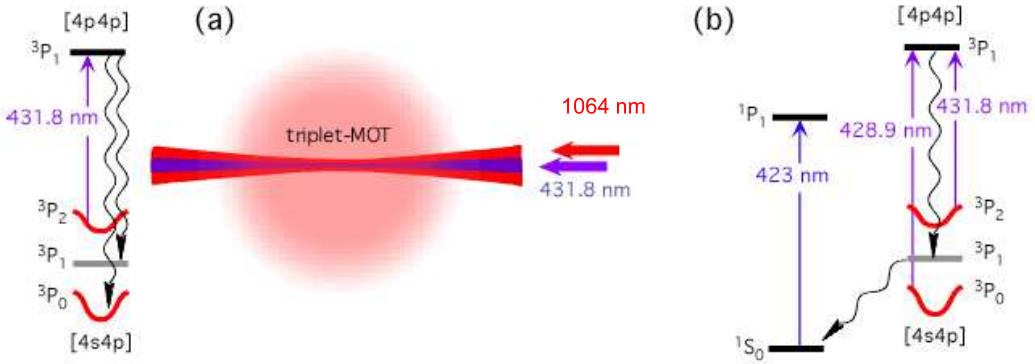

Figure 7.1: (a) Scheme for continuous loading of the $^3P_0$ ODT at 1064 nm. The $^3P_2$ triplet-MOT is continuously reloaded by the $^1S_0$ singlet-MOT, which operates with 423 nm light and thus does not affect the $^3P_0$ atoms. (b) Scheme for detection of $^3P_0$ atoms.

The work can be performed with a CODT, following the work on Yb atoms in the singlet ground state to further increase the density of the trapped $^3P_0$ atoms [Tak03]. Depending on the results with respect to the ratio between the elastic and inelastic scattering rates, we plan to implement evaporative cooling steps to extend our collision rate measurements to lower temperatures. As a further extension, depending upon our findings regarding the collisional properties, we will investigate the possibility to reach quantum degeneracy in the $^3P_0$ state [And95, Dav95].

The detection scheme for $^3P_0$ atoms is shown in Figure (7.1(b)). It is achieved by optical pumping via the $^3P_1$ [4p4p] state to $^3P_1$ [4s4p] using violet radiation. With a single pumping beam at 428.9 nm a transfer efficiency of 38.6 % is expected while with a second beam at 431.8 nm, which is also used for the loading of $^3P_0$ atoms (see Figure (7.1(a))), nearly 100 % transfer efficiently is obtained. The $^3P_1$ atoms spontaneously decay to the singlet ground state and are detected by an absorption image via the strong principle fluorescence line at 423 nm. This procedure has the significant advantage of using a nearly closed cycling transition for the imaging. The relatively long lifetime of the $^3P_1$ state gives rise to some small undesired expansion of the samples, which has to be taken into account for in the interpretation of the

obtained images [Han06b].

List of Abbreviations

AEA	Alkaline-Earth Atom
AMA	Alkaline-Metal Atom
AOM	Acousto-Optic Modulator
A.P.	Anamorphic Prism Pair
AR	Anti-Reflection
BEC	Bose-Einstein Condensate
CCD	Charge-Couple Device
CODT	Crossed Optical Dipole Trap
EOM	Electro-Optic Modulator
HODT	Optical Dipole Trap in a Horizontal Plane
HWP	Half Wave-Plate
MOT	Magneto-Optical Trap
OD	Optical Density
ODT	Optical Dipole Trap
PA	Photoassociation
PBC	Polarizing Beam-Splitter Cube
PD	Photo-Diode
PDH	Pound-Drever-Hall
PSD	Phase Space Density
QWP	Quarter Wave-Plate
RF	Radio Frequency
SNR	Signal-to-Noise Ratio
Tm:YAG	Thulium Doped Yttrium Aluminium Garnet
TOF	Time-of-Flight
UV	Ultraviolet
VCO	Voltage Controlled Oscillator
VODT	Optical Dipole Trap in a Vertical Plane

List of Symbols

a	Scattering Length
a_0	Bohr Radius
A	Pixel Area
B	Magnetic Field
c	Light Speed
$\dot{E_{3B}}$	Rate of Total Energy Change due to Three-Body Collisions
$\dot{E_{ev}}$	Rate of Total Energy Change due to Evaporative Cooling
$\overline{E_{ev}}$	Average Energy Loss per Evaporated Atom
$\dot{E}_p$	Rate of Total Energy Change due to Potential Changes
E_R	Recoil Energy
$\dot{E_{st}}$	Rate of Total Energy Change due to Stray Light
f	Focal Length
F_{scat}	Scattering Force
g	Gravitational Acceleration
h	Planck Constant
$\hbar$	$h/(2\pi)$
I	Intensity
I_s	Saturation Intensity
k	Wavenumber
k_{th}	Thermal Wavevector
k_B	Boltzmann Constant
L_{3B}	Three-Body Loss Coefficient
m	Mass of an Atom
n	Peak Density of an Atomic Sample
n_{CCD}	Number of CCD Image sensor Noise Electrons
n_{photon}	Number of Shot Noise Electrons
$n_{read-out}$	Number of Read-Out Noise Electrons

n_{signal}	Signal Electron Number
N	Atom Number
$\overline{N}$	Steady State Atom Number
$\dot{N_{3B}}$	Total Atom Loss per Time Unit due to Three-Body Collisions
$\dot{N_{ev}}$	Total Atom Loss per Time Unit due to Evaporative Cooling
$\dot{N_{st}}$	Total Atom Loss per Time Unit due to Stray Light
P	Power of a Laser Beam
$P_{1,\xi}(P)$	Probability for an Atom in the $^3P_2$ Triplet-MOT to Enter V_{ODT} without Being Optically Pumped
$P_{2,\xi}(P)$	Probability for an Atom in the $^3P_2$ Triplet-MOT Having Entered V_{ODT} to Leave It without Being Optically Pumped
$P_{in}(P)$	Average of $P_{1,\xi}(P)$ over Trajectories and Velocities According to a Temperature of the $^3P_2$ Triplet-MOT
$P_{out}(P)$	Average of $P_{2,\xi}(P)$ over Trajectories and Velocities According to a Temperature of the $^3P_2$ Triplet-MOT
P_L	Probability of an Atom in the Wings to Load into the Dimple via Elastic Collisions
r_d	Effective Beam Radius of the Dimple
r_h	Beam Radius of the HODT
r_w	Beam Waist of the Wing of the CODT
r_v	Beam Radius of the VODT
R_c	Capture Range of a MOT
$R(P)$	Effective Capture Rate of an ODT for Singlet Atoms, Depending on a Given Pump Laser Power
s	Saturation Parameter
s_0	On-Resonance Saturation Parameter
σ_{sc}	On-Resonance Scattering Cross-Section
σ_t	Energy-Dependent Elastic Scattering Cross-Section
σ_0	Elastic Scattering Cross-Section Independent of Energy
t_{coll}	Collision Time of Atoms in an ODT
t_{osc}	Oscillation Time of Atoms in an ODT
T_{ax}	Axial Temperature
T_{rad}	Radial Temperature
T_D	Doppler Temperature
T_R	Recoil Temperature
$\overline{u}$	Mean Relative Velocity

U	Well Depth
U_t	Time Dependent Well Depth
V_{eff}	Effective Trap Volume
V_{rec}	Recoil Velocity of a Single Photon
v_{rms}	Random Velocity of an Atom
V_{ODT}	Volume of an ODT
z_R	Rayleigh Range of a Beam
α_{EV}	Evaporative Quantity
β	Gradient of a Magnetic Field
δ	Detuning
$\widetilde{\delta}$	Power Broadening Detuning
Δl_{min}	Differential-Limited Resolution
η	Truncation Parameter
η_{ef}	Quantum Efficiency of a CCD Sensor
η_t	Time Dependent Truncation Parameter
$\overline{\omega}$	Mean Geometric Trap Frequency
ω_0	Beam Waist of a Laser Beam
ω_{ax}	Axial Trap Frequency
ω_{ot}	Frequency of an Optical Transition
ω_{rad}	Radial Trap Frequency
ω_l	Frequency of Laser Radiation
$\omega(z)$	$1/e^2$ Radius of a Beam, Depending on Position z
Ω	Rabi Frequency
γ	Loss Rate of a $^1S_0$ ODT Atom, Independent of Pump Laser Power
$\gamma_B(P)$	Additional Loss Rate of a $^1S_0$ ODT Atom, Depending on a Given Pump Laser Power
$\gamma_{ev}(T)$	Two-Body Elastic Collision Loss Rate, Depending on a Temperature of Atoms in a $^1S_0$ ODT
γ_{EV}	Evaporative Quantity
γ_{rms}	Random Position Shift of an Atom
γ_{rel}	Cross-Dimensional Relaxation Rate
Γ	Linewidth
$\widetilde{\Gamma}$	Power Broadening Linewidth
$\Gamma(P, \xi(t))$	Optical Pumping Rate along $\xi(t)$ of an Atom in the $^3P_2$ Triplet-MOT
Γ_{BG}	Background Collision Rate

Γ_{3B}	Three-Body Collision Rate
Γ_{el}	Elastic Collision Rate
Γ_{ev}	Evaporation Rate
Γ_{sc}	Photon Scattering Rate of an ODT Beam
ν_{rms}	Random Velocity of Atoms
$\nu(T)$	Temperature Dependent Correction Factor of an Effective Trap Volume
λ	Wavelength
λ_{th}	de Broglie Wavelength
ρ_{ee}	Population in an Excited State
τ_{3B}	1/e Three-Body Half Time
τ_{BG}	1/e Lifetime
$\xi(t)$	Ballistic Trajectory of Atoms in the $^3P_2$ Triplet-MOT

List of Figures

List of Tables

Bibliography

[AD] *Atomic Database*. http://www.cfa.harvard.edu/amp/tools.html .

[And95] M. H. Anderson, J. R. Ensher, M. R. Matthews, C. E. Wieman and E. A. Cornell. *Observation of Bose-Einstein Condensation in a Dilute Atomic Vapor*. Science **269** (1995).

[Arn97] M. Arndt, M. B. Dahan, D. Gury-Odelin, M. W. Reynolds and J. Dalibard. *Observation of a Zero-Energy Resonance in Cs-Cs Collisions*. Phys. Rev. Lett. **79**, 625 (1997).

[Bar02] M. D. Barrett. *A QUEST for BEC: An All Optical Alternative* (Ph.D. Thesis, Georgia Institute of Technology, 2002).

[Bla01] E. D. Black. *An Introduction to Pound-Drever-Hall Laser Frequency Stabilization*. Am. J. Phys. **69**, 79 (2001).

[Boh97] J. L. Bohn and P. S. Julienne. *Prospects for Influencing Scattering Lengths with Far-Off-Resonant Light*. Phys. Rev. A. **56**, 1486 (1997).

[Boh99] J. L. Bohn and P. S. Julienne. *Semianalytic Theory of Laser-Assisted Resonant Cold Collisions*. Phys. Rev. A. **60**, 414 (1999).

[Ciu04] R. Ciurylo, E. Tiesinga, S. Kotochigova and P. S. Julienne. *Photoassociation Spectroscopy of Cold Alkaline-Earth-Metal Atoms Near the Intercombination Line*. Phys. Rev. A. **70**, 062710 (2004).

[Ciu05] R. Ciurylo, E. Tiesinga and P. S. Julienne. *Optical Tuning of the Scattering Length of Cold Alkaline-Earth-Metal Atoms*. Phys. Rev. A. **71**, 030701 (2005).

[Com06] D. Comparat, A. Fioretti, G. Stern, E. Dimova, B. L. Tolra and P. Pillet. *Optimized Production of Large Bose-Einstein Condensates*. Phys. Rev. A. **73**, 043410 (2006).

[Dal98] J. Dalibard. *Collisional Dynamics of Ultra-Cold Atomic Gases* (Proceedings of the International School of Physics Enrico Fermi, Course CXL: Bose-Einstein Condensation in Gases, M. Inguscio, S. Stringari, C. Wieman edts. Varenna, 1998).

[Dav95] K. B. Davis, M. O. Mewes, M. R. Andrews, N. J. van Druten, D. S. Durfee, D. M. Kurn and W. Ketterle. *Bose-Einstein Condensation in a Gas of Sodium Atoms*. Phys. Rev. Lett. **75**, 3969 (1995).

[Doy04] J. Doyle, B. Friedrich, R. V. Krems and F. Masnou-Seeuws. *Editorial: Quo Vadis, Cold Molecules?*. Eur. Phys. J. D. **31**, 149 (2004).

[Dre83] R. W. P. Drever, J. L. Hall, F. V. Kowalski, J. Hough, G. M. Ford, A. J. Munley and H. Ward. *Laser Phase and Frequency Stabilization Using an Optical Resonator*. Appl. Phys. B. **31**, 97 (1983).

[Eco09] Y. N. M. de Ecobar, P. G. Mickelson, M. Yan, B. J. DeSalvo, S. B. Nagel and T. C. Killian. *Bose-Einstein Condensation of* ^{84}Sr. Phys. Rev. Lett. **103**, 200402 (2009).

[Eno08a] K. Enomoto, K. Kasa, M. Kitagawa and Y. Takahashi. *Optical Feshbach Resonance Using the Intercombination Transition*. Phys. Rev. Lett. **101**, 203201 (2008).

[Eno08b] K. Enomoto, M. Kitagawa, S. Tojo and Y. Takahashi. *Hyperfine-Structure-Induced Purely Long-Range Molecules*. Phys. Rev. Lett. **100**, 123001 (2008).

[Geh98] M. E. Gehm, K. M. O´Hara, T. A. Savard and J. E. Thomas. *Dynamics of Noise-Induced Heating in Atom Traps*. Phys. Rev. A. **58**, 3914 (1998).

[Gri00] R. Grimm, M. Weidemueller and Y. B. Ovchinnikov. *Optical Dipole Traps for Neutral Atoms*. Adv. At. Mol. Opt. Phys. **42**, 95 (2000).

[Gru01] J. Gruenert and A. Hemmerich. *Optimizing the Production of Metastable Calcium Atoms in a Magneto-Optical Trap*. Appl. Phys. B. **73**, 815 (2001).

[Gru02a] J. Gruenert. *Ultracold Metastable Calcium Atoms in a Bichromatic Magneto-Optical Trap* (Ph.D. Thesis, Universität Hamburg, 2002).

[Gru02b] J. Gruenert and A. Hemmerich. *Sub-Doppler Magneto-Optical Trap for Calcium*. Phys. Rev. A. **65**, 041401 (2002).

[Hal89] J. L. Hall, M. Zhu and P. Buch. *Prospects for Using Laser-Prepared Atomic Fountains for Optical Frequency Standards Applications*. J. Opt. Soc. Am. B. **6**, 2194 (1989).

[Hal11] P. Halder. *Private Communication* (January, 2011).

[Han05] D. Hansen and A. Hemmerich. *Doppler-Free Spectroscopy of Metastable Calcium in a Discharge Heat Pipe*. Phys. Rev. A. **72**, 022502 (2005).

[Han06a] D. Hansen. *Collisional Properties of Metastable Calcium Atoms in a Miniaturized Ioffe Trap* (Ph.D. Thesis, Universität Hamburg, 2006).

[Han06b] D. Hansen and A. Hemmerich. *Observation of Multichannel Collisions of Cold Metastable Calcium Atoms*. Phys. Rev. Lett. **96**, 073003 (2006).

[Hec98] E. Hecht. *Optics* (Addison Wesley Longman, Inc., 1998).

[Hop00] S. A. Hopkins, S. Webster, J. Arlt, P. Bance, S. Cornish, O. Maragò and C. J. Foot. *Measurement of Elastic Cross Section for Cold Cesium Collisions*. Phys. Rev. A. **61**, 032707 (2000).

[Kav00] G. M. Kavoulakis, C. J. Pethick and H. Smith. *Collisional Relaxation in Diffuse Clouds of Trapped Bosons*. Phys. Rev. A. **61**, 053603 (2000).

[Ket96] W. Ketterle and N. J. V. Druten. *Evaporative Cooling of Trapped Atoms*. Adv. At. Mol. Opt. Phys. **37**, 181 (1996).

[Ket99] W. Ketterle, D. S. Durfee and D. M. Stamper-Kurn. *Making, Probing and Understanding Bose-Einstein Condensates* (In Bose-Einstein Condensation in Atomic Gases, Proceedings of the International School of Physics ‘ Enrico Fermi ’, Course CXL, edited by M. Inguscio, S. Stringari and C. E. Wieman. (IOS Press, Amsterdam), 1999).

[Kok03] V. Kokoouline, R. Santra and C. H. Green. *Multichannel Cold Collisions between Metastable Sr Atoms*. Phys. Rev. Lett. **90**, 253201 (2003).

[Kra09] S. Kraft, F. Vogt, O. Appel, F. Riehle and U. Sterr. *Bose-Einstein Condensation of Alkaline Earth Atoms:* ^{40}Ca. Phys. Rev. Lett. **103**, 130401 (2009).

[Lui96] O. J. Luiten, M. W. Reynolds and J. T. M. Walraven. *Kinetic Theory of the Evaporative Cooling of a Trapped Gas*. Phys. Rev. A. **53**, 381 (1996).

[Mac01] R. Machholm, P. S. Julienne and K. A. Suominen. *Calculations of Collisions between Cold Alkaline-Earth-Metal Atoms in a Weak Laser Field*. Phys. Rev. A. **64**, 033425 (2001).

[Mon93] C. R. Monroe, E. A. Cornell, C. A. Sackett, C. J. Myatt and C. E. Wieman. *Measurement of Cs-Cs Elastic Scattering at* $T = 30\ \mu K$. Phys. Rev. Lett. **70**, 414 (1993).

[O01] K. M. O´Hara, M. E. Gehm, S. R. Granade and J. E. Thomas. *Scaling Laws for Evaporative Cooling in Time-Dependent Optical Traps*. Phys. Rev. A. **64**, 051403 (2001).

[PCO] http://www.pco.de .

[Pin98] P. H. W. Pinkse, A. Mosk, M. Weidemüller, M. Reynolds, T. W. Hijmans and J. T. M. Walraven. *One-Dimensional Evaporative Cooling of Magnetically Trapped Atomic Hydrogen*. Phys. Rev. A. **57**, 4747 (1998).

[Raa87] E. L. Raab, M. Prentiss, A. Cable, S. Chu and D. E. Pritchard. *Trapping of Neutral Sodium Atoms with Radiation Pressure*. Phys. Rev. Lett. **59**, 2631 (1987).

[Sav97] T. A. Savard, K. M. O´Hara and J. E. Thomas. *Laser-Noise-Induced Heating in Far-Off Resonance Optical Traps*. Phys. Rev. A. **56**, R1095 (1997).

[Sch03] P. O. Schmidt, S. Hensler, J. Werner, A. Griesmaier, A. Görlitz, T. Pfau and A. Simoni. *Determination of the S-Wave Scattering Length of Chromium*. Phys. Rev. Lett. **91**, 193201 (2003).

[Ses91] D. W. Sesko, T. G. Walker and C. E. Wieman. *Behavior of Neutral Atoms in a Spontaneous Force Trap*. J. Opt. Soc. Am. B. **8**, 946 (1991).

[Spo05] P. Spoden, M. Zinner, N. Herschbach, W. J. van Drunen, W. Ertmer and G. Birkl. *Collisional Properties of Cold Spin-Polarized Metastable Neon Atoms*. Phys. Rev. Lett. **94**, 223201 (2005).

[Ste86] S. Stenholm. *The Semiclassical Theory of Laser Cooling*. Rev. Mod. Phys. **58**, 699 (1986).

[Ste04] U. Sterr, C. Degenhardt, H. Stoehr, C. Lisdat, H. Schnatz, J. Helmcke, F. Riehle, G. Wilpers, C. Oates and L. Hollberg. *The Optical Calcium Frequency Standards of PTB and NIST*. C. R. Physique **5**, 845 (2004).

[Ste09] S. Stellmer, M. K. Tey, B. Huang, R. Grimm and F. Schreck. *Bose-Einstein Condensation of Strontium*. Phys. Rev. Lett. **103**, 200401 (2009).

[Stu05] J. Stuhler, A. Griesmaier, T. Koch, M. Fattori, T. Pfau, S. Giovanazzi, P. Pedri and L. Santos. *Observation of Dipole-Dipole Interaction in a Degenerate Quantum Gas*. Phys. Rev. Lett. **95**, 150406 (2005).

[Tak03] Y. Takasu, K. Maki, K. Komori, T. Takano, K. Honda, M. Kumakura, T. Yabuzaki and Y. Takahashi. *Spin-Singlet Bose-Einstein Condensation of Two-Electron Atoms*. Phys. Rev. Lett. **91**, 040404 (2003).

[Tak09] Y. Takasu and Y. Takahashi. *Quantum Degenerate Gases of Ytterbium Atoms*. JPSJ **78**, 012001 (2009).

[Toj06] S. Tojo, M. Kitagawa, K. Enomoto, Y. Kato, Y. Takasu, M. Kumakura and Y. Takahashi. *High-Resolution Photoassociation Spectroscopy of Ultracold Ytterbium Atoms by Using the Intercombination Transition*. Phys. Rev. Lett. **96**, 153201 (2006).

[Tra09] A. Traverso, R. Chakraborty, Y. N. M. de Escobar, P. G. Mickelson, S. B. Nagel, M. Yan and T. C. Killian. *Inelastic and Elastic Collision Rates for Triplet States of Ultracold Strontium*. Phys. Rev. A. **79**, 060702 (2009).

[Wal90] T. Walker, D. Sesko and C. Wieman. *Collective Behavior of Optically Trapped Neutral Atoms*. Phys. Rev. Lett. **64**, 408 (1990).

[Wal96] J. M. T. Walraven. *Atomic Hydrogen in Magnetostatic Traps, in Quantum Dynamics of Simple System* (44^{th} Scottisch Universities

Summer School in Physics, SUSSP Publications, Edinburgh, and Institute of Physics Publishing, London, 1996).

[Web03a] T. Weber. *Bose-Einstein Condensation of Optically Trapped Cesium* (Ph.D. Thesis, Universität Innsbruck, 2003).

[Web03b] T. Weber, J. Herbig, M. Mark, H. C. Nägerl and R. Grimm. *Bose-Einstein Condensation of Cesium*. Science **299**, 232 (2003).

[Wie76] C. Wieman and T. W. Hänsch. *Doppler-Free Laser Polarization Spectroscopy*. Phys. Rev. Lett. **36**, 1170 (1976).

[Yam07] A. Yamaguchi. *Metastable State of Ultracold and Quantum Degenerate Ytterbium Atoms: High-Resolution Spectroscopy and Cold Collisions* (Ph.D. Thesis, Kyoto University, 2007).

[Yam08] A. Yamaguchi, S. Uetake, D. Hashimoto, J. M. Doyle and Y. Takahashi. *Inelastic Collisions in Optically Trapped Ultracold Metastable Ytterbium*. Phys. Rev. Lett. **101**, 233002 (2008).

[Yan07] C. Y. Yang, P. Halder, O. Appel, D. Hansen and A. Hemmerich. *Continuous Loading of* $^1S_0$ *Calcium Atoms into an Optical Dipole Trap*. Phys. Rev. A. **76**, 033418 (2007).

[Yan09] M. Yan, R. Chakraborty, P. G. Mickelson, Y. N. M. de Escobar and T. C. Killian. *Numerical Modeling of Collisional Dynamics of Sr in an Optical Dipole Trap*. arXiv:0905.2223v1 (2009).

[Zel06] T. Zelevinsky, M. M. Boyd, A. D. Ludlow, T. Ido, J. Ye, R. Ciurylo, P. Naidon and P. S. Julienne. *Narrow Line Photoassociation in an Optical Lattice*. Phys. Rev. Lett. **96**, 203201 (2006).

[Zim95] C. Zimmermann, V. Vuletic, A. Hemmerich, L. Ricci and T. W. Hänsch. *Design for a Compact Tunable Ti:Sapphire Laser*. Optics Letters **20**, 297 (1995).

Acknowledgments

First of all, I would like to thank the DAAD (Deutscher Akademischer Austausch-Dienst) offering me the chance to study and prepare my Ph.D. thesis in Germany as well as providing me support for my studies. I like to thank Prof. Dr. Andreas Hemmerich for the interesting research subject and offering me the possibility to prepare my Ph.D. thesis in his workgroup. I like to thank Prof. Dr. Henning Moritz and Prof. Dr. Klaus Sengstock for taking over the evaluation of my Ph.D. thesis and the oral defence of my thesis.

During the past few years, I received much support and assistance from different people to complete my work. For this help, I want to say a big *Thank You* to all of them. I want to thank Mr. Dieter Barlosius for providing us homemade discharge cells, and especially for the quick support when the cells were out of order. Due to his great support, the experiments could run smoothly. Moreover, many thanks to Dr. Dirk Hansen for his assistance at the calcium experiment. He gave me a helpful guide and hints for operating the system and made me familiar with the experiment. Another thank you goes to my team mates, Purbasha Halder and Oliver Appel, for their works on the experiment. I also want to thank Dr. Parvis Soltan-Panahi for several scientific discussions and supporting me with different technical equipment for additional measurements. Finally, I want to thank Ms. Silke Froemming for assisting me with many practical issues in Germany.

For my study in Germany, I have faced many difficulties. I greatly thank for the help from the following people who help me overcome these challenges: Arne Wickenbrock for helping me to get used to the life and the study in Germany, especially for the first few months of my life in Germany. Dr. Parvis Soltan-Panahi and Dr. Malik Lindholdt for their useful remarks. Special thanks go to Parvis for his help and guide to let me get more familiar with the German way of life.

Next, I wish all the best to all group members in the workgroup of Prof. Dr. Andreas Hemmerich.

Last but not least I would like to thank my family and my friends for

their great assistance and for supporting me during the last years. I would especially thank my husband for his great support in the last years of my Ph.D. study.